TAMPEREEN TEKNILLINEN YLIOPISTO
TAMPERE UNIVERSITY OF TECHNOLOGY
Julkaisu 727 • Publication 727

Lauri Rostila

Electromagnetic Design of Superconducting Coated Conductor Power Cables

Tampere 2008

Tampereen teknillinen yliopisto. Julkaisu 727
Tampere University of Technology. Publication 727

Lauri Rostila

Electromagnetic Design of Superconducting Coated Conductor Power Cables

Thesis for the degree of Doctor of Technology to be presented with due permission for public examination and criticism in Rakennustalo Building, Auditorium RG202, at Tampere University of Technology, on the 9th of May 2008, at 12 noon.

Tampereen teknillinen yliopisto - Tampere University of Technology
Tampere 2008

ISBN 978-952-15-1944-4 (printed)
ISBN 978-952-15-2036-5 (PDF)
ISSN 1459-2045

Abstract

Superconducting YBCO cables are the latest step in the development of their kind, and their viability is constantly improving, because YBCO tapes are going down in price. The Super3C project aims to design, manufacture, and test a superconducting 30-m, 1-kA, 10-kV YBCO cable prototype, which will provide important information about the YBCO cable performance. A successful design of this cable must combine cryogenic, mechanical, and electromagnetic aspects. This thesis focuses on the electromagnetic part, which aims at low AC losses, a high critical current with a small amount of superconducting tape, and good tolerance of fault currents. With this in mind, computational tools were developed to predict the above cable capabilities. The special characteristics sought for in modeling the superconductor were highly nonlinear resistivity and strong magnetic-flux-density-dependent critical current density. Another aspect to be addressed in modeling is the troublesome high aspect ratio of the YBCO.

In this work, a circuit-analysis-based model was developed to predict AC losses in YBCO cables. Predicted losses were close to those measured for a one-layer, 0.5-m YBCO cable. Furthermore, some tape-wise variation was measured in the current, but computations suggested that the problem can be avoided with the 30-m cable. In addition, an algorithm was developed to compute the cable's critical current to further improve the AC loss model. Results suggest that tape arrangements can greatly affect the cable's critical current, and in cable use, the tape's critical current can be higher than in the self-field. The critical current algorithm was exploited to solve intrinsic material parameters from ordinary voltage-current measurements. The impact of fault current was analyzed by solving the heat conduction equation together with Maxwell's equations.

Preface

This work concludes my four-year study of superconducting, coated conductor cables. It has been an exiting time to view the progress in cables and conductors in the past few years and, in addition, to have an opportunity to take part in an international EU project to manufacture a coated conductor cable.

All this time, the Institute of Electromagnetics at Tampere University of Technology provided me with excellent working facilities, for which I am grateful to the former and present heads of our institute, Prof. Lauri Kettunen and Lasse Söderlund; they shouldered many administrative tasks and gave me free hands to concentrate fully on my work. Together with our superconductor group leader Risto Mikkonen, Lasse also helped me in many ways to complete this thesis. In addition, special thanks go to Maija-Liisa Paasonen for arranging so many issues, Heidi Koskela for drawing several figures for the thesis, and Dr. Timo Lepistö for the numerous improvements on the language. Thanks are also due to Dr. Aki Korpela for arranging regular football training for our staff.

In addition, I would like to thank the former and present members of the superconductor group. In 2001, when I was privileged to join the group, I had an opportunity to get to know Dr. Jorma Lehtonen. Later, he became my supervisor, and I am now very grateful to him for his significant assistance in my work. I am also grateful to my former colleague, Dr. Mika Masti, for teaching me the secrets of the technical computing language and for being the fair leader of the EU project. Mika is also one of those who for many years contributed to the relaxed, convivial atmosphere at the institute.

I am also thankful to my colleague, Dr. Saku Suuriniemi, and the other members of our institute for helping me out with numerical modeling and other tasks. I also like to thank the superconductor scientists at Slovak Academy of Sciences, where I had a change to work at the Institute of Electrical Engineering. In addition, many thanks to Tomáš Holúbek and his friends for their hospitality during my stays.

I am also grateful to all my friends and my girlfriend, Jenny, for being there and for helping me escape my academic cubicle at times. In addition,

many thanks to my grandparents for their great support during my studies, and, finally, thanks to my parents, Seija and Ilmari, who have been by my side every step of the way.

Lauri Rostila, 11.12.2007 in Tampere

List of publications

Publication I
L. Rostila, J. Lehtonen, M. Masti, and R. Mikkonen
"Circuit analysis model for AC losses of superconducting YBCO cable"
Cryogenics **46** (2006) 245–251

Publication II
L. Rostila, J. Lehtonen, M. Masti, and R. Mikkonen,
F. Gömöry, T. Melšek, E. Seiler, J. Šouc and A. Usoskin
"AC Losses and Current Sharing in an YBCO Cable"
IEEE Transactions on Applied Superconductivity **17** (2007) 1688–1691

Publication III
L. Rostila, J. Lehtonen, and R. Mikkonen
"Self-field reduces critical current density in thick YBCO layers"
Physica C **451** (2007) 66–70

Publication IV
L. Rostila, J. Lehtonen, M. Masti, and R. Mikkonen
"How to determine critical current density in YBCO tapes
from voltage-current measurements at low magnetic fields"
Superconductor Science and Technology **20** (2007) 1097–1100

Publication V
L. Rostila, L. Söderlund, R. Mikkonen, and J. Lehtonen
"Modelling method for critical current of YBCO tapes in cable use"
Physica C **467** (2007) 91–95

Publication VI
L. Rostila, J. Lehtonen, M. Masti, and R. Mikkonen
"Fault current analysis for a superconducting 1 kA YBCO cable"
Journal of Physics: Conference Series **43** (2006) 865–868

Publication VII
L. Rostila, J. Lehtonen, M. Masti, and R. Mikkonen
"Fault current model for YBCO cables"
Superconductor Science and Technology **19** (2006) 756–761

Publication VIII
L. Rostila, J. Lehtonen, M. Masti, N. Lallouet, J-M. Saugrain,
A. Allais, K. Schippl, F. Schmidt, G. Balog, G. Marot, A. Ravex,
A. Usoskin, F. Gömöry, B. Klinčok, J. Šouc, and H. C. Freyhardt
"Design of a 30 m long 1 kA 10 kV YBCO cable"
Superconductor Science and Technology **19** (2006) 418–422

Contents

Index of symbols

A_1	Magnetic vector potential caused by unit current in tape 1
B	Magnetic field tensor
B_0	Reference magnetic flux density
B_i	Approximated peak value of magnetic flux density of ith layer
B_{ext}	External magnetic flux density
B_{p}	Penetration magnetic flux density
$B_{\parallel}$	Tape's parallel magnetic flux density component
$B_{\perp}$	Tape's perpendicular magnetic flux density component
$\overline{B}_{\mathrm{a,amb},i,s}$	Axial magnetic flux density phasor of ith layer created by sth layer current
$\overline{B}_{\mathrm{a}}$	Axial magnetic flux density phasor
$\overline{B}_{\mathrm{a,self},i}$	Axial magnetic flux density phasor of ith layer created by the ith layer current
$\overline{B}_{\mathrm{c,amb},i,s}$	Circumferential magnetic flux density phasor of ith layer created by sth layer current
$\overline{B}_{\mathrm{c}}$	Circumferential magnetic flux density phasor
$\overline{B}_{\mathrm{c,self},i}$	Circumferential magnetic flux density phasor of ith layer created by ith layer current
$\mathbf{B}_{\mathrm{ext}}$	External magnetic field
$\mathbf{B}_{\mathrm{self}}$	Self-field
$\mathbf{B}_i$	Magnetic field of ith element
$\mathbf{B}_{ij}$	Magnetic field of ith element created by unit current of jth element and its image elements
b_0	Reference magnetic flux density used in fault current analysis
$\mathbf{b}$	Vector of current source terms
C_{p}	Volumetric specific heat
c_{ac}	Resistance ratio
D	Linear part of circuit matrix
d	Thickness of YBCO layer
E	Electric field intensity
E_{c}	Critical electric field

$\mathbf{E}$	Electric field
e_i	ith element
f	Frequency
f_{l}	Layer fill factor
H	Magnetic field intensity
H_{c}	Critical magnetic field intensity
H_{c1}	Lower critical magnetic field intensity
H_{c2}	Upper critical magnetic field intensity
H_{ext}	External magnetic field intensity
H_{p}	Penetration magnetic field intensity
$\mathbf{H}$	Magnetic field
$\mathbf{H}_{\mathrm{ext}}$	External magnetic field
h	Convective heat transfer coefficient
h_{s}	Relative step length
$\mathrm{I_c}$	Relation of element field and critical current
I	Transport current
I_{c}	Tape's critical current
I_{cable}	Test cable's current
I_{cm}	Measured critical current
I_{cr}	Tape's critical current obtained with Richardson extrapolation
I_{cs}	Simulated critical current
I_{e}	Element's current
I_i	Current of ith layer
I_{rms}	Root mean square value of oscillating fault current component
I_{t}	Rms value of tape current
I_{test}	Test current
$\overline{I}$	Phasor current of cable layer
$\overline{I}_{\mathrm{core}}$	Phasor current of cable core
i_{f}	Total instantaneous fault current
$i_{\mathrm{f},i}$	Instantaneous fault current in ith material
i_{n}	Normalized transport current
J	Magnitude of current density
J_{c}	Critical current density
J_{c0}	Zero field critical current density
J_{ca}	Average critical current density
J_{e}	Engineering critical current density
J_{new}	Critical current distribution of next iteration step
J_{old}	Critical current distribution of previous iteration step
$\mathbf{J}$	Current density
$\mathbf{J}_{\mathrm{YBCO}}$	Current density of YBCO

j	Imaginary unit
k	Thermal conductivity
N_c	Number of core layers
N_l	Number of tape layers
N_t	Number of tapes
N_x	Number of elements in x-direction
N_y	Number of elements in y-direction
n	Steepness of resistive transition
M	Inductance matrix
M_a	Axial part of inductance matrix
M_c	Circumferential part of inductance matrix
l	Cable length
l'	Lay length
l_t	Total length of tape needed for one cable meter
P	Total AC losses per cable length
P_ac	AC losses per tape length
P_ellipse	Self-field AC loss of elliptic superconductor
P_mag	Magnetization losses of one layer per cable length
P_self	Self-field AC losses per cable length
P_strip	Self-field AC loss of strip shaped superconductor
P_tm	Magnetization losses of one tape
p	Kim model parameter
q	Quantity
R	Resistance matrix
R_ac	Resistance due to AC losses
R_c	Contacts' resistance
$R_{\mathrm{c}1,i}$	First contact resistance
$R_{\mathrm{c}2,i}$	Second contact resistance
R_i	Resistance of ith cable layer per unit length
R_{ii}	ith diagonal element of resistance matrix
r	Radius
r_0	Cooling duct's radius
r_1	Former's radius
r_2	Substrate's radius
r_3	YBCO layer's radius
r_4	Silver shunt's radius
$\mathbf{r}$	Spatial vector
$\mathbf{r}'$	Vector pointing at current carrying element
S	Element cross-section area
S_cyl	Cross-section area of cylinder shaped return conductor
S_d	Cooling duct's cross-section area

S_f	Former's cross-section area
S_n	Sensitivity
S_tape	Tape's cross-section area
S_YBCO	YBCO layer cross-section area
T	Temperature
T^*	Critical temperature according to critical current model
T_0	Reference temperature
T_c	Critical temperature
T_YBCO	Temperature of YBCO
U_aux	Voltage of auxiliary loop
U_test	Test voltage
$\overline{V}_\mathrm{core}$	Phasor voltage of core layers
$\overline{V}_\mathrm{sh}$	Phasor voltage of shield layers
w	Width of superconducting layer
w_g	Gap width
α	Kim model exponent
α'	$J_\mathrm{c}(\mathbf{B})$-dependence parameter used in fault current analysis
β	Ratio of external and penetration field
Γ	Loss factor
γ	Anisotropic scaling factor
δ	Small positive real number
$\mathrm{\delta}$	Stoichiometric parameter
ϵ	Anisotropy factor
ε_max	Maximum value of absolute relative errors
$\varepsilon_\mathrm{mean}$	Mean value of absolute relative errors
η	Temperature ratio
θ	Angle between magnetic field and crystallographic c-axis
θ_ext	Angle between external magnetic field and c-axis
κ	Shape factor
μ_0	Permeability of free space
ρ	Resistivity
ρ_n	Normal state resistivity
ρ_sc	Superconducting state resistivity
ρ_YBCO	YBCO resistivity
τ	Fault current decay parameter
ϕ	Starting phase of fault current
φ	Lay angle
Ω_cyl	Cross-section of cylinder shaped return conductor
Ω_SC	Superconducting cross-section
Ω_YBCO	YBCO cross-section

Index of abbreviations

AC	Alternating current
BSCCO	Bismuth strontium calcium copper oxide
CC	Coated conductor
DC	Direct current
FEM	Finite element method
HBCCO	Mercury barium calcium copper oxide
HTS	High temperature superconductor
IBAD	Ion-beam-assisted deposition
LN_2	Liquid nitrogen
LTS	Low temperature superconductor
MOD	Metal organic deposition
PLD	Pulsed laser deposition
RABiTS	Rolling-assisted biaxially-textured substrate
rms	Root mean square
SC	Superconductor
SS1	First short sample
SS2	Second short sample
Super3C	EU-funded superconducting coated conductor cable project
TFA	Trifluoroacetate
YBCO	Yttrium barium copper oxide
YSZ	Yttria-stabilized zirconia

Chapter 1

Introduction

Superconducting (SC) cables can be used to transfer a large amount of power in a confined space. Especially in urban areas, these cables can be useful when power consumption increases and new cable ducts are expensive to build due to high land values. In addition, the energy transfer costs of superconducting cables are becoming competitive to conventional cables. However, considerable technical development is needed to widely commercialize this relatively new technology.

In 2004, an international project was started to study the feasibility of this technology with the aim of designing and constructing a 1-kA superconducting coated conductor cable (Super3C). In this work, computational tools were developed and used to electromagnetically design such a cable. Some of the results were compared to measurements of a 0.5-m prototype cable built during the project.

This chapter considers the history of electric cables from the first signal transmitting cables to today's superconducting cables based on high temperature superconductivity (HTS) and reviews some of the largest HTS cable projects. In addition, a detailed description is given of the motivation of this work and all its contributors.

1.1 Brief history of superconducting cables

Since a cable was first used to transmit electrical signals, the bottleneck has usually been insulation. In the first cable between New York and Jersey City under the Hudson River, conductors were insulated with gutta-percha, which is water-resistant but cannot withstand the heat generated in a power cable. Even in modern cables, in long-term use, insulation ages and dielectric losses are generated in it. These problems can be avoided by using overhead lines with the ambient air working as lossless insulation. A high voltage level also allows low currents and, thereby, decreases resistive losses. However, overhead networks are not suitable everywhere because they take a lot of valuable space in congested areas, cause fire hazards, and often visually mar the landscape. In addition, overhead lines are often exposed to storms and can be damaged by falling trees [124].

Often cables are the only choice though. Unfortunately, cable losses and, consequently, the cable's current is limited because soil cannot absorb more heat than 70 W m^{-1}. Simply increasing the cable's cross-section is not an efficient way to reduce losses because the skin effect forces the current close to the cable surface. However, this effect can be reduced with segmental conductor design [3]. Another way to increase the current is to bring down conductor resistance [96].

In 1911, Heike Kamerlingh Onnes discovered to his surprise that mercury lost its resistivity in liquid helium, a phenomenon later named superconductivity [82]. The first superconductors lost their superconducting properties at relatively low magnetic fields and were thus inadequate for power applications. During the 1960s, superconductors underwent a boom after the theory of superconductivity became established [5], and after new materials, which could operate, for example, in superconducting cables, were discovered. The most common of these superconductors are niobium tin (Nb_3Sn) and niobium titanium (NbTi), now called also low temperature superconductors (LTS) because they must usually be immersed in liquid helium [26, 96, 124].

At that time, energy consumption was predicted to increase dramatically and with it the need for power transmission lines with a capacity of several GVAs. Some plans were even made to use high capacity cables for transporting energy from conglomerates of nuclear plants to cities. Furthermore, many feasibility studies and prototype cables were made, including a 200-kV, 8 GW DC cable by AEG and a 110-kV, 1.9-GVA, three-phase AC cable by Siemens [96]. These systems boasted superior current densities and zero ohmic losses with no heat transmitted to the soil. However, superconducting wires were expensive, and operation costs sky-rocketed because of helium cooling. Therefore, cables based on LTS were competitive only in the highest power class. In the end, these high capacity cables did not become viable because power consumption did not increase as predicted. The story of superconducting power cables seemed to be over [96, 124].

A second superconductivity boom began in 1986 when J. G. Bednorz and K. A. Müller reported high temperature superconductivity (HTS) in a Ba-La-Cu-O system at 30 K [9]. A year later, an yttrium-based compound $YBa_2Cu_3O_{7-\delta}$ (YBCO) was found to be superconducting when cooled below 90 K [125]. This enabled liquid nitrogen cooling and dramatic cuts in cooling costs [26]. Once again, it seemed possible for superconducting cables to challenge conventional technology, especially in the moderate power class, below 1 GVA [96, 112]. A vigorous pursuit of commercial HTS conductors was launched, and it has so far focused on either YBCO- or bismuth-based compounds (BSCCO) [56].

1.2 HTS cable projects: an overview

In the late 1990s, when BSCCO conductors were the most promising for cable use, several BSCCO projects were started. The early 2000s became the golden age of BSCCO cable projects, and many prototype cables were installed in real power network. Recently, also the first YBCO projects have emerged. Some of the projects are summarized in table 1.1. All these systems are nitrogen-cooled AC cables and, therefore, operate at about 77 K.

To prove the feasibility of HTS cables, many projects have run tests on a real power grid. SouthWire Company installed industrial HTS cable system to power three of its main manufacturing plants [100] in Carrolton, Georgia. In Copenhagen, power was supplied via an HTS cable to about 50,000 utility customers of a public power grid. The cable showed no degradation during operation, which included varied load and short circuit currents and maintenance carried out by regular power company staff [110]. Field tests have also been run at Puji Substation of China Southern Power Grid [126] and an American Electric Power utility substation in Columbus, Ohio [35]. In Japan, a demonstration of single-core cable built in a SuperACE project showed that these cables can be wound on a shipping drum like conventional cables, and that they can cope with height variations, bent section, and vibrations typical of a real network in Japan [74]. During the Albany Project, a 320-m BSCCO cable was installed in the power grid of the Niagara Mohawk Power Company. Later, a 30-m section was replaced with a YBCO cable [69, 97, 107]. More projects are summarized in references [67] and [122].

The above-mentioned Super3C-project aims to construct a 30-m YBCO cable. When the project started in 2004, it was the world's first coated conductor cable project, comprising the development, manufacture, and testing of a single-core functional model. Though YBCO cables are in principle similar to BSCCO-based cables, many new technical difficulties that surfaced during the project must be overcome. In addition, after the cable is in operation in 2008, a lot of measurement data will be available for exploitation in future cable projects.

Table 1.1: HTS-based AC cable projects. BSCCO tapes are used as conductor unless otherwise mentioned.

Project or institution	Location	Year	Phases	Length (m)	Voltage (kV)	Power (MVA)
Pirelli [46]	Italy	1999	3	50	115	400
SouthWire [100]	Carrolton, US	2000	3	30	12.4	27
DTU and others [110]	Copenhagen, Denmark	2001	3	30	30	100
TEPCO and SEI [39]	Japan	2002	3	100	66	114
SCC and others [126]	Yunan province, China	2004	3	33.5	35	121
Albany [69]	Albany, US	2004	3	350	34.5	48
Super-ACE [74]	Japan	2004	1	500	77	77
Albany (YBCO) [69]	Albany, US	2006	3	30	34.5	48
Ultera/ORNL [35]	Columbus, US	2006	3	200	13.2	69
ASC and others [64]	Long Island, US	2007	3	660	138	574
Super3C (YBCO)	EU	2008	1	30	10	10

1.3 Motivation

This work concentrated on a superconductor-based technology for transferring energy. The technology introduced here can be used to improve the energy efficiency of power grids. Among the commercially available superconductors, YBCO-coated conductors were chosen here because of their rapidly developing energy transmission capability. In addition, their unit lengths are increasing fast and prices dropping as a result of their recent commercialization [67, 108, 112].

Compared to conventional cables, YBCO-coated conductors have the great advantage of obviating expensive cable tunnels in favor of small ducts. On the other hand, existing tunnels can be retrofitted with superconducting cables to increase power transmitting capacity [16, 96]. For example, a 1-GW cable with a diameter of only 130 mm can transmit the same power as six 138-mm conventional cables [112]. In addition, the transport current loss of the former compared to the power transmitted is less than that of the latter. So far though, HTS cables have been expensive mostly because of high conductor prices, but according to predictions YBCO cables will be cheaper and more efficient in densely populated areas, where tunnel building will constitute the bulk of total costs [38, 112, 113]. Therefore, cables are one of the most promising industrial application for HTS materials and YBCO predictably one of the most cost-efficient HTS material.

Generally, the design of a YBCO cable consists of three main aspects: mechanical, cryogenic, and electromagnetic design. This work focuses on the electromagnetic side, which can be further divided into three parts: determining the AC losses, modeling the cable critical current, and analyzing the fault current. When the Super3C project started, no suitable computational tools were available for cable design because the electromagnetic behavior of a superconductor is highly nonlinear and depends on numerous factors. Moreover, the cross-section of the current carrying part of the tape used in the cable may have a high aspect ratio, about 1:10,000. Here, computational tools were developed to overcome these problems.

In BSCCO-based coaxial cables, AC losses and current distribution have traditionally been determined in several ways. Flux conservation equations have been used with the power law to solve the problem [48, 111]. In addition, the three-dimensional finite element method (FEM) [99] has been exploited successfully [72] as well as a circuit-analysis-based approach [47, 78, 79]. Moreover, the two-dimensional FEM has been used in combination with circuit analysis to calculate losses in one-layer cables [37]. When this work was started, none of these analyses were performed on YBCO cables and, therefore, this work develops computational methods for YBCO cables and presents results for cables similar to the Super3C-cable.

The magnetic fields inside YBCO cables are of the same magnitude as the self-fields of YBCO tapes. The magnetic field changes the tapes' critical current, which further affects total AC losses. Thus it is important to know how the tapes are affected when they are installed in a cable. Consequently, an alternative method was developed to determine the critical current of the superconducting cable. This method requires the $J_c(\mathbf{B})$-model of the superconductor, which can be determined from voltage-current measurements performed at low fields. This method can be applied in applications other than cables as well.

Compared to conventional power cables, superconducting cables are more sensitive to fault currents due to extremely high current densities in their thin superconducting films. A high resistivity at overcritical currents and a small specific heat aggravate the situation. Therefore, it is essential that we can predict the cable's temperature and current transport properties during a short-circuit. Because in a modern power grid, the cables may have to withstand fault currents of up to 40 kA (rms), a nonlinear, time-dependent FEM model was developed to estimate the temperature distribution and current sharing in a YBCO cable during fault currents.

1.4 Structure of this work and contributors

Chapter 2 discusses the basics of superconductivity used in this work, introduces YBCO tapes and their electromagnetic properties and the different types of superconducting HTS cables. Chapter 3 introduces a circuit-analysis-based model to compute AC losses and current sharing in superconducting cables. This chapter summarizes publications I and II. Chapter 4 covers publications

III–V and presents the integral element method to compute critical currents on YBCO tapes and cables. The same method is also used to determine material electric field - current density characteristics from the tape's critical current measurements. The cable's critical current can be concluded from its material characteristics. Chapter 5 examines the effect of fault current on the YBCO cable in reference to publications VI and VII. The computational techniques discussed in the previous chapters are applied to the Super3C-cable presented in chapter 6 and in publication VIII. The chapter elaborates on the electromagnetic design work of the Super3C cable. Chapter 7 summarizes the work and its main results.

I developed and programmed all the algorithms used in the articles and wrote the manuscripts of papers I–VII. Dr. J. Lehtonen, adviser of this study, contributed to this thesis in many ways, providing, for example, a wealth of technical advice. He also gave me many new ideas and helped me with the writing process. Another major contributor was Dr. M. Masti, who was in charge of the design work on the Super3C-cable and helped with the modeling software at the start of the work. He also gave me some new ideas and valuable comments. The third important contributor was Lic. Tech. R. Mikkonen, head of our superconductor group, who made the final quality check on the papers for publication.

In publication II, the 0.5-m cable was designed and constructed by Doctors F. Gömöry, J. Šouc, E. Seiler, and T. Melíšek. They also measured the cable's current distribution and AC losses and described the measurements. Dr. A. Usoskin developed the superconducting tapes. In publication VI, Lic. Tech. L. Söderlund supervised the work. In publication VII, J. Šouc, E. Seiler, T. Melíšek, and M. Vojenčiak measured the critical current of the CC tapes in various external magnetic fields.

I edited publication VIII, the project coordinator Dr. J-M. Saugrain wrote the introduction, and Doctors A. Allais, K. Schippl, F. Schmidt, G. Balog and N. Lallouet the mechanical design section. Together with J. Lehtonen and M. Masti, I wrote the electromagnetic design, whereas Doctors G. Marot and A. Ravex wrote the cryogenics part. I wrote the final design in collaboration with J. Lehtonen and M. Masti, A. Allais drew up table 1, and F. Gömöry, J. Šouc, and B. Klinčok described the electric AC loss measurement technique. Dr. A. Usoskin developed the CC tapes, and Doctors A. Allais and G. Balog made the final revisions.

Chapter 2

Physical background

Traditionally, superconductors have been assumed to have no resistivity if their current density J, temperature T, and magnetic field intensity H are below the critical values. So far, the highest critical temperature, T_c = 135 K at normal pressure, has been measured for mercury barium calcium copper oxide ($HgBa_2Ca_2Cu_3O_{(8-\delta)}$) [127] with its critical current density at 77 K about tens of kA per square centimeter [14]. However, a 1,000 times higher value can be achieved when the temperature is lowered to 4 K [29]. Although, $YBa_2Cu_3O_{7-\delta}$ (YBCO) has a significantly lower critical temperature (92 K), its critical current density at 77 K can be as high as several million amperes per square centimeter [56]; therefore, it is well suited for applications that are cooled with liquid nitrogen (LN_2). Also YBCO coated conductors are mechanically strong [76, 87].

The magnetic fields at which HTS materials finally lose their superconductivity can exceed 100 T at 4 K [56, 96]. In practice, superconductor resistivity rises gradually from zero when J or T approach their critical values. In a magnetic field, superconductors behave in a more complex manner, and that is why their behavior is explained here first. That is followed by a discussion of the resistive transition with increasing J or T and a description of its mathematical representation, which forms the basis of electromagnetic and thermodynamic modeling. Although superconductors can carry a direct current without losses, alternating currents generate significant losses, which must be taken into account in cable design. Here, the theoretical basis of these losses is explained based on nonlinear resistivity. Unfortunately, AC losses are not the only constraint on cable design; other constraints arise from the mechanics and cryogenics. In addition, the cable must return to stable operation after fault currents.

2.1 Magnetization of superconductors

Superconductors are usually divided into two types according to their behavior in a magnetic field. In type I materials such as mercury, the current flows in the superconducting state on the material's surface only, where the current distribution is characterized by the London penetration depth. The material is in the Meissner state, which means that it works as a perfect diamagnet in which H is zero. If its critical magnetic field intensity H_c is exceeded, the superconductor immediately returns to its normal conducting state. Unfortunately, type I materials lose superconductivity in magnetic fields that are typically less than 0.1 T, and are, therefore, unsuited for most applications [96].

In contrast, type II superconductors such as YBCO, can operate at much higher fields. They are characterized by lower and upper critical fields H_{c1} and H_{c2}, respectively. Below H_{c1}, the material behaves exactly like type I superconductors. Between the critical fields, the material is partially superconducting, and the external field penetrates into the material as fluxoids, which adhere to the normal conducting pinning centers. When the external field is increased to the full penetration field value H_p, the flux penetrates the whole superconductor. Finally, superconductivity is lost at H_{c2} [26, 96, 123]. For HTS materials, H_{c2} is usually tens of teslas at 77 K, which is far above the application fields [96]. H_p and H_{c2} can be spotted on the sketched magnetization curve in figure 2.1.

The most widely used type II superconductors are niobium titanium (NbTi) and niobium tin (Nb_3Sn) with critical temperatures of 9.1 and 18.3 K, respectively [84]. Also all known HTS materials, including BSCCO and YBCO, are type II superconductors [26]. In HTS materials, superconductivity is based on copper oxide planes, which make these materials strongly anisotropic; consequently, their superconducting properties are much better along the CuO_2 planes than in the direction normal to them [36]. These copper oxide planes are shown in the diagram of the crystallographic structure of YBCO in figure 2.2.

2.2 Electromagnetic model for HTS

In cable applications, the electromagnetic behavior of HTS conductors is described by Maxwell's equations assuming that the displacement current is zero due to the small frequency $f = 50$ Hz of AC power cables. That is, Ampère's law is written as

$$\nabla \times \mathbf{H} = \mathbf{J}. \tag{2.1}$$

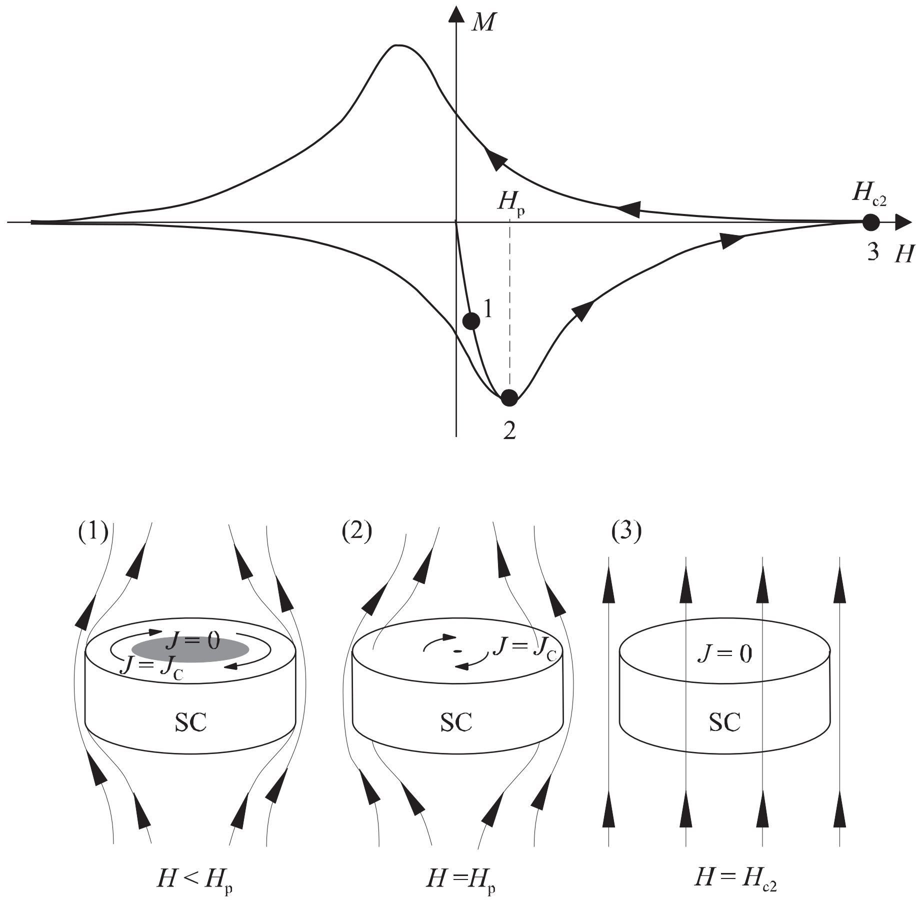

Figure 2.1: Magnetization curve of type II superconductor. Also shown are shielding currents related to different phases of magnetization. Superconductor is diamagnetic due to induced shielding current, and external magnetic field H_{ext} is below penetration field H_{p}. When $H_{\text{ext}} = H_{\text{p}}$, shielding current and magnetic field penetrate fully into material and saturate superconductor. When $H_{\text{ext}} > H_{\text{p}}$, shielding current start to decay and finally reaches zero when $H_{\text{ext}} = H_{\text{c2}}$.

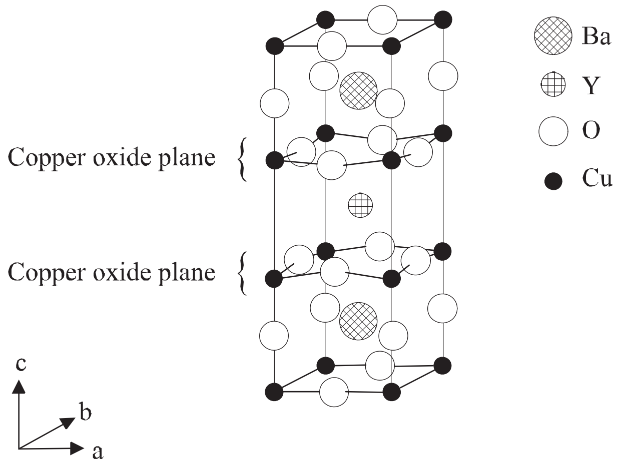

Figure 2.2: Crystallographic structure of YBCO.

Furthermore, because magnetization is created by supercurrents, not by magnetization currents, the permeability of the free space μ_0 is applied [92]. These assumptions lead to the magnetic diffusion equation

$$\nabla \times \rho \nabla \times \mathbf{H} = -\mu_0 \frac{\partial \mathbf{H}}{\partial t}, \tag{2.2}$$

which is solved numerically using, for example, the finite element method (FEM) [12, 99]. The highly nonlinear resistivity ρ is difficult to model because it depends on the current density $\mathbf{J}$, the magnetic field intensity $\mathbf{H}$, and the temperature T.

In stability considerations, equation 2.2 is solved together with the heat conduction equation

$$\nabla \cdot k \nabla T + \rho \left| \nabla \times \mathbf{H} \right|^2 = C_\mathrm{p} \frac{\partial T}{\partial t}, \tag{2.3}$$

where $k(T)$ is the thermal conductivity and $C_\mathrm{p}(T)$ the volumetric specific heat [40]. $H(t)$ and $T(t)$ were solved from the resultant system of equations. Practically, cross dependencies between the variables exacerbate solving the problem numerically. In this work, one-dimensional stability analysis was done.

2.3 Resistivity of YBCO

The transition between superconducting and normal conducting states characterizes the resistivity of YBCO. Here superconducting state resistivity was assumed to follow the power law [96] as

$$\rho_{\mathrm{sc}} = \frac{E_{\mathrm{c}}}{J_{\mathrm{c}}} \left(\frac{J}{J_{\mathrm{c}}} \right)^{n-1}, \tag{2.4}$$

where J_{c} is the critical current density corresponding to the typical electric field criterion $E_{\mathrm{c}} = 1\ \mu\mathrm{V\ cm}^{-1}$, and n defines the steepness of the transition. J_{c} corresponds roughly to the current density where the transition occurs. The transition of LTS materials is very steep with n values exceeding 40 [86], and even 130 has been reported [41]. In contrast, BSCCO tapes have values of about 10–20 [89, 130], whereas YBCO shows values of over 30 [94, 95].

Note though that these n-values are originally measured for conductors, and n as a material property may differ. The n-value of a conductor can be reduced by nonhomogeneities along the conductor [120] and by its self-field [68]. On the other hand, the n-value can increase spuriously if the temperature rises during the measurement [105]. Indeed, the resistivity of YBCO is sensitive to temperature.

In cable applications, temperature begins to be of interest from 70 K [19] on, and reaches well above T_{c}, where YBCO is in the normal state having normal state resistivity ρ_{n}. On the other hand, at a high J, the power law can suggest a higher than normal resistivity value. Therefore, the whole resistivity of YBCO was modeled as

$$\rho_{\mathrm{YBCO}} = \min(\rho_{\mathrm{n}}, \rho_{\mathrm{sc}}). \tag{2.5}$$

As an alternative to the power law, the Bean model [7] can be safely used because the relatively high n-value of YBCO justifies it. In fact, the Bean model is a special case of the power law, where $n \to \infty$; consequently, J is limited to two values, either 0 or J_{c}. The power law and the Bean model are compared in figure 2.3. Unfortunately, most commercial FEM software packages cannot manage the sudden jump in resistivity and its derivative. Therefore, the smooth power law was used here. However, this is not the only way to model resistivity. Other models have been developed, for example, by Ambegaokar and Halperin [2, 102], Yamafuji and Kiss [129], Majoros [65], and Dew-Hughes [23]. In fact, n depends on $\mathbf{J}$, $\mathbf{H}$, and T, but commercial FEM codes are usually unable to solve the problem, or considerably more computation time is needed if variable n is used. However, the results were not greatly affected whether n was 30 or 50; therefore, the assumption of a constant n for YBCO was justified.

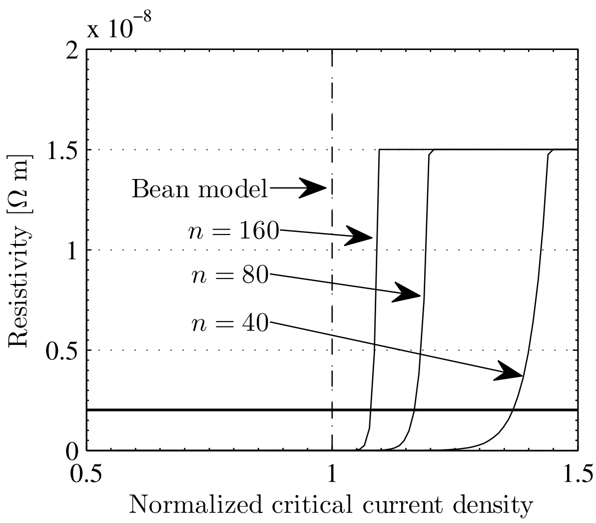

Figure 2.3: Resistivity models of YBCO as function of normalized critical current density. Shown for comparison are both Bean model (dashed line) and resistivity of pure copper at 77 K [42] (thick line).

2.4 Critical current density and critical surface

According to equation 2.4, J_c is the current density at which E reaches one microvolt per centimeter. However, there are several other, even confusing definitions of critical current density [96], but with every criterion J_c depends strongly on $\mathbf{H}$ and T [26]. When H is clearly below H_{c2}, the magnetic field dependence of the critical current density follows the Kim model [49]. Because J_c depends also on the orientation of $\mathbf{H}$, the following extended Kim model was used here:

$$J_c \propto \left(1 + \frac{\epsilon \mu_0 H}{B_0}\right)^{-\alpha}, \tag{2.6}$$

where B_0 is the reference field, and α is the Kim model exponent [32, 34].[1] Anisotropy is taken into account with the factor

$$\epsilon = \sqrt{\cos^2(\theta) + \gamma^{-2}\sin^2(\theta)}, \tag{2.7}$$

where θ is the angle between $\mathbf{B}$ and the crystallographic c-axis, and γ is the anisotropic scaling factor [11]. The resulting $J_c(\mathbf{B})$-dependence of YBCO is shown in figure 2.4.

[1] Publication IV makes use of a different form of the Kim model, whereas a more accurate model is used here. Both models are still widely used [83, 106].

Because J_c drops almost linearly as T changes [52], the following approximation was used:

$$J_c \propto \frac{T^* - T}{T^* - T_0},\ T < T^*, \tag{2.8}$$

where the reference temperature, T_0, was chosen to be 77 K. T^* is the temperature at which the fitted critical current drops to zero and is slightly below the critical temperature. Here T^* was 89 K, and according to equation 2.8, the critical current decreases about 8% per 1 K. Thus even a little heating can decrease the conductor's critical current. On the other hand, the cable's critical current can be increased by lowering the operation temperature by regulating the pressure.

Combining equations 2.6 and 2.8 leads to the function

$$J_c(H, T) = \left(1 + \frac{\epsilon \mu_0 H}{B_0}\right)^{-\alpha} \cdot \frac{T^* - T}{T^* - T_0} \cdot J_{c0},\ T < T^*, \tag{2.9}$$

where J_{c0} is zero field critical current density. Since in the real world, T^* depends only slightly on $\mathbf{H}$ [52], the $J_c(\mathbf{H}, T)$-dependence can be replaced with a more accurate model when more measured data is available. Here, equation 2.9 was used as the best available model. The corresponding critical surface is shown in figure 2.5, assuming that $\mathbf{H}$ is parallel to the ab-plane ($\theta = 90°$).

2.5 YBCO tapes and their fabrication

Today, practically all commercial YBCO tapes are coated conductors (CC), which means that the superconductor is deposited on a metallic substrate. Most substrates are nickel-based alloys such as Hastelloy [121] or simply stainless steel [115]. Unfortunately, the YBCO texture does not match directly these substrates, and at least one buffer layer is needed in between. Usually, the buffer layer consist of a CeO_2 layer and $SrTi0_3$- or Y_2O_3-stabilized ZrO_2 (YSZ) [56, 90], and buffer layers are currently developed to boost the tape's performance [128]. Usually, the buffer layer is deposited on the substrate by sputtering with the help of an assisting Ar-ion gun, a process called ion-beam-assisted deposition (IBAD) [119]. Another option is to texture the substrate by rolling and annealing. After that, buffer layers are grown on the substrate by a method called rolling-assisted, biaxially-textured substrate (RABiTS) [81].

There are also two common ways to deposit YBCO. In pulsed laser deposition (PLD), YBCO is evaporated in a low-pressure oxygen atmosphere [93]. This method results in high J_{c0} values and is so far the best way to manufacture high-quality YBCO. However, the use of a vacuum complicates

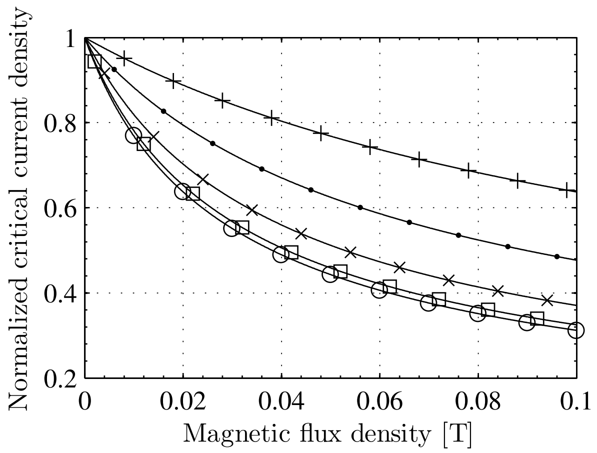

Figure 2.4: Critical current density of YBCO at 77 K as function of external magnetic flux density at different field orientations: (○) $\theta = 0°$, (□) 22.5°, (×) 45°, (●) 67.5° and (+) 90°. YBCO material is characterised with Kim model parameters: $J_{c0} = 3 \cdot 10^{10}$ A m^{-2} [13], $B_0 = 20$ mT [13], $\alpha = 0.65$ [30] and $\gamma = 5$ [18].

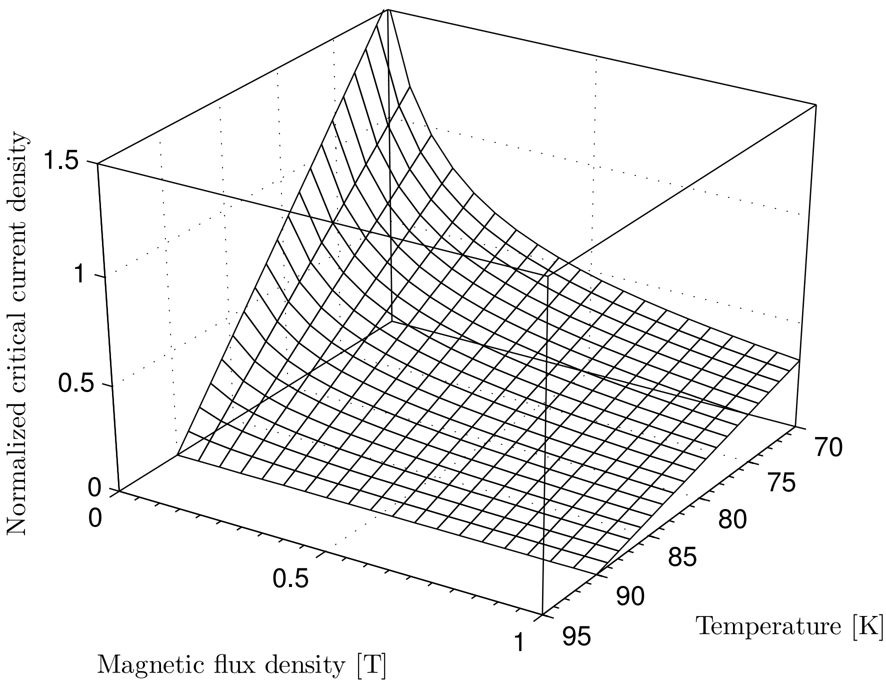

Figure 2.5: Critical surface model used in computations. Magnetic field is oriented parallel to crystallographic ab-plane.

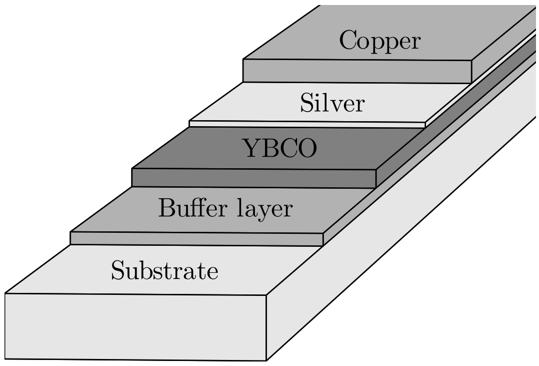

Figure 2.6: Layers of possible YBCO tape structure. Dimensions are not to scale. Typically, thicknesses of substrate, buffer layer, YBCO, and silver sheath are 0.05–0.1 mm, 300 nm, 0.5–3 µm, and 0.5 µm with often also about 0.1 mm thick copper stabilization layer on YBCO.

the tape's manufacture. No vacuum, however, is needed in metal organic deposition (MOD), in which YBCO is deposited chemically on the substrate. MOD yields satisfactory J_c values over 1 MA cm^{-2} with metal trifluoroacetate (TFA), which is placed on the substrate. After heat treatment, YBCO is formed [109]. Regardless of the deposition method, the substrate is usually about 0.1 mm thick and 1 cm wide. Depending on the application the tapes are then cut into narrower strips if needed [95]. A sketch of the tape is shown in figure 2.6.

2.6 AC losses in YBCO tape

In BSCCO multifilamentary tapes, AC losses are traditionally divided into three components: losses in the superconductor, losses created by the electromagnetic coupling between filaments, and eddy current losses in the matrix metal [88, 96]. CC tapes have no coupling losses, because the superconductor consists of only one film. Also the eddy current losses are negligible [25].

In the superconducting cross-section Ω_{SC}, the time-varying field induces an electric field in the material by Faraday's law; thus resistive power per meter is generated as follows:

$$P_{\mathrm{ac}} = \int_{\Omega_{\mathrm{SC}}} \mathbf{E} \cdot \mathbf{J} \mathrm{d}s = \int_{\Omega_{\mathrm{SC}}} \rho \left| \nabla \times \mathbf{H} \right|^2 \mathrm{d}s. \tag{2.10}$$

Using the right hand side of the equation, AC losses can be directly computed from $\mathbf{H}$ solved from equation 2.2. The time-varying field originates from the

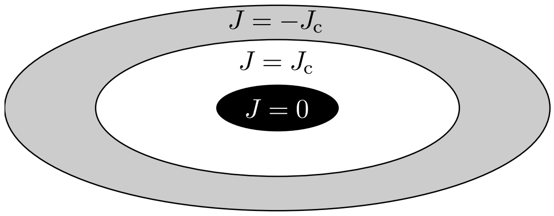

Figure 2.7: Remanence current distribution of elliptic conductor according to Bean model. First, AC current has penetrated almost whole superconductor. Then transport current has dropped back to zero; consequently, only remanence current circulates in material.

time-varying current of the superconductor itself $\mathbf{J}_{\mathrm{YBCO}}$ and from an external magnetic field $\mathbf{H}_{\mathrm{ext}}$.

The AC losses of a bulk superconductor can be roughly divided into transport current losses and magnetization losses [88]. In the former, the time varying field is caused only by $\mathbf{J}_{\mathrm{YBCO}}$. If the transport current is zero with a time varying $\mathbf{H}_{\mathrm{ext}}$, the generated losses are so-called magnetization losses. Of course, the losses can arise from a combination of transport current and magnetization losses. In that case, total losses are often approximated by computing separately magnetization losses and self-field losses and then adding them up [88].

For two simple cross-section shapes, strip and ellipse, AC losses can be calculated analytically as derived from the Bean model by Norris as follows:

$$P_{\mathrm{strip}} = \frac{\mu_0 I_{\mathrm{c}}^2 f}{\pi} \left[(1-i_{\mathrm{n}})\log(1-i_{\mathrm{n}}) + (1+i_{\mathrm{n}})\log(1+i_{\mathrm{n}}) - i_{\mathrm{n}}^2\right] \tag{2.11}$$

$$P_{\mathrm{ellipse}} = \frac{\mu_0 I_{\mathrm{c}}^2 f}{\pi} \left[(1-i_{\mathrm{n}})\log(1-i_{\mathrm{n}}) + (2-i_{\mathrm{n}})\left(\frac{i_{\mathrm{n}}}{2}\right)\right], \tag{2.12}$$

where $i_{\mathrm{n}} = \sqrt{2}I/I_{\mathrm{c}}$ and I is the rms value of the AC transport current at frequency f [80].

The strip model is a natural choice for a YBCO tape, but measurements suggest that the tape's AC losses follow the ellipse model [66, 118]. Both equations assume a constant critical current density across the tape cross-section, as shown in figure 2.7, an assumption that is not exactly correct, because the critical current is affected by the self-field. Due to the nonhomogeneous critical current distribution across the cross-section, the ellipse agrees better with measurements.

2.7 HTS cables

HTS cables are intended for transferring a high amount of energy in a confined space with the lowest possible losses. The losses comprise termination losses, dielectric losses, cryogenic losses, and AC losses, which are zero for direct current (DC) cables. Unfortunately, DC cables cannot be installed in a power grid without converters [96].

A high critical current is achieved in the cables by connecting several strip-like conductors in parallel. HTS cables are without exception cooled with liquid nitrogen (LN_2), which is liquefied by a cooling system that pumps LN_2 into the cryostat through terminations. Thus a cryostat with LN_2 circulation is also needed.

The terminations act as a link between the grid and the cable. Well designed terminations distribute the current evenly between the tapes, and their losses are kept minimal. The cryostat insulates the cold parts of the cable from the ambient temperature. In practice, the cryostat can be a liquid nitrogen transport line, which consists of two flexible tubes inside each other. Its thermal insulation consists of a high-level vacuum and super-insulation layers between the tubes.

There are two possibilities to arrange the phases in a three-phase cable: the phases can be kept on one cable, or a separate cable can be made for each phase. In effect, the latter means the construction of three 1-phase cables, which is exactly what the first HTS cables were like [110].

Some of the first cables were often of the so-called warm dielectric type, in which only the core conductors were cooled whereas the return conductor was not superconducting but conventional. Alternatively, the superconducting return conductor, also known as the shield conductor, can be placed into the cryostat, in which case the core and return conductors must be separated by the dielectric, which is also cooled. This cable is the cold dielectric type. Some of the most common designs are summarized in figure 2.8 and compared in table 2.1.

In addition to the dielectric, the cold part of the cold dielectric cables consists usually of a copper former and superconducting tapes, which are wound on the former to prevent tape movements and mechanical fatigue and to ensure flexibility of the cable. In cold dielectric cables, the dielectric is then on the tapes with shield conductors placed over the dielectric.

The former is usually a standard multi-segmented and twisted copper cable, in which the strands are braided to reduce eddy current losses. It is useful if the cable's nominal transport current is exceeded, because the former acts as a shunt. However, the copper former can be excluded if the cable is designed to operate also as a fault current limiter [58].

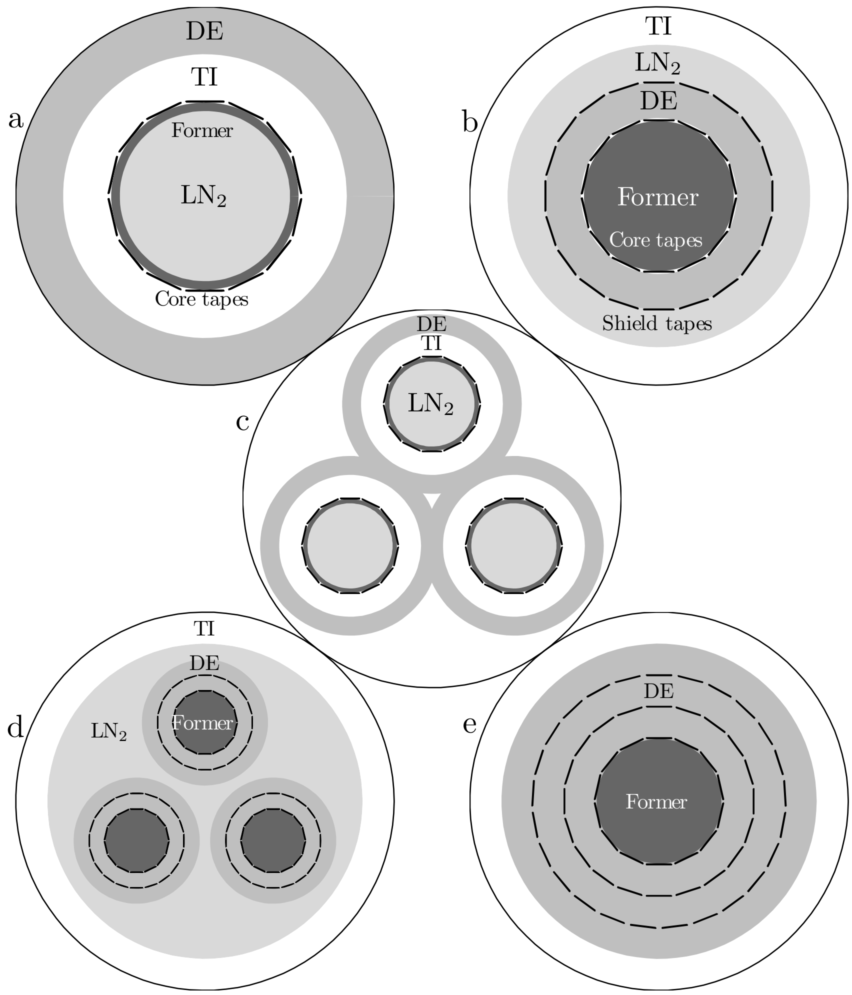

Figure 2.8: Cross-sections of most common HTS cable types. (a) Warm dielectric type cable which core layer is surrounded by thermal insulation (TI) and dielectric (DE) layers [110]. (b) Cold dielectric cable (Super3C). (c) Three-phased warm dielectric cable [46]. (d) Three-phased cold dielectric triaxial cable [39]. (e) Three-phase cold dielectric coaxial cable [35]. The cold dielectric is often impregnated with LN_2.

Table 2.1: Some advantages and disadvantages of three-phased cable types.

Dielectric	Phases	Advantages	Disadvantages
Warm	Separate	Conventional dielectric	Cryostats' losses
		Fewer tapes needed	Inductive coupling
		Low initial cost	Return conductors' losses
		Reliable structure	Space requirement
Warm	Triaxial	Compact design	Inductive coupling
		Conventional dielectric	High losses
		Fewer tapes needed	Tapes' c-axis oriented fields
		Low initial cost	
Cold	Separate	Dielectric losses	Cryostats' losses
		Simple design	Plenty of tapes needed
			Space requirement
Cold	Triaxial	Compact design	More tapes needed
Cold	Coaxial	Compact design	Inductive coupling

Chapter 3

AC losses and current sharing

In HTS cables, AC losses are the most important electrical loss factor. In order to rate the cooling system, it is essential to predict AC loss accurately. In this work, AC losses were determined for coaxial YBCO cable design using the circuit-analysis-based computational model. In an equivalent circuit, superconducting layers are connected in parallel, the layers have an inductive coupling between them, and AC loss within a layer generates an effective resistance. Layer currents can then be solved from a set of circuit equations. The computational model takes into account the fact that the current in the cable creates a magnetic field, which generates a small magnetization loss but affects strongly the critical current of the YBCO tapes.

The model was here applied to several coaxial superconducting YBCO cable designs with nominal currents of 1–10 kA (rms) and predictably low AC loss values. For example, AC losses of less than 4 W m^{-1} were predicted for 10-kA cables. In addition, a circuit analysis model was used to determine AC losses and current sharing of a 0.5-m, one-layer cable, constructed to test the behavior of a real YBCO cable. AC losses measured for this cable agreed well with computed results, verifying thus the feasibility of the developed design tool. However, measurements revealed that differences in contact resistances caused uneven current sharing between the tapes, whereas computational analysis predicted current sharing to be almost even in a 30-m cable.

3.1 Circuit analysis model for cable AC losses

AC losses and current sharing in coaxial BSCCO cables have been calculated in several ways [20, 37, 47, 48, 72, 78, 79, 111]. Here, a circuit-analysis-based approach was chosen to determine AC losses and critical current of the superconducting coaxial YBCO cables. The choice was made because Noji et al.

have developed a fast, circuit analysis based model to compute AC losses in multi-layer superconducting cables. Noji's model has been successfully used in BSCCO cable projects [78, 79]. In this work, the model was applied to the design of YBCO cables after its theoretical basis was first improved.

3.1.1 Model overview

The aim was to estimate AC losses in a coaxial superconducting cable with N_l layers. A scheme of one layer is shown in figure 3.1. A widely used approximation for total AC losses P is the sum of the self-field losses P_{self} and magnetization losses P_{mag} of all the superconducting layers [63]

$$P = \sum_{i=1}^{N_l} P_{\mathrm{self},i} + \sum_{i=1}^{N_l} P_{\mathrm{mag},i}. \tag{3.1}$$

For the ith layer, $P_{\mathrm{self},i}$ is the sum of the self-field loss of the individual tapes. This loss is computed according to the Norris strip approximation, equation 2.11. Due to the twist in the layer, the self-field loss, P_{strip}, is then scaled to per cable length. The model is restricted to sub-critical currents, because practical cables do not operate at overcritical current. Exceptionally, overcritical currents occur in fault operation, considered in section 5.

The magnetization loss in the ith layer is

$$P_{\mathrm{mag},i} = N_{\mathrm{t},i} P_{\mathrm{tm},i}, \tag{3.2}$$

where $N_{\mathrm{t},i}$ is the number of tapes and $P_{\mathrm{tm},i}$ the tape's magnetization loss in the ith layer. The tape is considered a current-carrying superconducting slab in the parallel magnetic field B. Therefore, the magnetization loss of one tape is

$$P_{\mathrm{tm}} = \frac{B_{\mathrm{p}}^2 S_{\mathrm{YBCO}} f}{3\mu_0}\Gamma, \tag{3.3}$$

where Γ is the loss factor, S_{YBCO} is the YBCO layer cross-section in the tape, and f is the frequency of the transport current. The penetration field of ith layer is defined as

$$B_{\mathrm{p},i} = \frac{I_{\mathrm{c},i}\mu_0}{2w} \tag{3.4}$$

for every layer. $I_{\mathrm{c},i}$ is the critical current of the tape in the ith layer and w the tape width. The loss factor for one layer is written as

$$\begin{cases} \Gamma = (\beta + i_\mathrm{n})^3 + (\beta - i_\mathrm{n})^3, & \text{for } i_\mathrm{n} \leq \beta \leq 1 \\ \Gamma = 2\beta\left(3 + i_\mathrm{n}^2\right) - 4\left(1 - i_\mathrm{n}^3\right) + \frac{12 i_\mathrm{n}^2 (1-i_\mathrm{n})^2}{\beta - i_\mathrm{n}} - \frac{8 i_\mathrm{n}^2 (1-i_\mathrm{n})^3}{(\beta - i_\mathrm{n})^2}, & \text{for } i_\mathrm{n} \leq 1 \leq \beta \\ \Gamma = (i_\mathrm{n} + \beta)^3 + (i_\mathrm{n} - \beta)^3, & \text{for } \beta \leq i_\mathrm{n} \leq 1 \end{cases}, \tag{3.5}$$

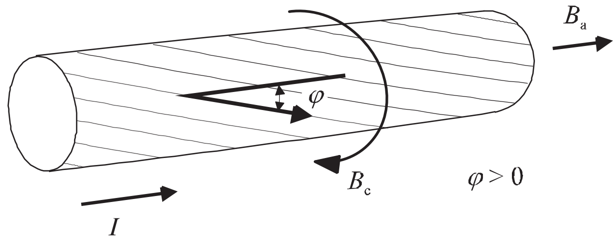

Figure 3.1: One layer of superconducting YBCO cable with transport current flowing rightwards. Tapes in layer are laid right-handed. Shown also are directions of axial and circumferential magnetic flux densities.

where i_n is the peak value of the tape transport current per tape critical current, and β is the ratio B/B_p [15]. The external magnetic flux density is assumed parallel to the tape surface and perpendicular to the current density.

To determine the cable's self-field and magnetization loss, currents in each layer must be solved as well as the external magnetic flux densities and the critical currents of the tapes in separate layers. The computational model consists of three parts. The first solves the phasor currents $\overline{I}_i$ in all layers; the second computes the norm of the external magnetic flux densities B_i from $\overline{I}_i$; and the third calculates the critical currents $I_{\mathrm{c},i}$ from B_i. The third part is important because the critical current of a YBCO tape depends strongly on the external magnetic flux density [85]. Figure 3.2 shows how to solve $I_{\mathrm{c},i}$.

3.1.2 Magnetic fields

$I_{\mathrm{c},i}$ was computed from B_i and measured $I_\mathrm{c}(B,T)$ data. The next step was to determine B_i, which was computed as

$$B_i = \sqrt{\overline{B}_{\mathrm{c},i}\overline{B}^*_{\mathrm{c},i} + \overline{B}_{\mathrm{a},i}\overline{B}^*_{\mathrm{a},i}}, \tag{3.6}$$

where $\overline{B}_{\mathrm{a},i}$ and $\overline{B}_{\mathrm{c},i}$ are the tape's external axial and circumferential magnetic flux density in the ith layer. Due to the time harmonic field, phasors were used. The field directions at peak transport current are shown in figure 3.1. The magnetic flux density consists of two components: one caused by the current flowing in the ith layer and the other by currents in the other layers.

$$\begin{cases} \overline{B}_{\mathrm{c},i} = \overline{B}_{\mathrm{c,self},i} + \overline{B}_{\mathrm{c,amb},i} \\ \overline{B}_{\mathrm{a},i} = \overline{B}_{\mathrm{a,self},i} + \overline{B}_{\mathrm{a,amb},i} \end{cases} \tag{3.7}$$

$\overline{B}_{\mathrm{c,self},i}$ and $\overline{B}_{\mathrm{a,self},i}$ are the circumferential and axial components of the magnetic flux density caused by the current in the ith layer, whereas $\overline{B}_{\mathrm{c,amb},i}$ and

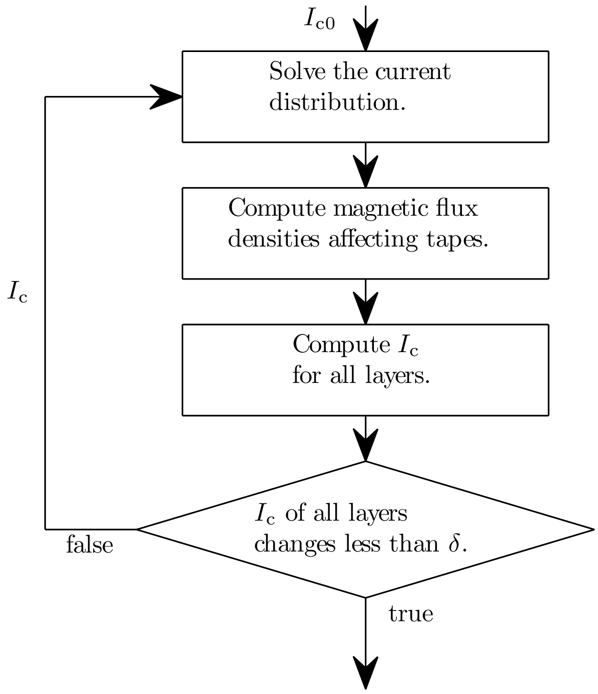

Figure 3.2: Block diagram of iterative computations of critical currents for all layers. δ is a small positive real number determining convergence criterion.

$\overline{B}_{\mathrm{a,amb},i}$ are the ambient magnetic flux densities caused by the currents in the other layers. Inside the cylinder, the circumferential magnetic flux density component is zero. Correspondingly, outside the cylinder, the axial magnetic flux density component is zero. The magnetic fields created by layers $s \neq i$ are

$$\begin{cases} \overline{B}_{\mathrm{c,amb},i} = \sum_{s=1}^{N_\mathrm{l}} \overline{B}_{\mathrm{c,amb},i,s} \\ \overline{B}_{\mathrm{a,amb},i} = \sum_{s=1}^{N_\mathrm{l}} \overline{B}_{\mathrm{a,amb},i,s} \end{cases}, \tag{3.8}$$

where $\overline{B}_{\mathrm{c,amb},i,s}$ and $\overline{B}_{\mathrm{a,amb},i,s}$ are the circumferential and axial components of the magnetic flux densities in the ith layer created by the current in the layer s. For ideal, infinitely long current-carrying cylinders, the transport current is assumed to flow at a constant angle to the cable axis. The magnetic fields are computed with Ampère's law as

$$\begin{cases} \overline{B}_{\mathrm{c,amb},i,s} = \frac{\mu_0 \sqrt{2} I_s}{2\pi r_i}, & \text{if } s < i, \quad \text{otherwise } \overline{B}_{\mathrm{c,amb},i,s} = 0 \\ \overline{B}_{\mathrm{a,amb},i,s} = \frac{\mu_0 \sqrt{2} I_s}{\mathrm{sgn}(\varphi_i) l'_i}, & \text{if } i < s, \quad \text{otherwise } \overline{B}_{\mathrm{a,amb},i,s} = 0 \end{cases}, \tag{3.9}$$

where r_i is the radius of the ith YBCO layer. l' is the lay length, and $\mathrm{sgn}(\varphi_i)$ is the sign of the lay angle, which is positive for the right-handed twist and negative for the left-handed twist. For ideal cylinders, the perpendicular magnetic flux density is zero.

Ampère's law cannot be used directly with one tape to compute the external magnetic flux density in one tape generated by the other tapes in the layer. Therefore, $\overline{B}_{\mathrm{c,self},i}$ and $\overline{B}_{\mathrm{a,self},i}$ are approximated as the mean value of the magnetic flux density outside and inside the current-carrying cylinder.

$$\begin{cases} \overline{B}_{\mathrm{c,self},i} = \frac{1}{2}\left[0 + \frac{\mu_0 \sqrt{2} I_i}{2\pi r_i}\right] = \frac{\mu_0 \sqrt{2} I_i}{4\pi r_i} \\ \overline{B}_{\mathrm{a,self},i} = \frac{1}{2}\left[\frac{\mu_0 \sqrt{2} I_i}{\mathrm{sgn}(\varphi_i) l'_i} + 0\right] = \frac{\mu_0 \sqrt{2} I_i}{2\mathrm{sgn}(\varphi_i) l'_i} \end{cases} \tag{3.10}$$

To assess the validity of equation 3.10, accurate magnetic fields were also computed. These exact computations are time-consuming and should thus not be implemented in a practical design tool. Here, results are shown for the layer with the smallest studied radius, 15 mm, because equation 3.10 becomes more accurate when the radius increases. The transport current of the layer was 1 kA (rms), and 22 tapes were twisted with a 10° lay angle. For the circumferential field, YBCO layers in the tapes were modeled as current-carrying rectangles, and the magnetic flux densities of these rectangles were then computed analytically and summed up according to the superposition principle [10]. The external circumferential magnetic flux density averaged over the YBCO cross-section was 9.3 mT when equation 3.10 gave 9.4 mT. The external axial field in the YBCO layer was integrated numerically from the Biot-Savart law. The agreement was satisfactory since the mean value of the external axial field inside the YBCO layer was 1.50 mT, whereas equation 3.10 predicted 1.66 mT.

3.1.3 Circuit equations

The last task was to solve the layer currents in an equivalent circuit of the cable shown in figure 3.3. When $\mathbf{x}$ contains layer currents, voltage of the core $\overline{V}_{\mathrm{core}}$, and voltage of the shield $\overline{V}_{\mathrm{sh}}$ as $\mathbf{x} = \left[\overline{I}_{1\times N_{\mathrm{l}}}\ \overline{V}_{\mathrm{core}}\ \overline{V}_{\mathrm{sh}}\right]^{\mathrm{T}}$, circuit equations are written as

$$R(\mathbf{x})\,\mathbf{x} + D\mathbf{x} = \mathbf{b}, \tag{3.11}$$

where $R(\mathbf{x})$ is the matrix containing nonlinear resistances, D the linear part of the system containing the self- and mutual inductances, and $\mathbf{b}$ consists of the current source terms. If the number of the core layers is denoted by N_{c}, then there are $N_{\mathrm{l}} - N_{\mathrm{c}}$ shield layers. Now, the first N_{c} equations are obtained from the fact that the voltage over the layers $1, \ldots, N_{\mathrm{c}}$ must equal $\overline{V}_{\mathrm{core}}$. Correspondingly, the condition that the voltage over the layers $N_{\mathrm{c}} + 1, \ldots, N_{\mathrm{l}}$ must equal $\overline{V}_{\mathrm{sh}}$ produces the next $N_{\mathrm{l}} - N_{\mathrm{c}}$ equations. By Kirchhoff's law of currents, the final equations require that the sum of all the layer currents is zero, and that the current flowing in the core equals $\overline{I}_{\mathrm{core}}$, thus

$$\sum_{i=1}^{N_{\mathrm{l}}} \overline{I}_i = 0 \text{ and } \overline{I}_{\mathrm{core}} = \sum_{i=1}^{N_{\mathrm{c}}} \overline{I}_i \tag{3.12}$$

and

$$\mathbf{b} = \begin{bmatrix} \mathbf{0}_{N_{\mathrm{l}}\times 1} \\ \mathbf{0} \\ \overline{I}_{\mathrm{core}} \end{bmatrix} \text{ and } R = \begin{bmatrix} \operatorname{diag}(R_i) & \mathbf{0}_{N_{\mathrm{l}}\times 2} \\ \mathbf{0}_{2\times N_{\mathrm{l}}} & \mathbf{0}_{2\times 2} \end{bmatrix}, \tag{3.13}$$

where the resistance R_i of the ith layer due to self-field losses is given as

$$R_i = \frac{1}{\cos(\varphi_i)} \cdot \frac{N_{\mathrm{t},i} P_{\mathrm{strip},i}}{I_i^2} \ \left(\Omega\ \mathrm{m}^{-1}\right). \tag{3.14}$$

Because the critical state model is assumed here, DC losses are zero.

Finally, D is written as

$$D = \begin{bmatrix} \mathrm{j}2\pi f M_{N_{\mathrm{l}}\times N_{\mathrm{l}}} & \begin{bmatrix} \mathbf{1}_{N_{\mathrm{c}}\times 1} & \mathbf{0}_{N_{\mathrm{c}}\times 1} \\ \mathbf{0}_{(N_{\mathrm{l}}-N_{\mathrm{c}})\times 1} & \mathbf{1}_{(N_{\mathrm{l}}-N_{\mathrm{c}})\times 1} \end{bmatrix} \\ \begin{bmatrix} \mathbf{1}_{1\times N_{\mathrm{c}}} & \mathbf{1}_{1\times (N_{\mathrm{l}}-N_{\mathrm{c}})} \\ \mathbf{1}_{1\times N_{\mathrm{c}}} & \mathbf{0}_{1\times (N_{\mathrm{l}}-N_{\mathrm{c}})} \end{bmatrix} & \mathbf{0}_{2\times (N_{\mathrm{l}}-N_{\mathrm{c}})} \end{bmatrix}, \tag{3.15}$$

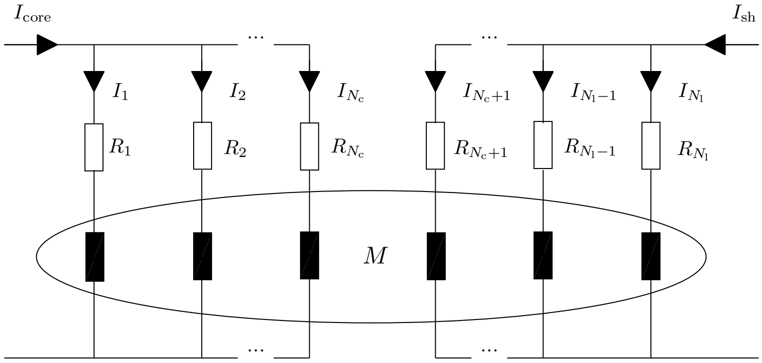

Figure 3.3: Equivalent circuit of superconducting cable with N_l layers. Resistances arise from self-field losses. Matrix M represents layers' magnetic connections.

where the inductance matrix M contains the self- and mutual inductances of the layers. The inductance matrix consists of circumferential and axial parts.

$$M = M_\mathrm{c} + M_\mathrm{a}, \tag{3.16}$$

where

$$M_\mathrm{c}(i,j) = \frac{\mu_0}{4\pi} \tan(\varphi_i) \tan(\varphi_j) \frac{[\min(r_i, r_j)]^2}{r_i r_j} \tag{3.17}$$

and

$$M_\mathrm{a}(i,j) = \frac{\mu_0}{2\pi} \ln\left(\frac{r_{N_\mathrm{l}}}{\max(r_i, r_j)}\right). \tag{3.18}$$

When $i = j$, the self-inductance of the layer is in question. Because the elements of $2\pi f M$ are much larger than R_i, it is acceptable to use phasors with a nonlinear problem. However, the nonlinear matrix equation must be solved iteratively, for example, as figure 3.2 shows [75, 78, 79].

3.2 Computed AC losses in example cables

The computational model was applied to YBCO cables to predict their electromagnetic behavior and AC losses in several YBCO cable designs, which for two reasons were mostly of the two-layer type. In multilayer cables, currents can divide unevenly between the layers, a division that was here avoided with a two-layer design consisting of one core layer and one shield layer. In addition, the external magnetic flux density in the multi-layer designs was increased compared to the two-layer cable of the same nominal current. The two-layer designs with nominal currents of 1, 2, 5, and 10 kA were labeled Cable 1, 2, 3, and 4, respectively. To show the differences between two-layer and multi-layer designs, Cable 5 was designed with two core and shield layers at a nominal current of 10 kA.

3.2.1 Design constraints

In practice, mechanical aspects restrict the lay angles, because the gaps between adjacent tapes must be wide enough to ensure the desired bending radius of the cable. In addition, the maximum lay length is limited, because increasing lay length undermines the mechanical strength of the cable [61]. The ratio of tape to gap areas within all layers was at most 19:1, and the tapes were evenly distributed. The minimum possible lay angle was expected to be 10°.

The tape was 4 mm and 0.1 mm in width and thickness, respectively. Its YBCO layer was 1.5 μm thick with a critical current of 90 A at 77 K and in self-field. The temperature and magnetic flux density dependence of I_c was modeled with the shape factor κ as

$$I_\mathrm{c}(B,T) = \kappa(B,T) \cdot 90 \text{ (A)}, \tag{3.19}$$

The shape factor was determined from the critical current of the YBCO tapes measured in the SUPERPOLI project [85] as

$$\kappa(B,T) = \frac{I_\mathrm{c}(B,T)}{I_\mathrm{c}(0\text{ T}, 77\text{ K})}, \tag{3.20}$$

where $I_\mathrm{c}(B,T)$ is the measured critical current of the tape in magnetic and thermal conditions corresponding to the superconducting cable. $I_\mathrm{c}(0\text{ T}, 77\text{ K})$ is the critical current of the tape in reference conditions. Critical currents were measured in parallel magnetic fields from 0 to 0.3 T and temperatures from 65 to 87.5 K. The shape factor was linearly interpolated from measured data, part of which is shown in figure 3.4. It has been suggested that to provide an appropriate safety margin, the operation temperature can be lowered from 77 to 75 K. Therefore, simulations were performed at 75 K. Other design parameters are listed in table 3.1. For low AC losses, the number of tapes was chosen so that the operation current was below 80% of the cable's critical current.

3.2.2 Computed results

The computational model was designed to give a pessimistic loss approximation because, in reality, the perpendicular magnetic flux density component is partly

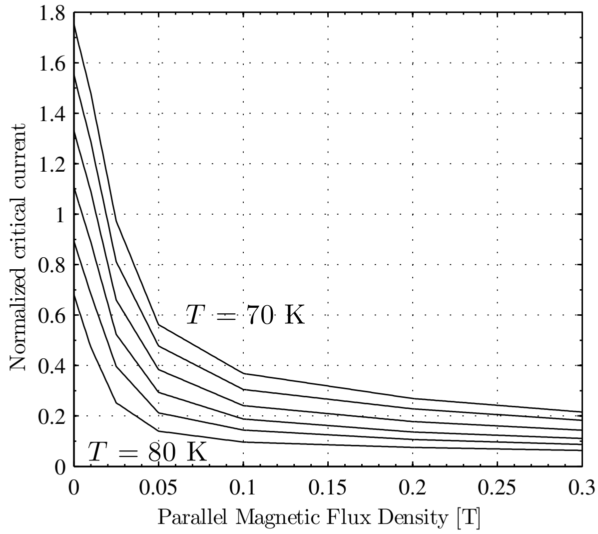

Figure 3.4: $\kappa(B,T)$ characteristics for computations. Available temperature data shown only partially; lines drawn at 2 K intervals.

Table 3.1: Parameters of cable designs for 1, 2, 5, and 10 kA-transport current. w_g is gap's width.

Model	Layer	N_t	r (mm)	l' (mm)	φ (deg)	w_g (mm)
Cable 1	Core	22	15	535	10.0	0.22
	Shield	29	20	713	10.0	0.27
Cable 2	Core	44	30	1069	10.0	0.22
	Shield	51	35	1247	10.0	0.25
Cable 3	Core	102	70	2494	10.0	0.25
	Shield	110	75	2673	10.0	0.22
Cable 4	Core	220	150	5345	10.0	0.22
	Shield	227	155	5523	10.0	0.23
Cable 5	Inner core	135	93	3296	10.0	0.24
	Outer core	134	93	2188	-15.0	0.21
	Inner shield	141	98	2473	13.9	0.22
	Outer shield	144	98	3492	-10.0	0.21

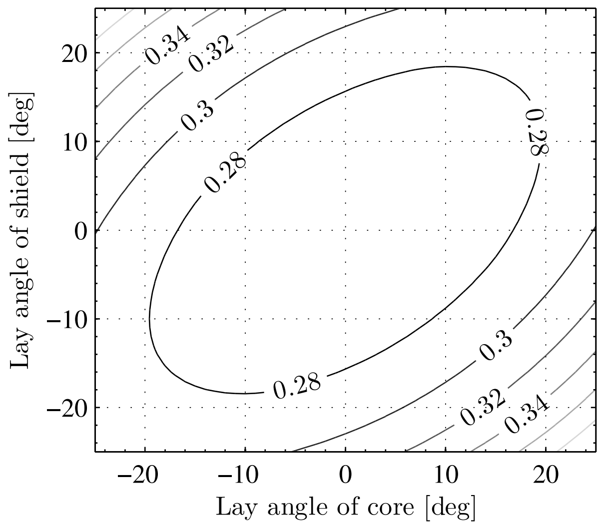

Figure 3.5: Total AC loss (W m^{-1}) of Cable 1 as a function of lay angles of core and shield. Self-field loss was computed using Norris strip approximation.

compensated for by the field of the neighboring tapes. Therefore, the strip approximation was used in simulations to achieve the upper loss limit. Ideally, one layer performs like a single current-carrying cylinder.

The total AC losses of Cable 1 at nominal current were computed with various lay angles with a constant number of tapes to find out how to choose lay angles for minimum AC losses. Total AC losses in Cable 1 as a function of lay angles are presented in figure 3.5. Total losses depend mostly on self-field losses, which increase with the tape length needed per one meter of cable. Thus the smaller the lay angle, the less tape is needed, and hence losses can be minimized by choosing small lay angles. The angles should have the same signs to partially compensate for the axial magnetic flux density in the cable.

All designs were simulated with their nominal currents. Table 3.2 shows self-field and magnetization losses for each layer in the cables and some additional simulation details. In two-layer simulations, the layers registered magnetic flux densities of about 9 mT and magnetization losses of about half a percent of the self-field losses. In comparison, the multilayer design produced a more compact geometry with the same transport current. The magnetic flux densities in the outer core and inner shield layer were about 9 mT, whereas the magnetic flux densities in the inner core and outer shield layer rose to about 23 mT. These magnetic fields caused I_c in the layers to drop by 39% and 36%, respectively, with the magnetization loss of the outer core and inner shield layer about 2% of the self-field loss. The cables' total AC losses at nominal currents are summarized in table 3.3 together with the length of the HTS tape

Table 3.2: Details of AC loss computations for designs.

Model	Layer	I (A)	I_c (A)	i_n	B_c (mT)	B_a (mT)	P_{self} (W m^{-1})	P_{mag} (mW m^{-1})
Cable 1	Core	1000	90	0.71	9.4	0.8	0.20	0.9
	Shield	-1000	95	0.51	7.1	1.2	0.07	0.5
Cable 2	Core	2000	90	0.71	9.4	1.2	0.40	1.9
	Shield	-2000	93	0.60	8.1	1.4	0.24	1.3
Cable 3	Core	5000	89	0.78	10.1	1.5	1.34	5.5
	Shield	-5000	90	0.71	9.4	1.7	1.01	4.7
Cable 4	Core	10000	90	0.71	9.4	1.6	2.02	9.4
	Shield	-10000	91	0.69	9.1	1.6	1.80	8.8
Cable 5	Inner core	5804	91	0.67	8.9	2.0	0.93	4.9
	Outer core	4196	55	0.81	24.0	1.8	0.84	14.8
	Inner sh.	-4253	58	0.74	22.8	1.4	0.63	14.5
	Outer sh.	-5747	92	0.61	8.3	1.5	0.69	4.1

Table 3.3: Performances of cable designs at their nominal current. l_t is the total length of tapes used to produce one meter of cable and P/l_t total AC loss per one meter of YBCO tape.

Model	I (kA)	P (W m^{-1})	l_t	P/l_t (mW m^{-1})
Cable 1	1	0.27	52	5.2
Cable 2	2	0.65	96	6.7
Cable 3	5	2.36	215	11.0
Cable 4	10	3.84	454	8.5
Cable 5	10	3.13	567	5.5

needed per one meter of cable and total AC losses per one meter of tape.

Finally, figure 3.6 shows the AC losses of the cable designs as a function of transport current. In the inner core and outer shield layer of Cable 5, critical currents were almost equal to the I_c in the core and shield layers of Cable 4. However, in the outer core and inner shield layer the increased magnetic field dropped I_c rapidly as the operating current increased. Therefore, the total AC loss in Cable 5 rose faster than that in Cable 4. At 10 kA, the multi-layer design registered about a 20% lower total AC loss than the two-layer design.

3.3 Comparison with a one-layer test cable

To fully exploit the performance of YBCO conductors in cables, it is important to understand current sharing between the layers and also between individual tapes in one layer. Designers should also be able to calculate AC losses fast and accurately. To verify the performance of the developed model, computed results are here compared with measurements of a 0.5-m, one-layer cable constructed in the Super3C project. The 0.5-m cable was also used to scrutinize current sharing between individual tapes. Measurements showed that variations in contact resistances can be crucial in short cable prototypes. However,

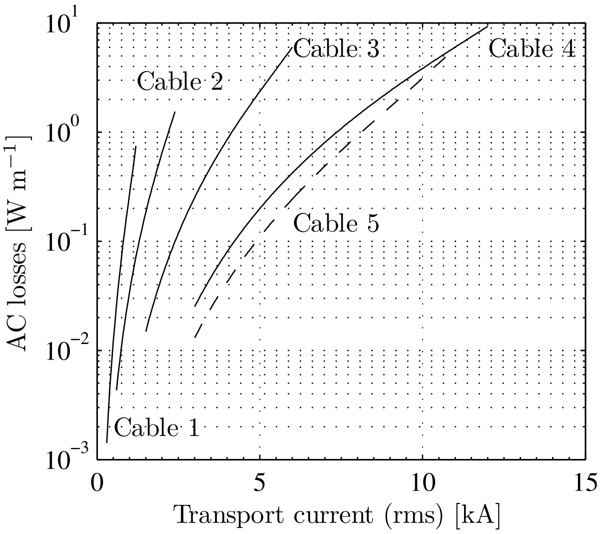

Figure 3.6: Total AC losses of cables; multilayer cable losses shown with a dashed line.

further computational study suggested that contacts would not pose problems in the final 30-m, 1 kA, 10 kV YBCO cable to be constructed in the Super3C-project.

3.3.1 Model for layerwise current distribution

The model described in section 3.1.1 had to be tuned to solve current sharing between the tapes in one layer. The main difference here was the generation of an inductance matrix. In addition, due to the thin superconducting layer, magnetization losses were small and hence ignored.

Because the tapes in a layer are connected in parallel, the matrix equation is as follows:

$$\left(R(\mathbf{x}) + \begin{bmatrix} \mathrm{j}2\pi f M & -\mathbf{1}_{N_\mathrm{t}\times 1} \\ \mathbf{1}_{1\times N_\mathrm{t}} & 0 \end{bmatrix} \right) \mathbf{x} = \begin{bmatrix} \mathbf{0}_{N_\mathrm{t}\times 1} \\ \overline{I} \end{bmatrix}, \tag{3.21}$$

where the elements of the diagonal matrix R are the total resistances of the tapes per cable length l. The total resistances of individual tapes consist of the contacts resistance R_c and that caused by the AC losses of the superconductor R_ac. Accordingly, the resistance of the superconducting tape per cable length was

$$R_{ii} = R_\mathrm{c} + R_\mathrm{ac} = \frac{R_{\mathrm{c}1,i} + R_{\mathrm{c}2,i}}{l} + \frac{P_{\mathrm{strip},i}}{I_{\mathrm{t},i}^2 \cos(\varphi)}, \tag{3.22}$$

where $R_{c1,i}$ and $R_{c2,i}$ are contact resistances at both ends of the tape, φ is the lay angle of the layer, $I_{t,i}$ the rms value of the ith tape current.

The first elements of $\mathbf{x}$ are the phasor currents of the individual tapes. The last element is the phasor voltage over the tapes. $f = 50$ Hz is the frequency of the driving current. In addition, the magnetic coupling between the tapes is described by the inductance matrix

$$M = \begin{bmatrix} M_{11} & M_{12} & M_{13} & \cdots & M_{1N_t} \\ M_{1N_t} & M_{11} & M_{12} & \cdots & M_{1(N_t-1)} \\ M_{1(N_t-1)} & M_{1N_t} & M_{11} & \cdots & M_{1(N_t-2)} \\ \vdots & \vdots & \vdots & \ddots & \\ M_{12} & M_{13} & M_{14} & & M_{11} \end{bmatrix}. \tag{3.23}$$

The inductances between the tapes were integrated numerically as

$$M_{1i} = \frac{1}{S_{\mathrm{tape}}} \int_{\Omega_i} A_1 \mathrm{d}s - \frac{1}{S_{\mathrm{cyl}}} \int_{\Omega_{\mathrm{cyl}}} A_1 \mathrm{d}s, \tag{3.24}$$

where Ω_i is the cross-section of the ith tape and S_{tape} the cross-sectional area. Correspondingly. Ω_{cyl} is the cross-section of the return conductor and S_{cyl} the cross sectional area. A_1 is the magnetic vector potential caused by the unit current in tape 1 and in the return conductor on condition that the current density is constant in both the tape and the return conductor [92]. Total AC losses for one layer were obtained as the sum of AC losses in individual tapes computed with the solved tape currents.

3.3.2 Experimental

AC losses in the 0.5-m cable were determined by electrical measurement, in which the testing current was delivered across a transformer; that is, it was the secondary current of a power transformer, shown in figure 3.7 [101]. Voltage U_{aux} was detected with the help of an auxiliary loop embracing the core of the power transformer. The component of this voltage in phase with the testing current I_{cable} was equal to the sum of the in-phase voltages of all the secondary circuit current components.

For simplicity, figure 3.7 shows only the cable core and the resistive part of the secondary loop. A dissipative voltage on the superconducting cable was then detected as a difference between the in-phase components of two measured signals. With this scheme, signal wires became unnecessary in the cable's cryogenic envelope. The test cable consisted of 14 tapes, wound on a ∅ 21-mm cylinder at a 10°-lay angle. Its 3.8-mm wide and 2.5-µm thick YBCO

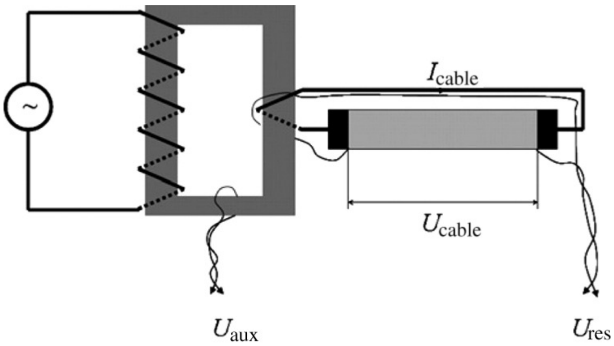

Figure 3.7: AC loss measurement set-up.

layer carried a critical current of 75 A in a self-field. The current returned via a 40-mm copper cylinder, coaxial with the tape layer.

The metallic, less than 1 μm thick layer on top of the YBCO was used to examine the distribution of contact resistances on the completed cable as follows. Each tape was provided with an auxiliary current lead, which allowed feeding a test current across the contact between the tape and the current termination, as shown in figure 3.8. Because of the tapes' low thermal conductivity, only one end of the test cable could be cooled with liquid nitrogen, allowing the contact resistances at that end to be determined. The test current I_{test} fed to the auxiliary current lead could use no other path but to return to the current termination, because the tapes' upper part was at ambient temperature and thus highly resistive. The contact resistance for each tape was determined according to Ohm's law from a fixed $I_{test} = 10$ A and a test voltage U_{test}.

3.3.3 Current sharing and contact resistances

The quality of the connections between the tapes and the copper block serving as the current termination varied considerably. Due to the wide spread of contact resistances listed in table 3.4, the critical current of the test cable was lower than that of a single tape multiplied by the number of tapes. To observe the distribution of the cable current among individual tapes in the DC regime, contact resistances were used as shunts to determine all tape currents in such a test. The results are shown in figure 3.9. Measurements showed that currents in individual tapes varied widely.

Figure 3.10 shows the simulated effect of contact resistances on AC current distribution for the 0.5-m and 30-m cable. Because contact resistance depends on frequency due to the skin effect [53], measured contact resistances were

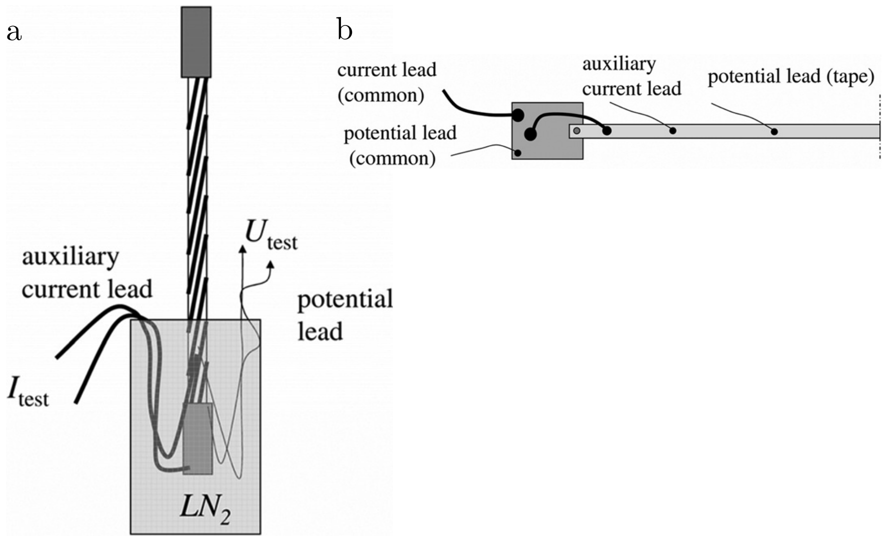

Figure 3.8: (a) Experimental set-up to determine contact resistances. Only the tapes' lower part, immersed in liquid nitrogen, is superconducting. (b) Set of electrical contacts provided for each tape to determine contact resistance. Only one tape shown for simplicity with lay angle omitted in drawing.

multiplied by a constant c_{ac} in simulation. The dispersion of tape currents becomes insignificant when the cable reaches the project's goal of 30 m with a large span of c_{ac}. Figure 3.11 shows tape currents with a pessimistic $c_{ac} = 5$ and a 500-A transport current as a function of cable length. They converge because the inductances become dominant when the cable increases in length.

AC loss measurements were compared to computed results. Figure 3.12 shows the cable's AC losses computed with three different models. Model I followed Kim's approximation:

$$I_c(B) = \frac{75}{1 + \left(\frac{B}{56\ \mathrm{mT}}\right)^{0.6}}\ \mathrm{(A)}, \tag{3.25}$$

where B is the magnetic flux density parallel to the film surface. The approximation yielded markedly higher losses than the measured values, which means that in reality the critical current does not fall at fields under 20 mT as rapidly as in the model.

When AC losses were computed with a constant $I_c = 75$ A (Model II), very accurate AC loss figures were obtained. This may indicate that the tape's critical current is more than was assumed in cable use. Computed losses were slightly optimistic only at transport currents of beyond 500 A. In Model III, individual tape currents were determined from equation 3.21. The current deviation between the tapes slightly increased AC losses. The error is systematic

Table 3.4: Contact resistances at ends of YBCO tapes.

Tape	1	2	3	4	5	6	7	8	9	10	11	12	13	14
R_{c1} (μΩ)	87	54	53	56	54	50	52	48	45	75	45	38	53	46
R_{c2} (μΩ)	46	42	52	42	43	43	45	48	47	53	43	28	60	30

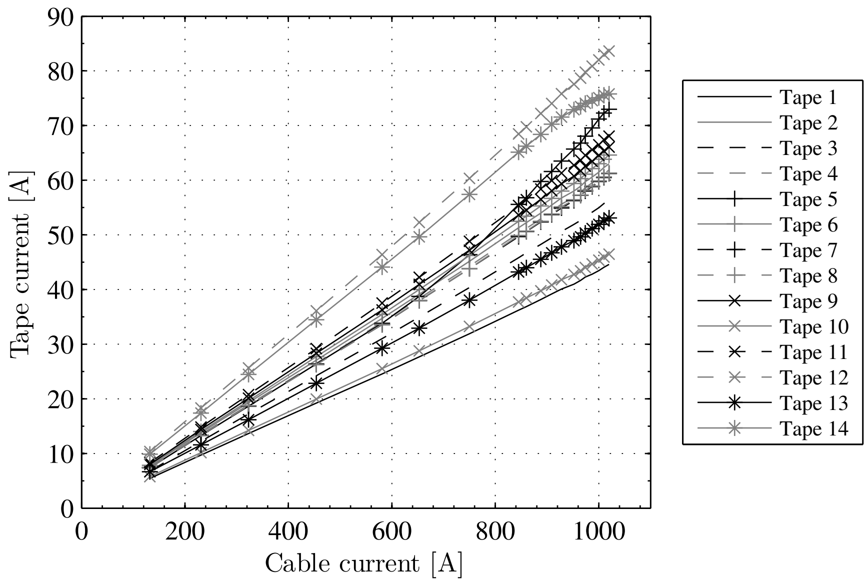

Figure 3.9: Distribution of total cable current among individual tapes in DC test. Contact resistances were used to determine individual tape currents.

between 200–600 A. In addition, convergence of the tape currents lowered AC losses from 92 mW m^{-1} in the 0.5-m cable to 68 mW m^{-1} in the 30-m cable.

3.4 Concluding remarks

This chapter dealt with the computational model of AC losses and current sharing in YBCO cables. The model's theoretical basis, founded on circuit analysis, was improved and applied to YBCO cables. The model takes into account the magnetic field inside the cables, which reduces the critical current of YBCO tapes. Furthermore, the model was applied to designing and simulating two- and four-layer YBCO cables with nominal currents of 1–10 kA (rms).

With two-layer cables, minimal AC losses were achieved when the lay angles had the same signs and were as small as possible. In each case, magnetization losses in the YBCO tapes were at most 2% of the self-field losses with all simulated cable designs. Two-layer and four-layer cables with 10 kA nominal currents had total AC losses of 3.84 W m^{-1}and 3.13 W m^{-1}, respectively. The

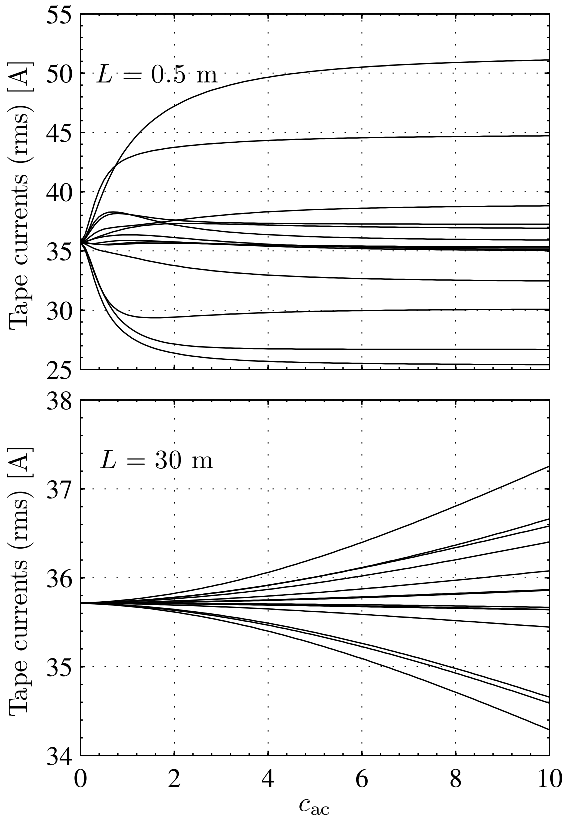

Figure 3.10: Computed currents of tapes as function of c_{ac} with transport current of 500 A (rms).

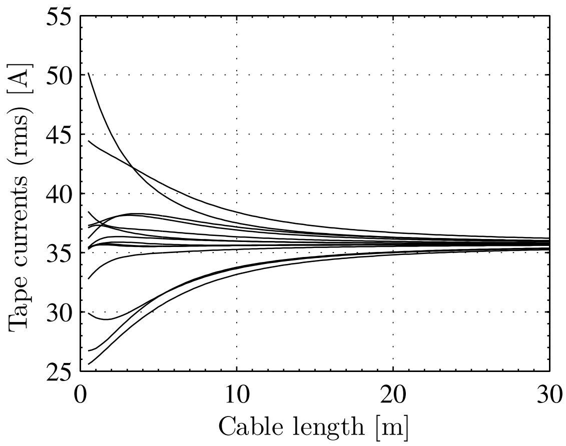

Figure 3.11: Computed currents of tapes as a function of cable length with a transport current of 500 A (rms) and $c_{ac} = 5$.

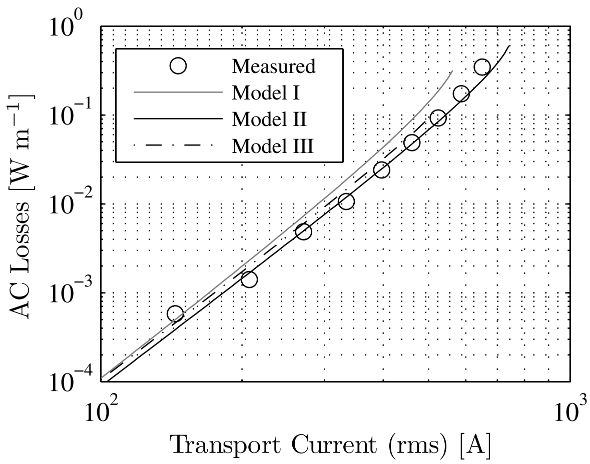

Figure 3.12: AC losses in a 0.5-m YBCO cable with Models I, II, III. Computations were run up to the critical current of the weakest tape.

multi-layer design was more compact than the two-layer design, but the greater magnetic flux density in the cable had a greater effect on the critical current of the YBCO tapes.

To verify the AC loss model, results were compared to measurements of a 0.5-m, one-layer test cable, constructed to test AC losses and current sharing in a real YBCO cable. AC losses measured for this cable agreed well with results computed with circuit analysis models. Measurements also showed that in short cables variations in contact resistances may cause uneven current sharing between the tapes. Further computational analysis suggested that in the final 30-m YBCO cable to be constructed in the Super3C project, tape currents will be equal to an accuracy of 2%.

Though the circuit analysis model is rough, it seems to predict AC losses quite accurately. However, results suggested higher that the $I_c(\mathbf{B})$-dependence used here may be conservative. The next chapter elaborates on this issue and presents a new technique to predict the critical current of tapes in a cable application.

Chapter 4

Critical current analysis

This chapter explains how the critical current of a cable can be computationally determined from critical current data measured from individual tapes. First, to show the role of the tape's self-field, a method to solve the critical current of a tape from its intrinsic material parameters is explained. Second, an optimization method is proposed to determine material parameters from measured critical current data. Finally, a technique is introduced to compute the critical current of a cable from its material parameters.

The method developed here to solve the critical current of a tape from its intrinsic material parameters can help tape manufacturers as well. The engineering current density in YBCO-coated conductor applications can be improved in two ways. Either the critical current density should be improved or the superconducting films made thicker. Unfortunately, it has often been observed that the average critical current density drops when the film thickness increases. Suggested reasons for this behavior include, for example, two-dimensional pinning properties, microcracks, and imperfect crystallographic alignment.

However, it has often been forgotten that the self-field effect inevitably reduces the critical current density when the thickness of YBCO films increases and, along with it, the total current. Here, the impact of the self-field on the average critical current density was studied computationally as a function of film thickness. The situation was also scrutinized at different external magnetic fields to find ways to distinguish self-field effects from problems related to the manufacturing process. That is why critical current measurements are proposed to be done at the external field perpendicular to the film surface.

The method to compute the tape's critical current can also be used as optimization to determine the magnetic field dependence of the intrinsic critical current density, $J_c(\mathbf{B})$. First, the critical current is measured in various external magnetic fields. Then the $J_c(\mathbf{B})$-dependence that fits optimally the measurements is searched for. Because the self-field of the sample is taken into account, also measurements done at low external magnetic fields below 0.1 T can be exploited. Here the $J_c(\mathbf{B})$-dependence of the YBCO material was described with the Kim model, which is modified to take into account also anisotropy. Thus, we have four parameters to search: the zero field critical current density J_{c0}, the reference field B_0, the Kim model exponent α, and the anisotropy scaling factor γ. Searching for all these parameters was computationally challenging, yet computation times remained within reasonable limits. As examples, the $J_c(\mathbf{B})$-dependences of two YBCO samples by different manufacturers were solved. For both samples, all parameters except B_0 were close to each other. For example, for both samples, J_{c0} was about $0.9 \cdot 10^{10}$ A m^{-2}.

Finally, the method to compute the tape's critical current was extended to apply to cables as well. In cables, for mechanical reasons, gaps must be left between adjacent tapes. The effect of these gaps on the tapes' critical current was determined based on the cable geometry and the intrinsic $J_c(\mathbf{B})$-dependence. In the studied 1-kA cable, the gap effect caused the critical current of the individual tapes to actually rise from 86.5 to 88.8 A, when they were moved from self-field to cable field. The gap effect was also studied as a function of superconducting layer width, cable radius, and tape number. It was shown that the cable's critical current can be given as a function of tape number and the layer fill factor defined in this paper. In addition, the results suggested that the gap effect will become increasingly important in the future when J_{c0} is expected to rise.

4.1 Tape's critical current

The engineering critical current density, J_e, is one of the main parameters that determines the viability of the application [123]. YBCO films produce extremely high critical current densities, J_c, up to several MA cm^{-2} at 77 K, but the engineering current density is drastically lowered, because the superconducting layer is very thin compared to the substrate on which it is grown [17].

Obviously, J_e should be improved if superconducting films are made thicker [77]. So far, some encouraging examples have appeared in which the average critical current density of the YBCO layer, J_{ca}, at self-field seems quite independent of the thickness of the YBCO layer, d. Such situations have been reported in tapes manufactured by the TFA-MOD method [44, 109] or with yttrium-rich compositions [27]. However, commonly J_{ca} decreases if the thickness d is increased. Several possible reasons have been suggested for this behavior. According to collective pinning theory, J_{ca} should be proportional to $d^{-1/2}$ when d is smaller than the pinning correlation length [57]. This explanation has been criticized because at sufficiently high magnetic fields, J_{ca} can be higher in a thicker superconducting tape [71], and the $J_{ca}(d)$-dependence does not vanish at low temperatures, as predicted [70].

More probable reasons point to the deteriorating structure of YBCO material. When d increases, regions may appear where the crystallographic c-axis is no longer normal to the substrate plane [70, 73]. If d exceeds some tenths of micrometers, microcracking usually occurs owing to the difference between the thermal expansion coefficients in the substrate and the YBCO film [45]. However, recently, a film thickness of up to the micrometer range has been achieved with sapphire substrates without microcracking [21], but even then J_c plummeted with increasing film thickness [22]. The film's porosity and roughness increased accordingly, changing the defect structures responsible for flux pinning.

$J_{ca}(d)$-variations cannot be explained solely on the basis of material quality. In analysis, it should be remembered that the self-field effect inevitably reduces the critical current density when the thickness of YBCO films increases and the total current rises. The self-field effect has been studied both computationally and experimentally in LTS films [31] and BSCCO tapes [59, 98, 103], and recently a one-dimensional computational model was applied to YBCO films [13]. Because of mesh generation problems encountered with the finite element method due to the high aspect ratio of YBCO tapes [104], a self-made algorithm, a simple and fast approach based on the integral element method, was chosen here.

4.1.1 Computational model

In computations, homogeneous YBCO material and the DC operating current were assumed. Homogeneous means that the Kim model parameters over the cross-section are constant. Thus variations in the current density distribution were exclusively due to spatial variations in the self-field. A Cartesian coordinate system was used, in which the x-axis was parallel with the broad face of the tape, the y-axis parallel with the narrow face, and the current flowed in the positive z-direction. The magnetic flux density created by the transport current flowing in the tape was denoted by $\mathbf{B}_{self}$. Furthermore, the tape can be exposed to an external magnetic flux density $\mathbf{B}_{ext}$ shown in figure 4.1.

The algorithm sought to determine the current density distribution that fulfills the condition $J = J_c\left(\mathbf{B}_{ext} + \mathbf{B}_{self}(J)\right)$ inside the film. Here, the local $J_c(\mathbf{B})$-dependence was described with equation 2.6, in which the intrinsic critical current density J_{c0} was 3 MA cm^{-2} [13], the reference field B_0 was 20 mT [13], the Kim model exponent α was 0.65 [30], and the anisotropic scaling factor γ was 5 [18]. These parameters serve as a typical example of the $J_c(\mathbf{B})$-dependence of YBCO for any search of general trends in the self-field effect.

The film's cross-section was divided into N_x times N_y rectangular elements in order to calculate the magnetic flux density, $\mathbf{B}_{\text{self}}(\mathbf{r})$, created by $J(\mathbf{r}')$, where $\mathbf{r} = [x\ y]^T$ and $\mathbf{r}' = [x'\ y']^T$. In computations, the mesh shown in figure 4.1 with $N_x = 16$ and $N_y = 12$ was used as a default. When the current densities inside such elements are assumed constant, the magnetic flux density can be calculated from the two-dimensional Biot-Savart law

$$\mathbf{B}_{\text{self}}(\mathbf{r}) = \frac{\mu_0}{2\pi}\begin{bmatrix} 0 & -1 \\ 1 & 0 \end{bmatrix}\int_{S_{\text{YBCO}}} \frac{J(\mathbf{r}')(\mathbf{r}-\mathbf{r}')}{(\mathbf{r}-\mathbf{r}')^2}\mathrm{d}s, \tag{4.1}$$

where μ_0 is the vacuum permeability, and S_{YBCO} is the cross-section of YBCO.

The block diagram in figure 4.2 shows the principle of the algorithm starting from a constant current density. Magnetic fields were calculated in the element centers, and a new current density distribution was achieved as $J_{\text{new}} = J_c(\mathbf{B}_{\text{ext}} + \mathbf{B}_{\text{self}}(J_{\text{old}}))$, where J_{old} is the previous current distribution. After that, the critical current was computed as an integral of the new current density over the sample's cross-section. The critical current was compared with its previous iteration value, and if the relative change remained below a given tolerance, a final current density distribution was obtained. Otherwise, the procedure was repeated.

Simulations were done with the self-made algorithm implemented for MATLAB. About ten iterations were required to find the final critical current with a relative tolerance of 10^{-6}. Acceptable solutions could also be achieved with a very coarse mesh. For example, if the self-field critical current in a 4 mm × 1.5 μm tape was computed with $N_x = 4$ and $N_y = 3$, the result deviated less than 2.95%, compared to a mesh of $N_x = 64$ and $N_y = 48$. For the default mesh, the deviation was less than 0.57%, and it took about 0.3 s to compute one critical current with the AMD Athlon 64 3400+.

4.1.2 YBCO layer thickness and tape's critical current

The self-field always depends on the sample geometry and dimensions. Thus both the sample width and film thickness should affect J_{ca}. However, J_{ca} was practically constant at a given film thickness, if the sample width exceeded one tenth of a millimeter, as shown in figure 4.3a. Therefore, in practice, the sample width can be ignored, and attention can be paid solely to the film thickness.

To explain the above result, the magnetic field inside the film was studied. Figure 4.3b shows that after the sample width reached one millimeter, the

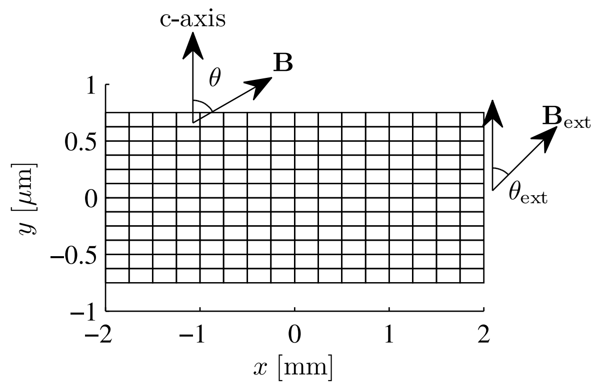

Figure 4.1: Tape's cross-section and default mesh with $N_{\mathrm{x}} = 16$ and $N_{\mathrm{y}} = 12$.

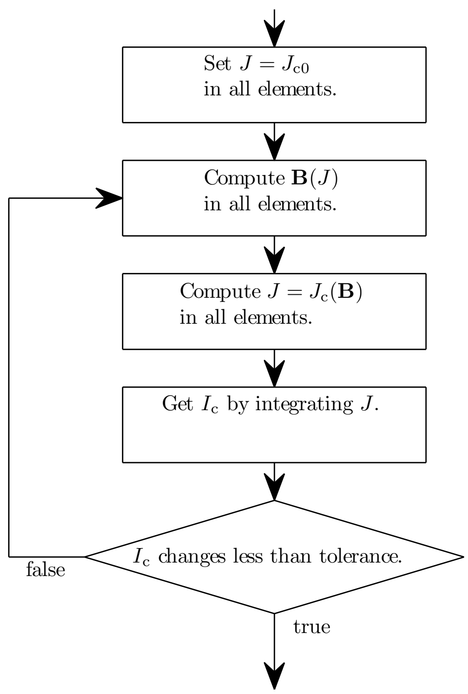

Figure 4.2: Block diagram of critical current computation.

average of B_y was always practically constant. The average of B_x could increase slightly until the sample width reached one millimeter, but in an anisotropic superconductor, the critical current density is mainly determined by B_y [98].

Usually, the short sample critical current is measured as a function of the magnetic flux density magnitude at a constant field orientation, defined by the angle θ_{ext} between the field and the normal of the film surface. Figure 4.4 presents J_{ca} as a function of YBCO film thickness in both parallel and perpendicular external magnetic fields. In the self-field, $J_{ca}(d)$ closely resembled exponential decay, and in a 3-μm thick film, J_{ca} was reduced by about 35%, compared to the real zero field critical current density J_{c0}. Exponential decay was also fitted to measurements in [22, 28]. For example, the decay measured in [28] was probably caused mainly by the self-field effect, because no structural problems were detected in the samples. Here the function

$$J_{ca}(d) \approx J_{c0} \cdot \left[0.41984 \cdot \left(-\frac{d}{1.7929 \times 10^{-6}}\right) + 0.57563\right] \tag{4.2}$$

fits the computed self-field J_{ca} values in figure 4.4 with a maximum relative error of 0.42%. The parameter values in equation 4.2 were given at five-digit accuracy, because the fitting was sensitive to them. However, even a much better fit was achieved as

$$J_{ca}(d) \approx J_{c0} \cdot \left(1 + \frac{d}{1.2826 \times 10^{-6}}\right)^{-0.35509}, \tag{4.3}$$

which produced only a 0.016% error.

In external magnetic fields, the situation changes dramatically. Even in parallel fields, the shape of $J_{ca}(d)$ is no longer exponential. In perpendicular fields, $J_{ca}(d)$ was quite constant if the thickness was below 0.60, 1.42, and 2.46 μm at a B_y of 10, 20, and 30 mT, respectively. In other words, thickness has no significant effect on J_{ca}, if the external field is higher than the maximum value of the self-field y-component. Therefore, YBCO thin film samples should be measured at a sufficiently high perpendicular external magnetic field, where the self-field effect is canceled out, and where J_{ca} will directly describe the quality of the material. Thus, for example, the measured critical currents in [71] suggest that the quality of the studied material actually improved with increasing d.

4.1.3 Orientation of external field

To further visualize the self-field effect, figure 4.5 shows the average critical current density as a function of external magnetic flux density at different field

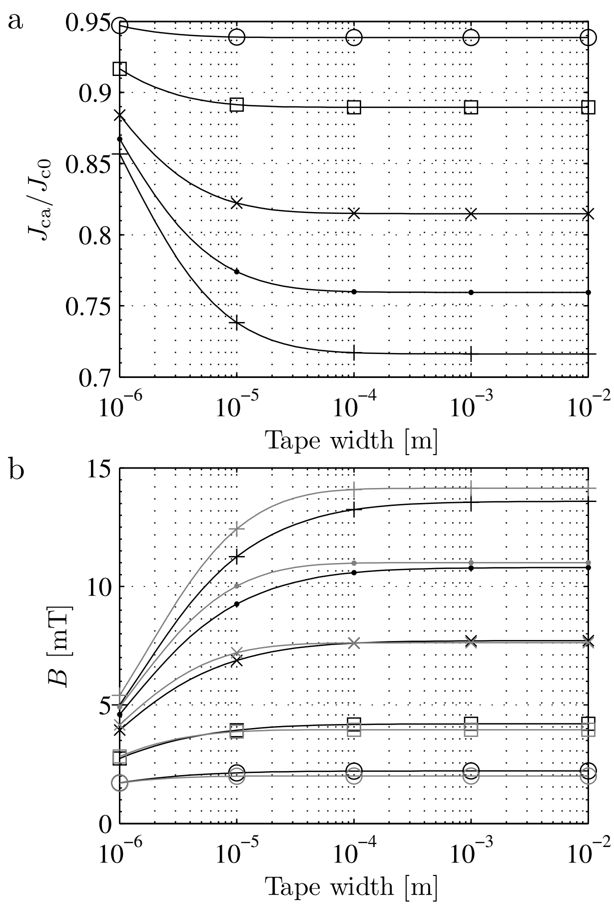

Figure 4.3: (a) Normalized average critical current density and (b) average B_x (black) and B_y (gray) inside the YBCO as functions of YBCO tape width with different film thicknesses: (○) 0.25 μm, (□) 0.5 μm, (×) 1.0 μm, (·) 1.5 μm, and (+) 3.0 μm.

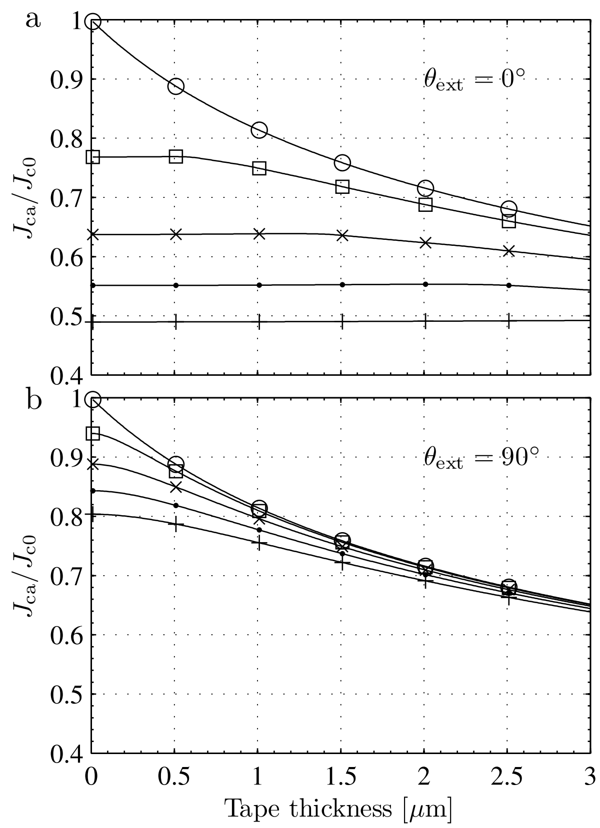

Figure 4.4: Computed normalized average critical current density as a function of YBCO film thickness at different external magnetic fields oriented (a) perpendicular and (b) parallel to film surface: (○) 0 mT, (□) 10 mT, (×) 20 mT, (·) 30 mT, and (+) 40 mT.

orientations in a 1.5-μm thick YBCO film. At low parallel fields, J_{ca} remains quite constant due to the self-field effect.

Figure 4.6 illustrates the current density distributions in the YBCO film at different external fields. Here the mesh with $N_x = 64$ and $N_y = 48$ was used to achieve an appropriate resolution for figures about the current density distribution. In the self-field, B naturally equaled zero in the film centre; therefore, the current density was highest there. When the film was exposed to an external magnetic field, the self-field and the external field in some parts compensated for each other. The region of the highest J shifted to the point where compensation was most effective. Thus at low external fields, just the shape of the J-distribution was reformed, but the average critical current density changed little. At perpendicular fields, also the J_{ca} dropped, because the critical current density decreased drastically even at low B values. Similar behavior often occurs in high-quality BSCCO tapes as well [59, 62]. The self-field effect was noticeable in J_{ca} as long as the current density distribution remained inhomogeneous. When the external magnetic field rose, the current distribution was homogenized, and the self-field effect could be ignored.

The $J_c(\mathbf{B})$-dependence can vary significantly between tapes and can be complicated in anisotropic HTS materials. Thus the $J_c(\mathbf{B})$-dependence model used here does not necessarily describe it correctly [60]. Therefore, the sensitivity of the results was studied with respect to parameters J_{c0}, B_0, α, and γ. The basic definition states that the sensitivity $S_n(p, q)$ of a quantity q with respect to parameter p is computed as

$$S_n(p, q) = \frac{p}{q}\frac{\mathrm{d}q}{\mathrm{d}p}. \tag{4.4}$$

Here, the derivative was approximated numerically as

$$\frac{\mathrm{d}q}{\mathrm{d}p} \approx \frac{q(1.1p) - q(0.9p)}{0.2p}. \tag{4.5}$$

Equation 4.4 gives a rough estimate of how much a change in a parameter value affects J_{ca}. Table 4.1 shows the sensitivity of J_{ca}/J_{c0}. The most sensitive parameter was α, whereas variations in the anisotropy factor γ had almost no effect on the results. It is expected that α and γ do not vary significantly between samples, but that J_{c0} and B_0 can depend strongly on sample quality. Therefore, when this analysis is applied to real samples, attention should be paid to determining their values. Yet small variations in the chosen parameters do not affect the general trend in results.

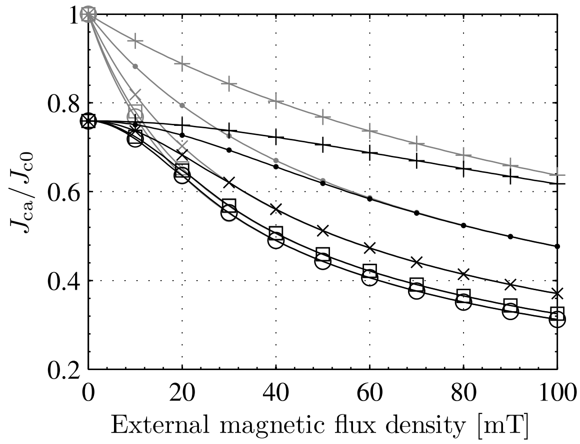

Figure 4.5: Normalized average critical current density as a function of external magnetic flux density at different field orientations in YBCO film with a thickness of 1.5 μm: (○) $\theta = 0°$, (□) 22.5°, (×) 45°, (·) 67.5°, and (+) 90°. For comparison, normalized critical current density as given by equation 2.6 is shown in gray.

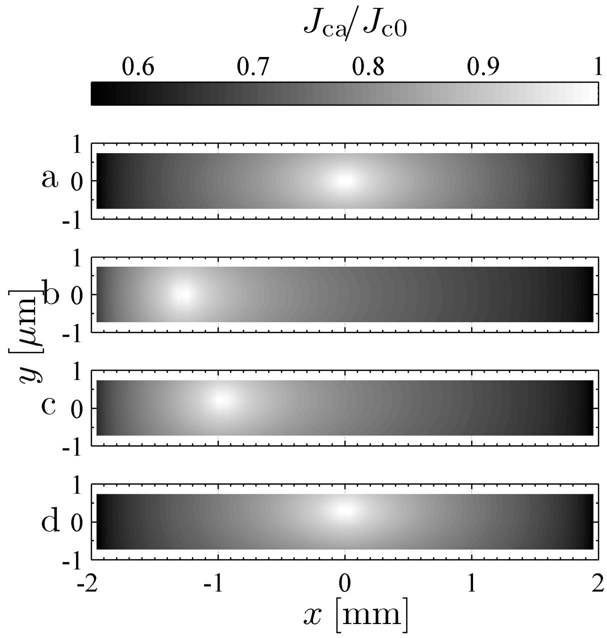

Figure 4.6: Current density in YBCO film with a thickness of 1.5 μm at different external magnetic fields: (a) self-field, (b) $\theta = 0°$, $B = 10$ mT, (c) $\theta = 45°$, $B = 10$ mT (d) $\theta = 90°$, $B = 10$ mT.

Table 4.1: Sensitivity of normalized average critical current density with respect to intrinsic material parameters; sensitivity studied with thicknesses $d_1 = 0.25$ µm, $d_2 = 1.5$ µm, $d_3 = 3$ µm and external magnetic flux densities $B_1 = 0$ mT, $B_2 = 20$ mT.

	d_1, B_1	d_2, B_1	d_3, B_1	d_1, B_2	d_2, B_2	d_3, B_2
J_{c0}	0.06	0.19	0.25	-0.00	0.05	0.15
α	0.06	0.25	0.36	0.45	0.45	0.48
B_0	-0.06	-0.19	-0.25	-0.33	-0.31	-0.32
γ	-0.01	-0.01	-0.01	-0.00	-0.01	-0.01

4.2 Search for intrinsic material properties

For HTS application designers, information about a tape's self-field performance is not enough when they are to estimate the electrical performance and possible AC losses of the whole application. For this purpose, it is essential to have accurate information about the magnetic field dependence [33, 51] of the intrinsic critical current density, $J_c(\mathbf{B})$. Such information would also directly characterize the quality of YBCO regardless of tape structure and make it possible to compare different tapes.

Unfortunately, the $J_c(\mathbf{B})$-dependence of YBCO is hard to measure directly due to the sample self-field [68]. Usually, the problem is avoided by fitting the Kim model to high-field measurements and by extrapolating J_c for low-field values [62]. However, extrapolation is always prone to errors; therefore, more accurate information would be gained of the $J_c(\mathbf{B})$-dependence, if measurements could be performed directly of the fields studied. For example, the fields in the superconducting power cable are of the order of the self-field of the tapes.

An alternative way is presented here to determine the $J_c(\mathbf{B})$-dependence accurately by an optimization method. The method takes into account the current distribution in the YBCO layer and the self-field. Hence, the $J_c(\mathbf{B})$-dependence can be determined from the critical current values measured for low external magnetic fields. These measurements are inexpensive, because they can be done with conventional magnets.

4.2.1 Optimization method

When the critical current of a superconducting tape is computed from a $J_c(\mathbf{B})$-model, simulated critical currents I_{cs} should agree with measured critical currents I_{cm}, if the $J_c(\mathbf{B})$-model is correct. Thus determining the $J_c(\mathbf{B})$-model can be formulated as a minimization problem

$$\min_{\mathbf{x}} f(\mathbf{x}) = \min_{\mathbf{x}} \sum_i [I_{\text{cm}}(\mathbf{B}_i) - I_{\text{cs}}(\mathbf{B}_i, \mathbf{x})]^2, \tag{4.6}$$

where $\mathbf{x}$ is a vector containing the parameters of the chosen $J_{\text{c}}(\mathbf{B})$-model and I_{cm} the measured critical currents at external magnetic flux densities $\mathbf{B}_i$. Here the $J_{\text{c}}(\mathbf{B})$-dependence was also described with the Kim model extended to take into account material anisotropy according to equation 2.6. Simulated critical currents I_{cs} were computed with the integral element method, taking into account the sample's self-field according to section 4.1.1.

The total magnetic field of a fully penetrated tape consists of an external field and a self-field, as shown in figure 4.7. Note that in high-field measurements the self-field can be ignored. In typical voltage-current measurements, the external field is very homogeneous and has thus a spatially constant norm B_{ext} and an angle θ_{ext}.

First, artificial critical current data was generated to verify the reliability of the minimization process. A homogeneous YBCO tape with dimensions of 4 mm $\times$ 1.5 µm was studied. Again, the YBCO material was characterized with the following parameters: $J_{\text{c0}} = 3 \cdot 10^{10}$ A m^{-2} [13], $B_0 = 20$ mT [13], $\alpha = 0.65$ [30], and $\gamma = 5$ [18]. The critical current was computed at the external magnetic fields shown in figure 4.8. In computations, the tape was divided into 16×8 elements to take the self-field into account. This critical current data was used as input for the minimization algorithm, and the initial values were chosen as $J_{\text{c0}} = 1 \cdot 10^{10}$ A m^{-2}, $B_0 = 1$ T, $\alpha = 1$, and $\gamma = 1$.

Optimization turned out to be very difficult. However, the Nelder-Mead simplex algorithm [54] worked in a robust way, though the convergence was slow, as shown in figure 4.9. However, the slow optimization convergence was accepted, because the required critical current computations were very fast. Thus the total computation time for the data shown in figure 4.9 was about one minute. The neighborhood of the optimum point was found after 480 steps, after which convergence was expedited. The optimum was found when the 10^{-6} relative tolerance was achieved.

A measurement error can lead to a significant error in the optimized $J_{\text{c}}(\mathbf{B})$-dependence. Therefore, the effect of a measurement error on the solution of equation 4.6 was studied statistically. First, the input data for optimization was computed as in figure 4.8. Then the values were perturbed with a disturbance which had a uniform distribution within the interval $[-\delta, \delta]$. Equation 4.6 was solved 100 times, and the relative error in the solved $J_{\text{c}}(\mathbf{B})$-model parameters was determined for each solution. After that, the maximum and mean values of the absolute relative errors ε_{max} and $\varepsilon_{\text{mean}}$ were computed. Initially, the error was studied using only one value of θ_{ext} in the input data. In

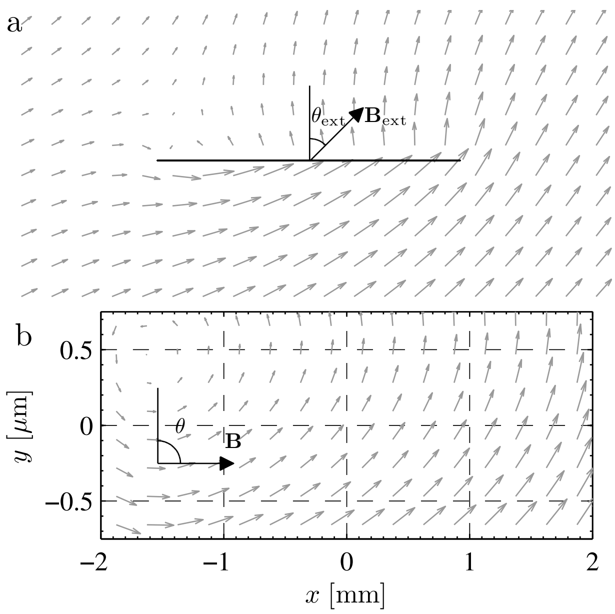

Figure 4.7: Gray arrows represent total magnetic field outside (a) and inside (b) of 123 A YBCO tape in external magnetic field: $B_{\text{ext}} = 20$ mT and $\theta_{\text{ext}} = 45°$.

this case, parameter errors especially in B_0 and γ were intolerably high, and their values were impossible to determine reliably. Consequently, for reliable results, input data should contain critical current values at various θ_{ext}.

As a rule of thumb, it is highly recommended that such θ_{ext} values be used that lead to as different critical currents as possible. That is why angles $\theta_{\text{ext}} = 0°$ and $90°$ were used in computations, and logarithmically distributed values were chosen from a magnetic flux density interval of 1 to 100 mT. It was also observed that Kim-model parameters can be determined with as few as four critical current measurements. Results for 4 and 16 measurement points are shown in figure 4.10. The more measurement points were used, the better the accuracy achieved, if δ remained below a certain limit, usually roughly 1% of the measured critical current value. However, beyond that limit, more measurement points may even lower the accuracy. The most inaccurate parameters were B_0 and α, which describe the rate of fall in J_c when the magnetic field is increased.

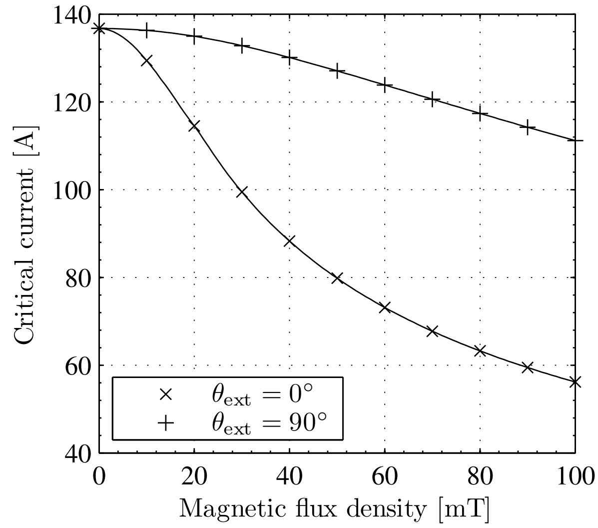

Figure 4.8: Generated measurements at external magnetic fields with (×) $\theta_{\text{ext}} = 90°$ and (+) $\theta_{\text{ext}} = 0°$. Optimization algorithm found originally assumed parameters, leading to perfect fit.

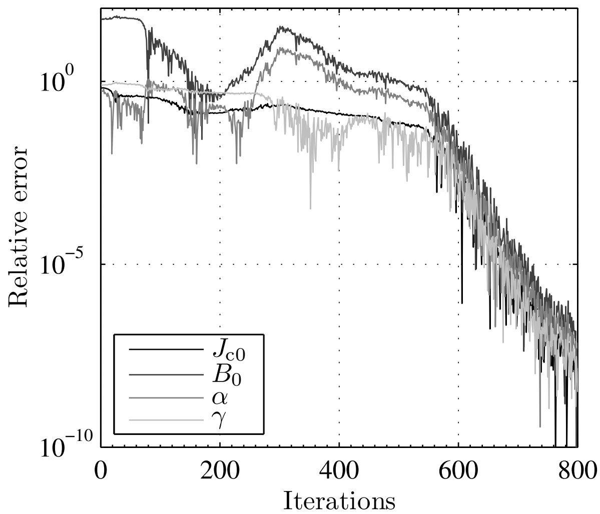

Figure 4.9: Convergence of Kim-model parameters with initial values of $J_{c0} = 1 \cdot 10^{10}$ A m^{-2}, $B_0 = 1$ T, $\alpha = 1$, and $\gamma = 1$. Correct values of $J_{c0} = 3 \cdot 10^{10}$ A m^{-2}, $B_0 = 20$ mT, $\alpha = 0.65$, and $\gamma = 5$ were attained after 709 steps.

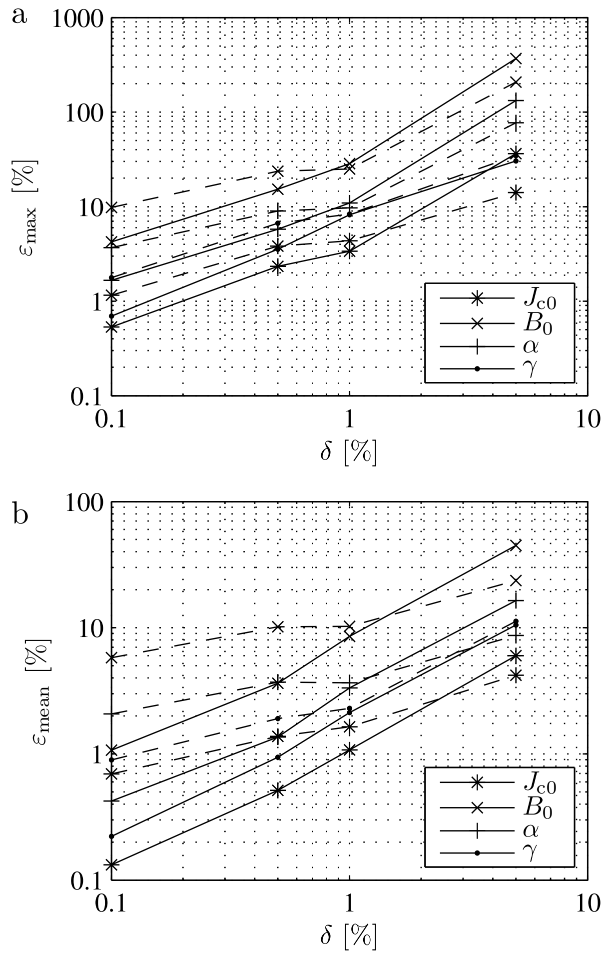

Figure 4.10: (a) Maximum and (b) mean error in Kim-model parameters as a function of maximum relative disturbance of critical current measurements; dashed lines computed with 4 measurement points and solid lines with 16 points.

4.2.2 Sample tapes

The method was also applied to two real, short samples, SS1 and SS2. SS1 had the cross-sectional dimensions of the YBCO layer, 3.8 mm × 2.5 µm. Measured critical currents are shown in figure 4.11a. All measurements were used to solve an optimal fitting curve with the following parameters: $J_{c0} = 0.90 \cdot 10^{10}$ A m^{-2}, $B_0 = 53.3$ mT, $\alpha = 0.74$, and $\gamma = 2.39$. On average, the measurements differed 4.0% from the fit. SS2 had a 4.0 mm × 1.3 µm YBCO layer. Critical current measurements were run at relatively low fields; consequently, the effect of the self-field shows clearly in figure 4.11b. In this case, measurements taken from various directions were exploited. The best agreement between measurements and computed values was achieved with parameters $J_{c0} = 0.92 \cdot 10^{10}$ A m^{-2}, $B_0 = 25.9$ mT, $\alpha = 0.79$, and $\gamma = 2.06$. On average, the fit and the measurements differed 2.7%. In comparison to parameters computed from SS1 and SS2, all other parameters except B_0 were almost equal.

With SS1 and SS2, the fitting curves aligned well with measurements, and the tapes' critical current could be determined for any external magnetic field. Particularly with SS2, the measured self-field effect matched the modeled one. However, according to figure 4.10, the difference between fit and measurements may lead to a significant error in parameter values. Especially B_0 appeared to be the most difficult to determine accurately, whereas the results of J_{c0} and γ were the most accurate. Clearly, two error components may affect the accuracy of parameters. First, an error may occur in voltage-current measurements, from which the critical current value is determined. Secondly, the external magnetic field may be inexact; for example, substrate magnetization may distort the field.

Furthermore, the uncertain cross-section of the superconductor or nonhomogeneous superconducting material may lead to wrong parameter values. Consequently, an integral element method must be developed to take into account the nonhomogeneous superconductor and possible magnetization. Possibly, because the Kim model may not necessarily be the correct $J_c(\mathbf{B})$-model either, measurements and model cannot converge even if all error factors are eliminated.

4.3 Cable's critical current

HTS power cables have one [100, 110] or several [69, 114] superconducting core layers, in which conductors are usually installed in circular form. In one-core-layer cables, the core usually determines the critical current of the whole cable.

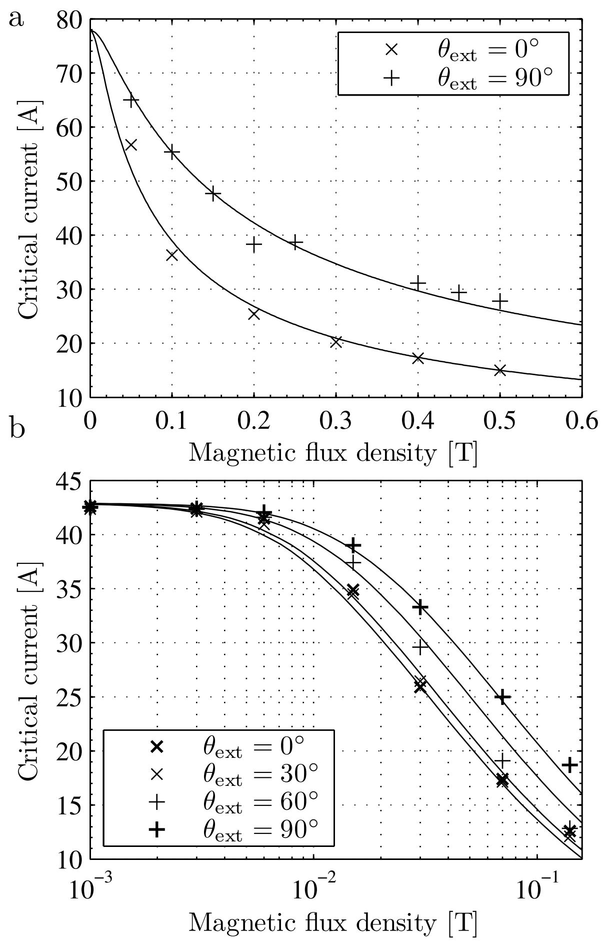

Figure 4.11: Measured critical currents and optimal fit as a function of external perpendicular (×) and parallel (+) magnetic field in (a) SS1 and (b) SS2.

This section examines a cable with a structure similar to that of the Super3C cable; that is, a one-core-layer cable in which a sufficiently small lay angle, for example, $\varphi \leq 20°$ was used. A small lay angle ensures a small axial field inside the cable; hence the cable can be safely modeled in its cross-sectional dimensions.

The core layer is surrounded by a normal or superconducting return conductor, which, if properly designed, creates only a negligible interior field. The critical current of the core tapes is expected to be reduced by the magnetic field created by the other tapes in the cable, a critical current reduction generally encountered, for example, in magnet applications [123]. However, in coaxial cables, the magnetic field perpendicular to the tape surface is decreased, because the fields of the neighboring tapes compensate for each other [103]. This can even lead to an increased critical current, if compared to a tape in the self-field. A possible increase in the critical current must be taken into account in estimating AC losses in superconducting cables. Here we extend the model in section 4.1.1 to cover the critical current of YBCO cables as well.

4.3.1 Computational model

In fully penetrated superconducting material, the critical current density distribution $J_c(\mathbf{r})$ depends on the magnetic flux density $\mathbf{B}(\mathbf{r})$, which again depends on $J_c(\mathbf{r})$. Here it is assumed that the current in the core flows perpendicular to the core cross-section, as shown in figure 4.12, and that $\mathbf{r}$ is a vector on the cross-sectional plane. The problem is to find such $J_c(\mathbf{r})$ that fulfills both relations simultaneously. For a numerical solution, the superconductor was divided into rectangular elements, and each element was assumed to carry a uniform current density. Then the critical currents of these elements were solved from a nonlinear system of equations

$$I_{e,i} = \mathrm{I_c}\left\{\mathbf{B}_i\right\} = \mathrm{I_c}\left\{\sum_j \mathbf{B}_{ij} I_{e,j}\right\} \tag{4.7}$$

by fixed point iteration [50]. The critical current in the ith element $I_{e,i}$ depends on the magnetic flux density in the element e_i, according to the relation $\mathrm{I_c}\{\mathbf{B}_i\}$. $\mathbf{B}_i$ is computed from the element currents by the superposition principle. Thus the notation $\mathbf{B}_{ij}$ means the magnetic field in the element e_i caused by unit current in the element e_j and its image elements, which due to the symmetry carry the same current as e_j. After the magnetic B_{ij} is computed for all i and j, they can be represented with the magnetic flux density tensor B.

The advantage of the previous approach is that B has to be computed only once, which speeds up the iteration process. In this work, B was computed using an analytical formula for a rectangle carrying a uniform current distribution [10]. In this case, the tapes are spaced equally and the superconductor is assumed homogeneous, that is, the distribution of element currents is equivalent and symmetric in all tapes. Therefore, only the current distribution in one half of the tape needs to be solved as shown in figure 4.12, and the total critical current of the whole tape I_c is two times the sum of the solved currents. However, asymmetric cables, which, for example, vary in critical current from tape to tape or have asymmetric tape configurations, can also be computed, but then the whole cross-section of the YBCO must be modeled.

Here the $J_c(\mathbf{B})$-dependence according to equation 2.6 was used again, and the relation between element critical current and element field could be written as

$$\mathrm{I_c}\left\{\mathbf{B}_i\right\} = SJ_{c0}\left(1+\frac{\sqrt{\gamma^{-2}B_{\parallel,i}^2+B_{\perp,i}^2}}{B_0}\right)^{-\alpha}, \tag{4.8}$$

where $B_{\parallel,i}$ and $B_{\perp,i}$ are the tape's parallel and perpendicular magnetic flux density components in the center of e_i, and S is the cross-section of the element.

The Richardson extrapolation helped markedly improve computation time and accuracy. The method exploits two coarse meshes instead of one fine mesh. The extrapolated critical current of a tape is obtained as

$$I_{cr}\left(h_s\right) = 2I_c\left(\frac{h_s}{2}\right) - I_c\left(h_s\right), \tag{4.9}$$

where $I_c\left(h_s\right)$ is the critical current of one tape computed with one mesh characterized by the relative step length h_s [1]. Here all tapes had $4/h_s$ times $1/h_s$ elements.

4.3.2 Gap effect

The computational model was applied to a YBCO cable to determine the total critical current of its tapes in cable use. The design parameters of this cable were similar to those of the Super3C cable as a default. The superconducting area of the tapes was 3.8 mm wide and 2.5 µm thick. $J_{c0} = 1.11$ MA cm^{-2} at 77 K was chosen to correspond to the self-field critical current of one tape, I_{c1} = 86.5 A. If the tape is installed in a cable with a radius of r = 15 mm and 18 tapes, its critical current increases to I_{c18} = 88.8 A. On the contrary, the critical current was expected to drop by more than 10%, based on traditional analysis of an average external magnetic field in the YBCO layer. Traditional analysis, which ignores the gap effect, was used to design the super3C-cable for a pessimistic estimate of its critical current. Here the cable radius was defined

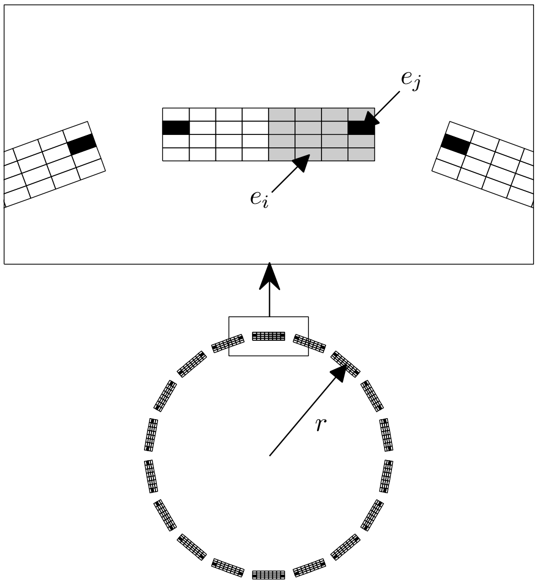

Figure 4.12: Cross-section of cable with 18 tapes. Only currents in the gray half of the tape are solved. Arbitrary element e_j from solved section and its image elements are marked black. Unit current in arbitrary element e_j and its image elements creates magnetic flux density in centre of element e_i.

as the distance between cable axis and tape centre, and a maximum of 24 tapes were fitted into the cable, resulting in $I_{c24} = 93.1$ A. Results were computed by the Richardson extrapolation with two meshes of 256 and 64 elements (h_s = 1/8 and h_s = 1/4) as a default.

To study the algorithm's numerical accuracy, the convergence of I_c with respect to h_s was computed. Figure 4.13 shows that the Richardson extrapolation yielded excellent accuracy with very coarse meshes. With any studied mesh, the Richardson extrapolation yielded somewhat more accurate results than direct computation with 1,024 elements ($h_s = 1/16$). Generating B consumed practically all the computation time and depended mainly on N_t and the number of elements in one tape $4/h_s^2$. For one mesh, it was roughly $N_t/h_s^4 \cdot 3.1 \cdot 10^5$ s, whereas the Richardson extrapolation took about $N_t/h_s^4 \cdot 3.3 \cdot 10^5$ s with the AMD Athlon 64 3400+. For example, I_{c18} with $h_s = 1/8$ was computed in 2.3 s.

Shown in figure 4.14, the critical currents in the elements of a single tape and in cables with 18 or 24 tapes illustrate the tapes' improved performance. Corresponding magnetic fields are illustrated in figure 4.15. In one tape, the maximum current density occurred in the middle of the tape, where the magnetic field was zero. When 18 tapes were installed to form a cable, the field created by the other tapes shifted the maximum current density towards the cable's axis. With 24 tapes, the gap effect became evident. Because of narrow gaps, the radial components of the magnetic field were canceled near the tape edges; the current density distribution was thus smoothed out, and the tape's critical current increased. Figure 4.15 underlines the fact that the gap effect also prevents the flux leaking inside the cable.

4.3.3 Effects of cable geometry and material properties

The gap effect takes place when the layer fill factor

$$f_l = \frac{N_t w}{2\pi r \cos(\varphi)} \tag{4.10}$$

is sufficiently large. The layer fill factor describes how much of the layer perimeter is covered by tapes. To conclude, I_c rises with increasing N_t or f_l, as shown in figure 4.16. Therefore, it is recommended that the layer be filled to its mechanical limits.

In principle, the critical current is affected by the parameters of the cable geometry r, w, and N_t. Therefore, I_c was studied near the default geometry, such that one of these parameters was varied and the other two were kept constant. In this manner, these variations can be given as variations of f_l, as shown in figure 4.17. Because the graphs describing the changes in w and in r lay on each other, it was not necessary to give I_c as a function of three variables r, w, and N_t. Instead it could be written as $I_c(w, r, N_t) = I_c(w/r, N_t)$ or $I_c(f_l, N_t)$, because cable dimensions are largely compared to the thickness of the YBCO layer. Also the difference between the graphs describing changes in w and in N_t is small. Thus if we study the cable geometries near the default geometry, with good accuracy we can approximate I_c to be a function of f_l only.

The critical current was scrutinized as a function of N_t in a broad range. Figure 4.18 shows a change in the critical current within a commonly applied layer fill factor range of $0.8 < f_l < 1$ in cables with 5–40 tapes. The highest critical current is achieved if the tapes form a perfect circle; thus if N_t is increased, the tapes' critical currents increase, because the cable geometry becomes more circular. Hence a gained increase of I_c must converge as N_t tends to infinity. With a given superconductor thickness and $J_c(\mathbf{B})$-dependence, the theoretical upper limit for increase in I_c was 10.9%. However, all practical advantage is gained with 20–30 tapes. Only slight improvement was observed in I_c, if more tapes were added; at the same time though cable dimensions could become intolerable.

However, with the I_c-values of commercial tapes increasing, the gap effect can become more important. In fact, as high critical currents per tape width as 495 A cm^{-1}, corresponding to $J_{c0} \approx 2.6$ MA cm^{-2}, have been reported [116]. Thus the gap effect was studied in a cable of 25 tapes as a function of J_{c0}. Figure 4.19 summarizes the results, which suggest that the benefit of the gap effect increases with the quality of the YBCO. For example, with $J_{c0} = 2.6$ MA cm^{-2}, I_c can rise up to 16% in cable use.

4.4 Concluding remarks

This chapter discussed the effect of the tape's self-field on the critical current of the YBCO tape. A new method was developed to solve the critical current of a YBCO tape from its intrinsic material parameters, and the other way round, a method to determine the intrinsic $J_c(\mathbf{B})$-dependence of the YBCO from voltage-current measurements. By exploiting the solved $J_c(\mathbf{B})$-dependence, the critical current was then determined in the cable's magnetic environment.

The model was also used to study computationally the effect of the self-field on the critical current as a function of film thickness. The self-field effect inevitably reduces the critical current density with increasing YBCO film thickness and total current. In practical YBCO samples, the average critical current density does not depend on sample width but decreases with increasing film thickness in the self-field. To distinguish the self-field effects from problems

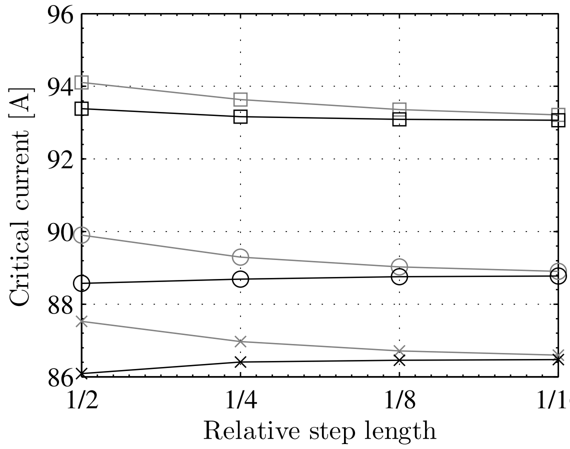

Figure 4.13: Algorithm convergence with a cable of 1 (×), 18 (○), and 24 (□) tapes. Gray curves are computed directly and black curves with Richardson extrapolation using meshes with h_s and $2h_s$; $h_s = 1/2$, 1/4, 1/8, and 1/16 correspond to 16, 64, 256, and 1,024 elements, respectively.

related to the manufacturing process, it was proposed that critical current measurements be made in the external field perpendicular to the film surface such that the external field exceeds the maximum value of the self-field's perpendicular component. The effect of the self-field depends on material $J_c(\mathbf{B})$ characteristics. Throughout this work, the $J_c(\mathbf{B})$-dependence was assumed to follow the Kim model, which was modified to take anisotropy into account. However, the Kim model parameters varied between the tapes.

Because of the above, an optimization method was developed to determine YBCO characteristics and applied to two different sample tapes. First, the critical current was measured at various external magnetic fields. Then a $J_c(\mathbf{B})$-dependence was searched that would optimally fit measurements. Measurements can be made at low fields, even below 0.1 T, because the distortion of the external magnetic field, caused by the sample's self-field, is taken into account. In addition, the $J_c(\mathbf{B})$ model can be assessed for validity at low fields.

The computational search for the Kim model parameters turned out to be difficult, yet parameters could be determined for one sample in less than a minute with the Nelder-Mead Simplex algorithm. Parameters can be determined accurately with enough high-quality measurement data with various external magnetic field norms and directions. However, any measurement error in critical current values should be roughly below 1%, because only then added measurement points can improve accuracy. Furthermore, it should be consid-

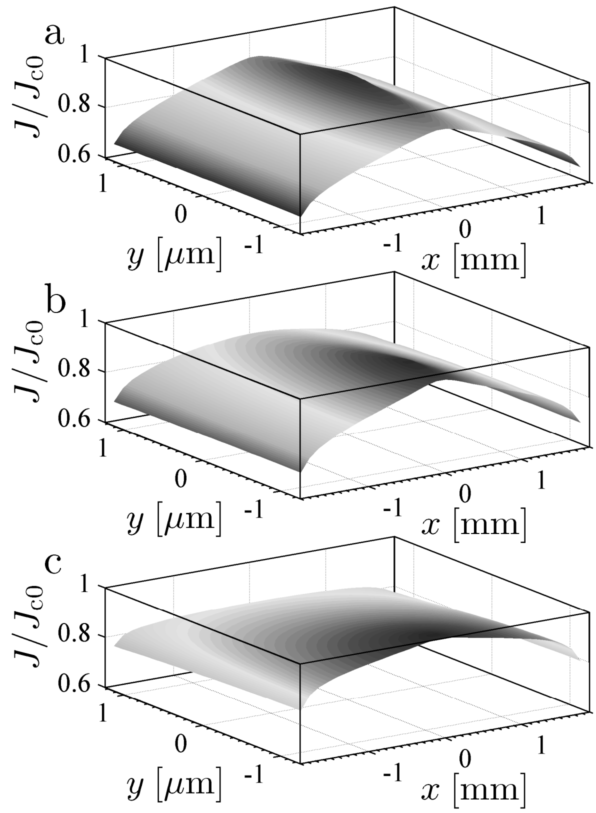

Figure 4.14: Normalized current density distribution in (a) single tape, (b) 18 tapes, and (c) 24 tapes. Black color corresponds to 0.6 and white to 1.

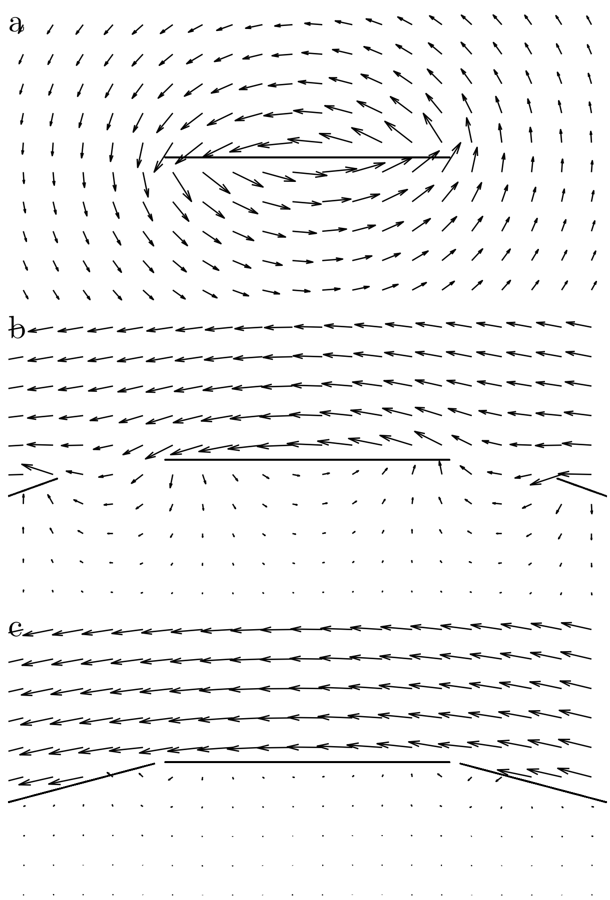

Figure 4.15: Magnetic field caused by currents in figure 4.14; (a) single tape, (b) 18 tapes, and (c) 24 tapes.

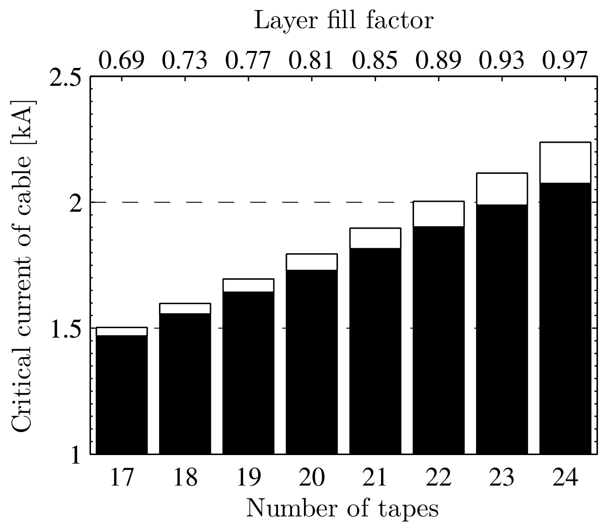

Figure 4.16: Critical current of default cable as function of tape number. Total height of bar is cable's computed critical current . Height of black bar is critical current of individual tape multiplied by tape number.

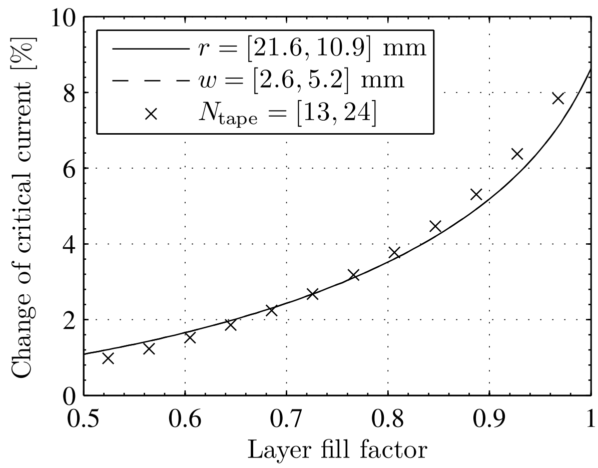

Figure 4.17: Change in critical current as function of layer fill factor: (solid line) $w = 3.8$ mm, $N_{\mathrm{t}} = 18$, r is varied; (dashed line) $r = 15$ mm, $N_{\mathrm{t}} = 18$, w is varied; ($\times$) $r = 15$ mm, $w = 3.8$ mm, N_{t} is varied.

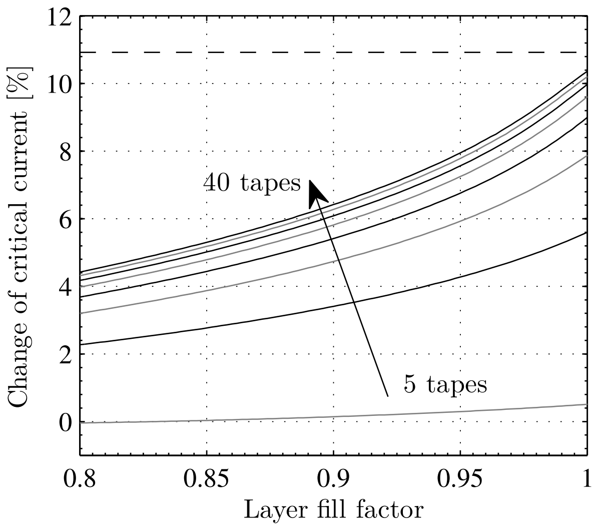

Figure 4.18: Change in critical current as function of layer fill factor. Lowest curve corresponds to cable with five tapes; other curves are at five-tape interval up to 40 tapes from bottom to top. Dashed line represents theoretical upper limit.

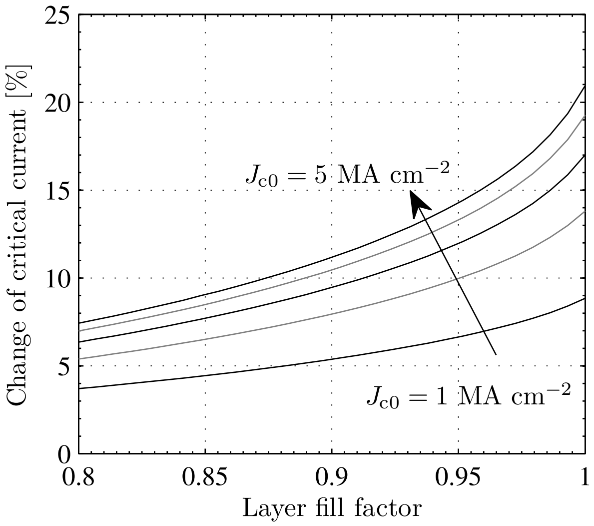

Figure 4.19: Change in critical current as function of layer fill factor computed for cable with 25 tapes. Gap effect increases with zero field critical current density, and curves are computed with 1 MA cm^{-2} interval.

ered that measurements may be affected by the nonhomogeneity of YBCO or the magnetization of the substrate. Also, the Kim model is only an approximation of the $J_c(\mathbf{B})$-dependence, and not necessarily an accurate one.

Finally, the effect of the cable geometry on the critical currents of YBCO tapes was studied, and the efficiency of the numerical algorithm was greatly improved by the Richardson extrapolation. The critical current of one tape rises if the tape is transferred from self-field to cable field. The relative increase in critical currents was constant for all studied one-layer cables with similar geometric proportions; hence the layer fill factor was defined as describing these proportions. Furthermore, a small change in the number of tapes had no significant impact on the results; the cable's critical current could then be determined solely as a function of the fill factor. Results suggested that in practical one-layer cables, the tape's critical current can rise about 5%, compared to the self-field values. However, in future, better tapes will incorporate an even more substantial gap effect. Finally, the critical current values computed here should be used to solve AC losses. As shown in section 3.3.3, the AC loss measurements of the 0.5-m test cable suggested that critical currents should be higher than previously expected. Unfortunately, these measurements could not be used to verify the critical current values computed here, because the tapewise current deviation in the 0.5-m cable was too high. We must wait until the critical current and AC losses of a full-length Super3C cable can be measured.

Chapter 5

Fault current analysis

So far, analysis has been restricted to the under-critical case, in which the major loss components are heat leak to the cryostat and AC losses. Because these components are small, stable operation can be easily maintained. However, due to extremely high current densities in very thin superconducting films, YBCO cables are sensitive to overcurrents. High resistivity at an overcritical current and low specific heat make the situation even worse. Because in a modern power grid the cables may have to resist fault currents of up to 40 kA (rms), it is essential that we are able to predict the cable's heating and current transport properties during a short-circuit.

This chapter introduces a 1D FEM model to determine simultaneously both current density and temperature distributions in the cable's cross-section as functions of time. Real temperature-dependent properties of cable materials were included, and the strong magnetic field and the current density dependence of superconductor resistivity were taken into account. The model was used to study the stability of various 1-kA YBCO cable geometries at several fault current waveforms.

The 1D model does not take into account the effect of the twisting of the layers and the gap effect. However, small lay angles are preferred in two-layer YBCO cables to curtail AC losses. Modeling of the gap effect leads to a 2D problem, which is difficult and slow to solve because of mesh-related problems induced by the high aspect ratio of YBCO.

5.1 Nonlinear 1D FEM model

The electrical insulation surrounding the cable former acts as thermal insulation as well. Therefore, it is adequate to model just the core layer and the cable former, which is the main source of heat when a fault current occurs.

The modeled part of the cable is shown in figure 5.1 with four sub-domains: copper former, steel substrate, YBCO, and silver shunt.

The thermal and electromagnetic model of the HTS presented in section 2.2 was solved with the FEM, a time-consuming task because the resistivity of the superconductor ρ_{YBCO} is highly nonlinear, as described in section 2.3. However, moderate computation times were achieved in the cylindrical symmetric case, in which all quantities depended on radius r and time t and equations 2.2 and 2.3 reduced to

$$\begin{cases} \frac{\partial}{\partial r}\rho\frac{1}{r}\frac{\partial}{\partial r}rH = \mu_0\frac{\partial H}{\partial t} \\ \frac{1}{r}\frac{\partial}{\partial r}rk\frac{\partial T}{\partial r} + \rho J^2 = C_{\mathrm{p}}\frac{\partial T}{\partial t} \end{cases}, \tag{5.1}$$

where

$$J = \frac{1}{r}\frac{\partial}{\partial r}rH \tag{5.2}$$

[4]. $\rho(T)$, $C_{\mathrm{p}}(T)$, and $k(T)$ are presented in figure 5.2.

In the geometry shown in figure 5.1, H is zero at the inner radius of the former r_0, because no current flows in the duct. For a cable without a duct, r_0, equals zero. The total fault current $i_{\mathrm{f}}(t)$ determines the boundary condition at r_4 as

$$H(r_4, t) = \frac{i_{\mathrm{f}}(t)}{2\pi r_4}. \tag{5.3}$$

For the heat conduction equation, the boundary condition for cooling was set at r_0.

$$k(r)\frac{\partial T}{\partial r}\bigg|_{r_0} = h\left(T(r_0) - T_0\right), \tag{5.4}$$

where $T_0 = 77$ K is the temperature of the liquid nitrogen and h the convective heat transfer coefficient [40], which equals zero in the adiabatic case. h was always zero at the boundary r_4. The initial values $T(r, 0) = T_0$ and $H(r, 0) = 0$ A m^{-1} were used. Furthermore, there were no electrical or thermal contact resistances; that is, H and T were assumed continuous.

According to Ampère's law (see equation 2.1), the instantaneous current $i_{\mathrm{f},j}(t)$ in the jth material can be computed from the solution $H(t, r)$ as follows.

$$i_{\mathrm{f},j}(t) = 2\pi\left[r_j H(t, r_j) - r_{j-1}H(t, r_{j-1})\right], \tag{5.5}$$

where $j \in 1, 2, 3, 4$.

An arbitrary fault current function can be used for $i_{\mathrm{f}}(t)$, but in a real power grid ordinary fault currents can be simulated as

$$i_{\mathrm{f}}(t) = \sqrt{2}I_{\mathrm{rms}}\left[\sin(2\pi ft + \phi) - \sin(\phi)e^{-\tau 2\pi ft}\right], \tag{5.6}$$

where I_{rms} is the rms value of the oscillating current component with 50 Hz frequency. ϕ is the fault current starting phase, and the constant $\tau = 0.02$ depends on the topology of the power grid [55]. Fault currents resulting from equation 5.6 are shown in figure 5.3. Fault current durations are typically less than 0.5 s, because the breakers switch off the current.

The resistivity model described in section 2.3 was used here with the exception that the critical surface model according to reference [106] was used instead of equation 2.9 as follows:

$$J_{\mathrm{c}}(H,T) = \frac{1}{1+\left(\frac{\mu_0 H}{b_0}\right)^{\alpha'}} \cdot \frac{T^* - T}{T^* - T_0} \cdot J_{\mathrm{c0}},\ T < T^*. \tag{5.7}$$

Figure 5.4 presents a set $J_{\mathrm{c}}(H,T)$-characteristics used here. They are described by the parameter values $b_0 = 56$ mT and $\alpha' = 0.6$. $J_{\mathrm{c0}} = J_{\mathrm{c}}(0\ \mathrm{T}, 77\ \mathrm{K})$ equals the amplitude of 1 kA (rms), divided by the cross-section of YBCO. Furthermore, a constant n-value ($n = 10$) was used to ensure the monotonicity of $\rho_{\mathrm{sc}}(H,J)$. These parameters represent the state-of-the-art values of the year 2005. Here, the normal resistivity value was modeled as

$$\rho_{\mathrm{n}} = 6.5 \cdot 10^{-11} \cdot T + 1.0 \cdot 10^{-8}\ (\Omega\ \mathrm{m}), \tag{5.8}$$

which results in $1.5 \cdot 10^{-8}\ \Omega$ m at 77 K [85].

5.2 Fault current distribution and stability

This computational model was developed to design the first YBCO cables. Because no large-scale YBCO cables have been constructed so far, the computational results cannot yet be verified experimentally. Therefore, example runs are presented here with the aim to provide insight into the interplay between current sharing, temperature increase, and varying magnetic fields. All simulations were done using a self-made MATLAB program exploiting FEMLAB subroutines. A mesh of about 800 nodes was used, and typically 50 nodes were in YBCO. About two hours were needed to simulate a 0.5-s fault current with the AMD Athlon$^{\mathrm{TM}}$ 64 3400+ and 1.5 GB of RAM.

The cable geometry and dimensions used here are based on the constructed 1-kA HTS cable prototype [74]. The area of the copper cross-section was $S_{\mathrm{f}} = 4\ \mathrm{cm}^2$; that is, the radius of the former r_1 varied between 11.3 and 19.6 mm, depending on the cooling duct radius r_0. The steel substrate, YBCO layer, and silver shunt were of thickness 0.1 mm ($= r_2 - r_1$), 1.5 µm ($= r_3 - r_2$), and 0.5 µm ($= r_4 - r_3$), respectively.

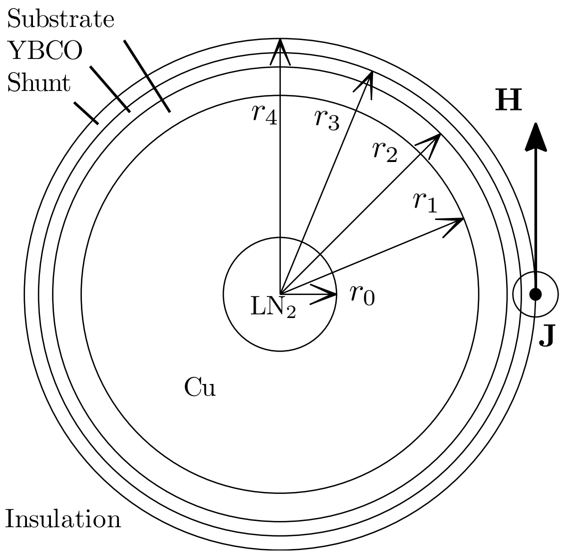

Figure 5.1: Core cross-section. Current density and magnetic field intensity are defined positive if they are oriented according to the figure. Dimensions are not to scale.

In cables, segmental type conductors are typically used as stabilization formers to reduce eddy currents [3]. However, only tubular copper formers were studied here for three reasons. First, it has been shown that a short YBCO cable can be designed to operate also as a fault current limiter [58]. In such a system, solid copper formers could be useful for dissipating energy during fault currents. On the other hand, eddy current losses can also be easily cut, if a cooling channel is made inside the former. Furthermore, the performance of a computational model can be effectively tested only if the former structure is kept simple.

First, several different fault currents were studied in a cable without a cooling duct. Almost all fault current was shared between the copper and YBCO; that is, only minor currents flowed in the steel and silver. Figure 5.5 presents current distribution in the former and currents in the copper and YBCO as a function of time. A small I_{rms} value of 2 kA was used to emphasize the nonlinear current sharing characterized by the superconductor. When $\phi = 0$, current density distributions look almost like Bessel functions, though small differences arise due to the nonlinear resistivity of YBCO and the transient effects during the first fault current cycle. First, the current in YBCO increases. When the current transfer capacity of YBCO reaches its limit, an additional current starts to flow in the former. Increasing, the current creates a magnetic field, which reduces the critical current and, thus, diminishes the current in

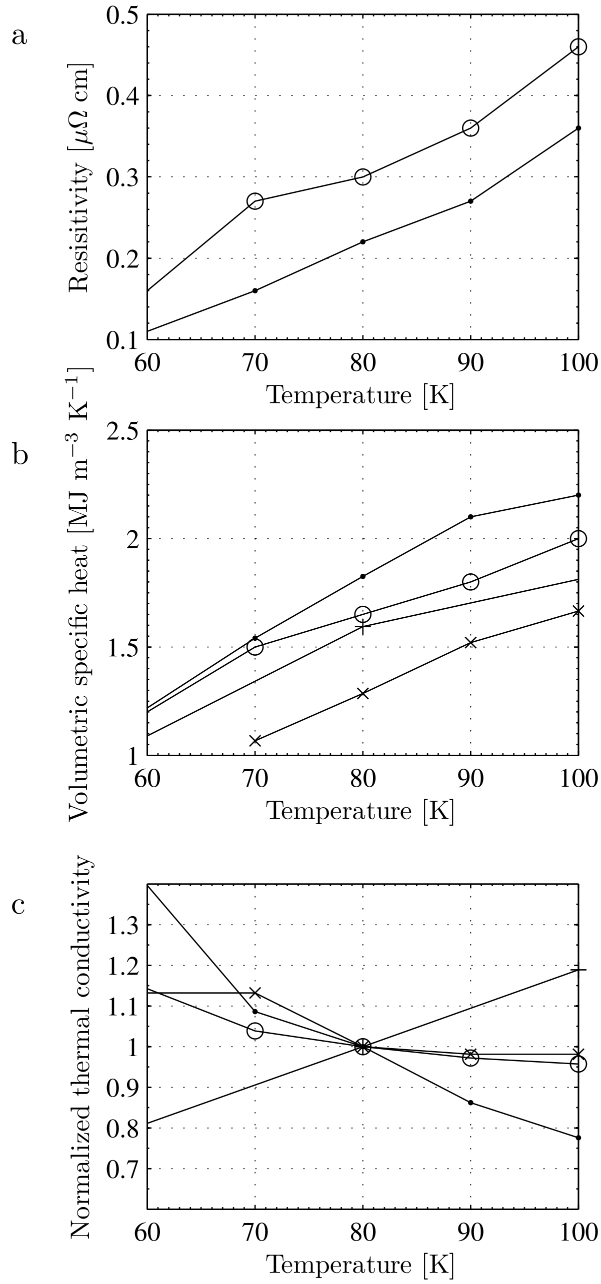

Figure 5.2: (a) Interpolated resistivities of (·) copper [42] and (∘) silver [43]. (b) Interpolated volumetric specific heats of (·) copper [42], (+) stainless steel [91], (×) YBCO [8], and (∘) silver [42]. (c) Interpolated and normalized thermal conductivities. The values of thermal conductivities at 80 K are (·) 580, (+) 7.57, (×) 0.530, and (∘) 464 W m^{-1} K^{-1}, respectively.

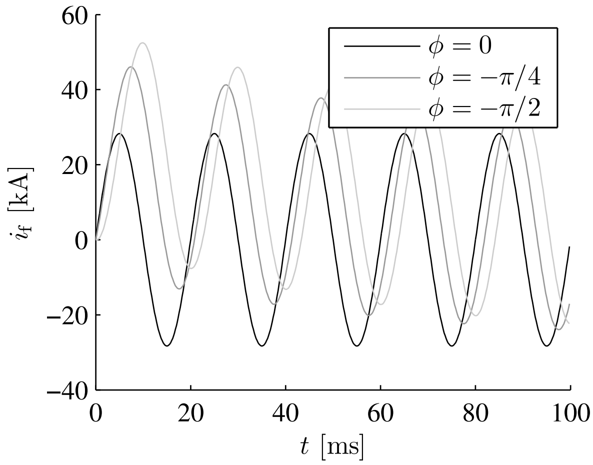

Figure 5.3: Part of 20-kA (rms) fault currents with three closing angles. Exceptionally $\tau = 0.05$.

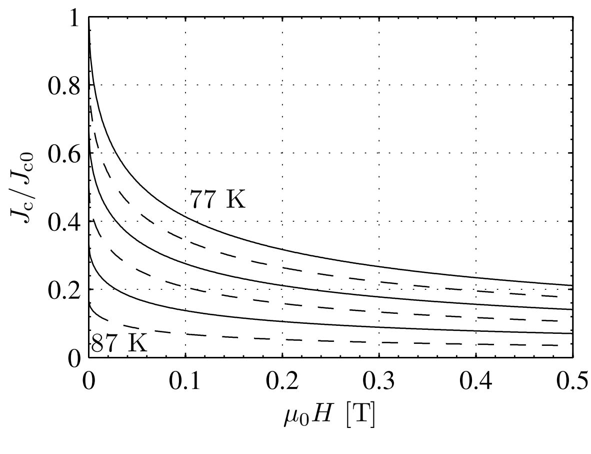

Figure 5.4: Normalized $J_c(H, T)$-dependence of YBCO. $J_c(H)$ characteristics are sketched at 2-K intervals.

YBCO. Just before 10 ms, the current in YBCO changes directions, and at 10 ms, a remanence current circulates between YBCO and copper. After that, also the current in the copper changes directions.

Figure 5.6 shows the temperature evolution in YBCO, T_{YBCO}, due to fault currents. T_{YBCO} was defined here as the mean temperature of YBCO layer, but spatially the temperature in YBCO layer varied at most by 0.02% of the mean value. T_{YBCO} rose at a nearly constant rate. Only at first, the temperature rose quickly before the temperature difference increased between YBCO and steel, and thermal conduction started slowing down the heating. On the other hand, when the current was close to zero during a cycle, YBCO temperature dropped, because substrate and former absorbed thermal energy from YBCO. The increasing T_{YBCO} caused the current in the superconductor to decay, as shown in figure 5.7.

5.3 Temperature

Though no measurement data is available, the results can be compared with conventional analytical stability analysis. In a simple fault current model, heating in the cable was computed with the assumptions that all current flowed through the former, and that no eddy currents were created. The temperature of the cable was then solved from

$$\frac{\mathrm{d}T}{\mathrm{d}t} = \frac{\rho(T)}{C_{\mathrm{p}}(T)} \frac{i_{\mathrm{f}}(t)^2}{S_{\mathrm{f}}^2} \tag{5.9}$$

with an initial condition $T(0) = T_0$ [123]. An explicit Runge-Kutta algorithm was used here, [24] but the equation could be solved analytically as long as the approximations of $\rho(T)$ and $C_{\mathrm{p}}(T)$ were kept simple enough.

According to the FEM and equation 5.9, the ratio η between temperature rises was almost independent of I_{rms} at between 5 and 40 kA (rms), as shown in figure 5.8. This means that after η was determined with FEM computations at one I_{rms}, the temperature of YBCO could be accurately estimated as $T_{\mathrm{YBCO}} = \eta T + (1 - \eta)T_0$. However, this approximation does not apply to low currents, because then only a small share of the fault current heats the former. For example, in figure 5.8, the curve computed with $I_{\mathrm{rms}} = 2$ kA stands clearly apart from the other curves.

In a solid former, eddy currents cause most of the heat. However, if a duct is made inside the former, eddy currents and, thereby, heat generation can be minimized [3]. To study the effect of the former geometry on the cable temperature, the copper former cross-section was kept constant, but the area of the cooling duct cross-section S_{d} was varied, as shown in figure 5.9,

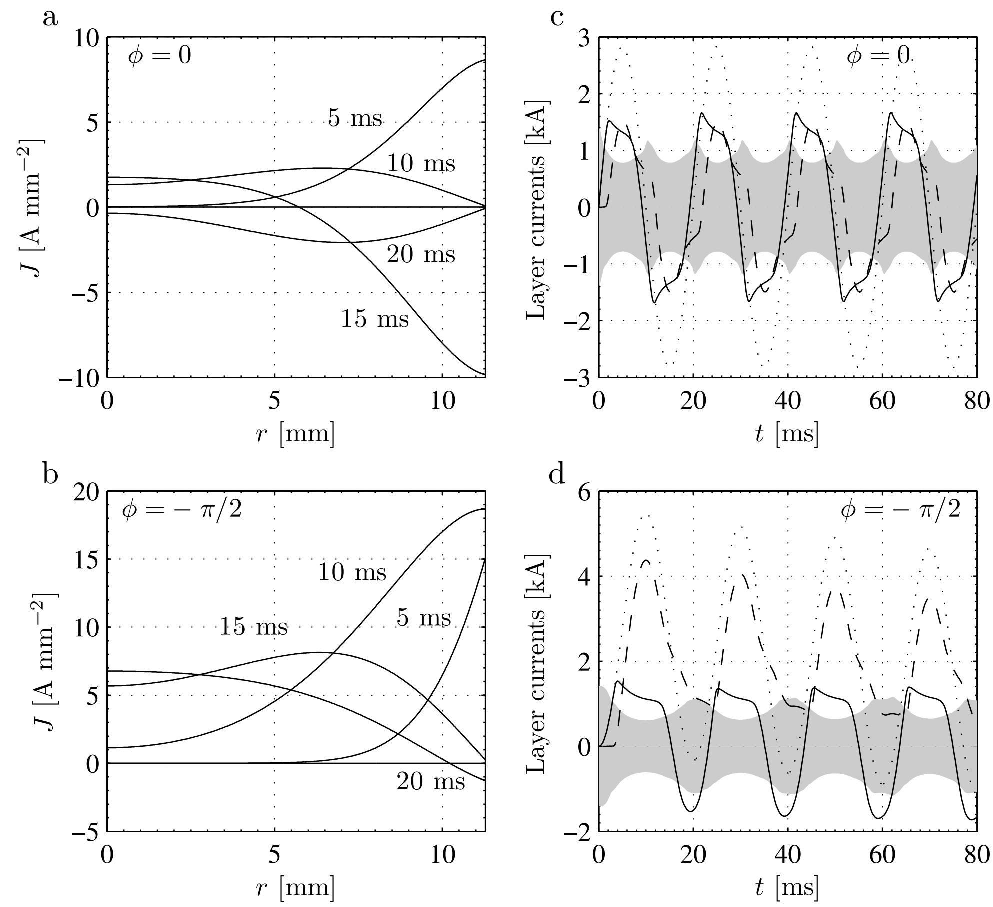

Figure 5.5: Current density along former radius at four different times during first current cycle when (a) $\phi = 0$, (b) $\phi = \pi/2$. Currents in YBCO (solid line) and former (dashed line) as function of time are shown in (c) $\phi = 0$ and (d) $\phi = \pi/2$. For comparison, total fault current $I_{\text{rms}} = 2$ kA is shown with dotted line. In shaded area, current in YBCO is below critical value.

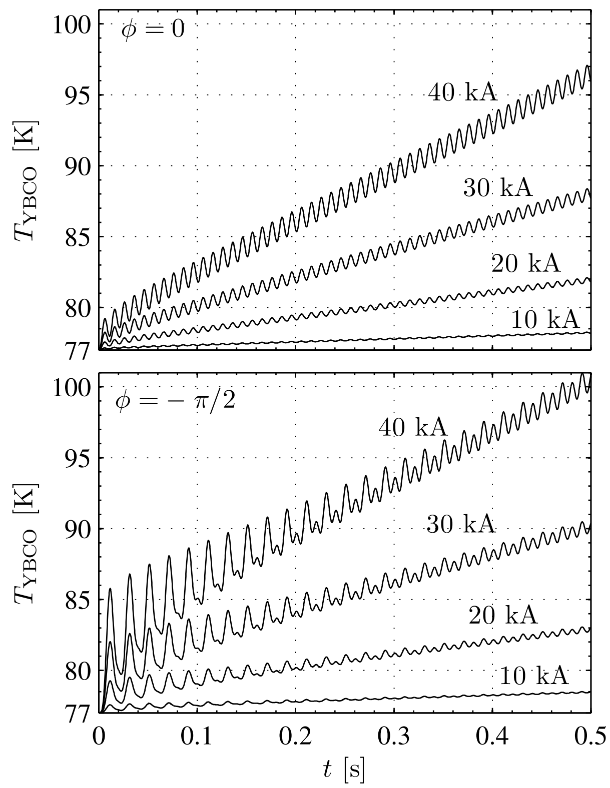

Figure 5.6: Temperature evolution in YBCO layer with I_{rms} of 10, 20, 30, and 40 kA.

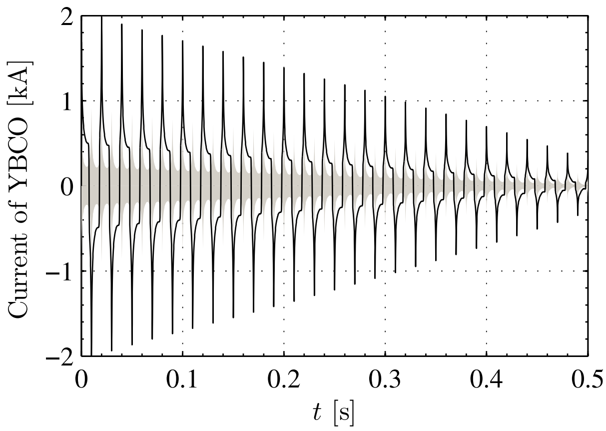

Figure 5.7: Current decay in YBCO layer at 30-kA sinusoidal fault current. In shaded area, current is below critical value.

at $I_{\mathrm{rms}} = 30$ kA and $\phi = 0$. Already at 2 cm^2, the duct could bring down the maximum temperature from 88 K to 84 K. Results were also compared to predictions from equation 5.9. Note that at small fault currents, η can be less than one because a large fraction of the current flows in the superconductor.

The cable should be designed so that it reaches its operating temperature before the current is switched on again after circuit breaker operation. Therefore, sufficient cooling is needed. However, in LN_2-cooled cables, h values can vary in a broad range depending on, for example, the flow velocity. In nucleate boiling conditions [40], h can exceed 10,000 W m^{-2} K^{-1} [6], but usually nitrogen is not allowed to boil in the duct. The results of example runs at different h, shown in figure 5.10, illustrate the effect of cooling on cable behavior. In the former, LN_2 cooling reduces the peak value of T_{YBCO}, and the cable recovers after a time. Only if $h \geq 50,000$ W m^{-2} K^{-1} could normal operation temperature be reached in less than 0.5 s. If the current is switched on before the operating temperature is reached, the cable may start heating again and lose its stability.

5.4 Concluding remarks

A nonlinear and time-dependent FEM model was developed to simulate simultaneously current sharing and temperature distribution in a superconducting YBCO cable during a fault current. The model included the temperature-dependence of the cable materials. Furthermore, the YBCO resistivity model took into account magnetic field dependence of current density, which effected on the results below 5 kA (rms) fault currents.

Because a wide range of fault current waveforms can occur in a real power grid, various fault currents were simulated with several cable geometries and cooling parameters. Simulations illustrated nonlinear current sharing between former and superconductor. According to simulations, 0.5-s fault currents at different magnitudes lifted the temperature of YBCO almost linearly as a function of time. The cable could cope with fault currents of up to 20 kA, but at higher fault currents, eddy currents in the copper former generated high losses, and stability was lost.

A cooling duct inside the former reduces eddy currents and, thereby, lowers the peak temperature of the YBCO layer in the cable core. The peak temperature can be further reduced by heat transfer to LN_2; the cable can then recover after the circuit breaker has switched off the current. The cable with both a former and a cooling duct cross-section of 4 cm^2 could cope with a sinusoidal 0.5-s and 40-kA (rms) fault current without exceeding 89 K.

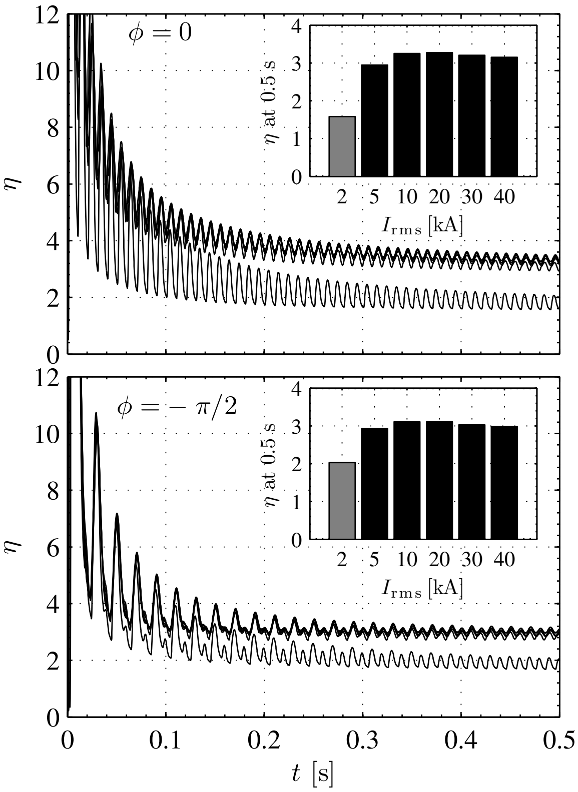

Figure 5.8: Ratio between temperature rises from FEM model and equation 5.9. Almost superimposed black curves are computed with 5, 10, 20, 30, 40 kA fault currents. Gray curve represents 2-kA fault current. Ratios at 0.5 s are shown in insets.

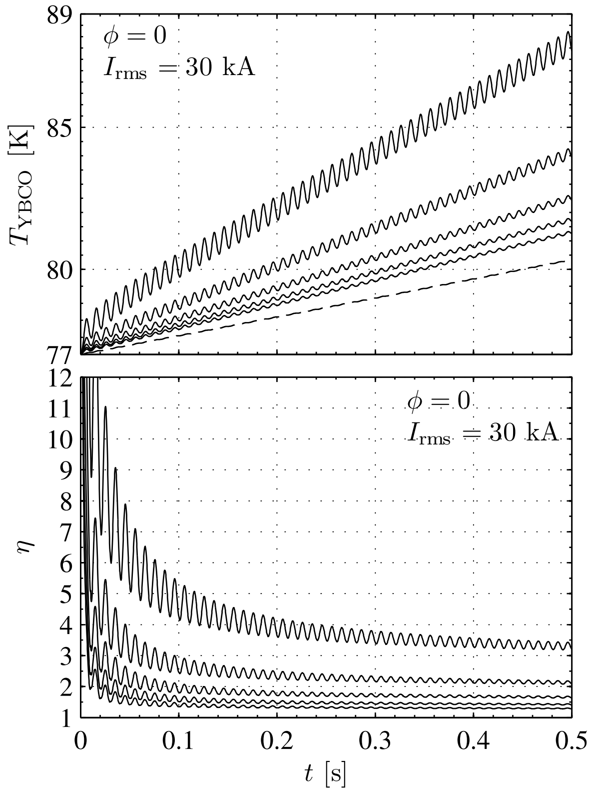

Figure 5.9: Temperature evolution and ratio, η, between temperature rises according to FEM and equation 5.9 with two different fault currents. Curves from top to bottom correspond to $S_{\rm d}$ of 0, 2, 4, 6, and 8 cm^2. Dashed line results from equation 5.9.

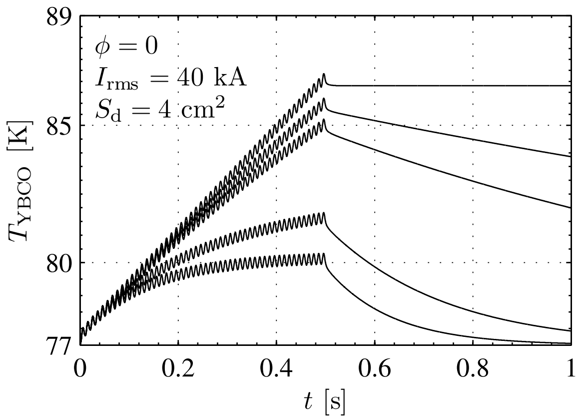

Figure 5.10: Effect of cooling on YBCO temperature. Curves from top to bottom correspond to convective heat transfer coefficients of 0, 5 000, 10 000, 50 000, and 100 000 W m^{-2} K^{-1}.

Chapter 6

Application: 1-kA demonstration cable

This chapter concludes the design work on the Super3C cable incorporating cryogenic, mechanical, and electromagnetic aspects. Here emphasis is on the electromagnetic side of the work. However, cryogenics and mechanical restrictions cannot be totally omitted, because cryogenics limit the size of the superconducting layers and determine the operating temperature and maximum heat generation during normal and fault current conditions for stable operation.

Mechanical design limits the minimum gaps between the CC tapes and the minimum lay angles to make cabling feasible and handling manageable. In addition, mechanical design ensures that CC tapes are not exposed to harmful forces especially during cooling. Electromagnetic design aims to minimize heat generation and fault current conditions in normal operation. Moreover, the design of the electrical insulation should, as far as applicable, follow the international standard.

6.1 The design

The Super3C project aims to establish the feasibility of a low-loss, HTS, AC cable using CC tapes as the current carrying elements. It comprises the development, manufacture, and testing of a functional model consisting of a one-phase, 30-m, 10-kV, 1-kA coaxial cable. The cable is connected to the network through a termination at each end, and it will be of the cold dielectric type requiring cooling with pressurized liquid nitrogen. The core will be composed of a flexible former, designed to carry currents during a short circuit in the grid. The former supports the conductor, consisting of one layer of HTS tapes. The dielectric insulation is based on lapped, polypropylene-laminated paper (PPLP), impregnated with LN_2. The shield layer consists of HTS tapes for normal operation and a Cu layer for a short circuit event.

Currents in the shield layer and core layer are equal in magnitude but opposite in direction. Consequently, the cable will not generate any significant external magnetic field and will demonstrate very low impedance. As each phase in such a system is electrically and thermally independent, manufacturing one phase only will provide the same output data, at a lower cost, as the test of an AC cable with three independent phases.

A successful electromagnetic cable design takes the mechanical limits imposed on it, adds them to the electromagnetic limits of the CC tapes, and minimizes, within given boundaries, the cable's total electromagnetic losses.

The cable design was based on a tape I_c of roughly 85 A, since the present result of I_c per tape width was 235 A cm^{-1} at 77 K and the self-field was measured in the project. Forty-meter CC tapes can easily meet that requirement. The former diameter and insulation thickness determine the radius of the CC tape layer, whereas the tapes' transport current and I_c define the number of CC tapes in the core and shield layers. A slight overcapacity in amperage should be used in the cable to keep AC losses moderate and to compensate for possible uneven distribution of I_c between tapes. Fortunately for a 1-kA cable, one layer of the given CC tapes in the core and one layer in the shield is enough to carry the specified design current. With two layers, an uneven current share between the layers is not a problem, and determining only two lay angle parameters becomes easy, compared to optimizing a multilayer structure [85].

Lay angles were optimized with a circuit-analysis-based model for AC losses presented in section 3.1.1. The model takes into account the strong $I_c(B, T)$-dependence of the CC tapes. However, the effect of the neighboring tapes reduces AC losses in the YBCO tapes. It is difficult and time-consuming to estimate the reduction with any field-theory-based model due to the flat geometry of the YBCO layer. In addition, the gaps are not of equal size, because the tapes can move in the cable, for example, due to bending. Therefore, the effect of neighboring tapes was not taken into account in the model.

The $I_c(\mathbf{B})$-dependence was the same as that used in section 3.2. Since the stranding machine limits lay angles to at least 17.66°, figure 6.1 shows simulation results up from that angle. The data was calculated assuming that both the core and shield layer shared the same laying direction; opposite laying directions would result in much higher losses due to combined magnetic flux densities. As figure 6.1 indicates, minimal losses were attained with the smallest possible lay angles, due to the minimization of the magnetic fields.

Another important factor is the radial magnetic flux density at the edge of the CC tape. This is a major cause for measured AC loss in the CC tape due to the anisotropic magnetic flux dependence and the large width to thickness ratio of the YBCO layer. The situation can be improved by increasing f_l to compensate for the radial field and, thereby, effectively increase the tape's I_c and reduce AC losses [117]. Unfortunately, mechanical design needs non-zero gaps for cable manufacture and bending, which limit design options in this regard.

The functional model specifications were loosely based on the IEC international standards, mainly IEC60183, IEC60071, and IEC60141-1/IEC60055-1, since the cables to be made later must be compatible with an existing network. Because the cable concept was of the cold dielectric type, and the dielectric material had to fulfill its requirements in cryogenic conditions, the cable design exploited lapped insulation impregnated with LN_2. In this way, the inner layers could be cooled without specific cooling ducts, and LN_2 could be used as part of the dielectric layer. The dielectric tape consists of PPLP with carbonized paper as dielectric. This insulation technology has been tested successfully in various other projects.

When all design aspects are interconnected, conflicting requirements often arise. Therefore, a final design must be searched for iteratively. All the requirements are fulfilled in the design shown in figure 6.2 and table 6.1. The former consisted of several thin copper wires braided to reduce eddy current losses and to ensure the cable was mechanically flexible. The CC tapes were 4 mm wide and 0.1 mm thick. In the 1-kA cable, the core layer required 18 tapes with $I_c(0\ \mathrm{T}, 77\ \mathrm{K}) > 86.5$ A and the shield layer 27 tapes with $I_c(0\ \mathrm{T}, 77\ \mathrm{K}) > 56$ A. Both layers had a lay angle of 17.66°. Therefore, the unit length of the 30-m cable with 5-m terminations was 36.7 m, and the total length of the CC tape used was 1,652 m. To illustrate the performance of the cable, AC losses were estimated using the circuit analysis model in section 3.1.1. Figure 6.3 shows calculated AC losses for the final design at three different temperatures within an operating temperature range of 70–77 K.

After the cable is finished, AC losses will be determined by electrical measurement, in which the so-called secondary voltage method will be used. This method was developed and successfully tested on single HTS tapes and small coils. A testing current was delivered across a transformer, that is, the secondary current of a power transformer, as shown in figure 3.7. This feature is particularly important in multi-tape structures, in which correct placement of voltage taps and signal-leading wires has not yet been resolved satisfactorily. The secondary voltage method was explained in detail in section 3.3.2 and in reference [101].

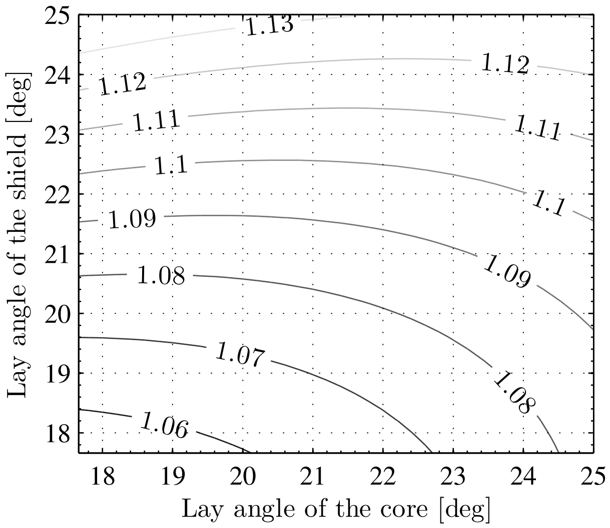

Figure 6.1: Total AC losses of cable per unit length (W m^{-1}).

Figure 6.2: Projected final design.

Table 6.1: Outer layer diameters of final design.

Layer diameter	(mm)
Copper former	27.0
Core layer	30.0
Insulation	39.0
Shield layer	40.0
Stabilization layer-copper	44.0
LN2 flow	60.0
Inner cryostatcorrugated	66
Vacuum	100
Outer cryostatcorrugated	110

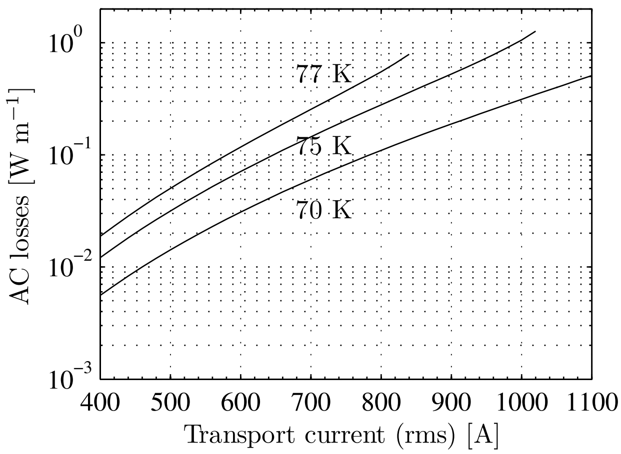

Figure 6.3: Computed total AC losses in final design.

6.2 Concluding remarks

BSCCO tape has been moving to its pre-commercial stage through projects on cables that are almost a kilometer long. However, the second generation of HTS tapes, the YBCO-coated conductors, is expected to lower costs and thereby widen the application range of HTS power cables. In this chapter, a 30-m, one-phase coaxial YBCO cable with a 1-kA transport current and 10-kV operating voltage was designed. Furthermore, the design of the cable prototype pointed out the topics that should be examined in detail in future cables, that is, critical and fault current analysis.

The final design had to take into account interconnected cryogenic, mechanical, and electromagnetic aspects. Cryogenic design must ensure stable operation, that is, the generated heat must be removed from the cryostat. Thus viable operation requires that electromagnetic losses be as small as possible. Furthermore, cryogenic design must provide a way to remove the heat generated during fault conditions. According to the conventional fault current model, the copper stabilization should have a conducting section of more than 354 mm^2 to make the cable to withstand a 40-kA, 1-s fault current without the LN_2 reaching the boiling point from its initial conditions of 77 K and 3 bar.

Mechanical restrictions, for convenient cabling and handling, limit the number of CC tapes per layer and the lay angles. To avoid overlapping CC tape edges during cabling, the layer fill factor cannot exceed 97%. On the other hand, the stranding machine requires lay angles of more than 17.66°.

The electrical insulation follows the industry standard. Therefore, similar cables are also compatible with existing electricity distribution networks. The cable concept was of the cold dielectric type, and lapped insulation impregnated with LN_2 was used. In this way, the inner layers are cooled without specific cooling ducts, and LN_2 is used as part of the dielectric layer.

Chapter 7

Conclusions

Superconducting YBCO cables are designed to improve power grids especially in densely populated areas, because they can transfer energy in a confined space with low losses. Because YBCO tapes have been commercialized only recently, their market price is expected to plummet, making superconducting YBCO cables commercially attractive in future.

The design of these cables combines several fields of engineering. Mechanical design aims at a strong and flexible structure and ensures that the tapes are not exposed to harmful forces during cooling. Thermal design aims to minimize the heat leak to the cryostat and assure full recovery after a fault current. Fault current analysis must be included in electromagnetic design as well. Electromagnetic design should also prevent dielectric breakdown in the electrical insulation, determine the adequate amount and arrangement of tapes needed to carry the specified current, and minimize AC losses.

Suitable modeling tools are essential to simulate electromagnetic behavior. Due to the high aspect ratio of the superconducting layer and the nonlinear and anisotropic nature of the superconductor, the cable is difficult to model with commercial software. Therefore, special computational tools were developed to analyze the stability, cable critical current, and AC losses.

The circuit-analysis-based model was suitable for AC loss modeling. The model takes into account the effect of the magnetic field on the tape critical currents and the nonlinear resistivity arising from AC losses. The AC losses of the individual tapes were determined using the Norris strip model: this approach gave correct AC loss values for individual tape layers as verified with the 0.5-m, one-layer test cable. The losses of the test cable were slightly increased by an uneven current sharing between the individual tapes. This was caused by a small inductive coupling of the tapes, compared to the contact resistance variations between the tapes.

AC loss measurements suggested that the tape's critical current does not necessarily drop as dramatically as traditionally assumed when the tape is transferred from the self-field to a cable. Therefore, the dependence of the critical current on the magnetic fields was closely examined. Calculations pointed out that, indeed, the tape's critical current does not change in a cable similar to the test cable. In future cables with high critical currents, the effect on the cable's critical current may be even more. These results were obtained with the self-made integral-element-method-based algorithm. The same method was also used to extract the intrinsic magnetic field dependence of the critical current density from standard voltage-current measurements. An accurate knowledge of these intrinsic superconductor properties is a key factor when the cable's critical current or AC losses are determined.

In electromagnetic design, fault current analysis cannot be neglected. In a real power grid, fault currents are common: therefore, a copper former is needed to dissipate the fault current energy safely without nitrogen boiling. In this work, a nonlinear 1D FEM model was developed to study the impact of the fault current on the cable. Furthermore, the model suggested that former's eddy currents may increase the cable's heating.

Tools were developed here in connection with the EU funded YBCO cable project Super3C. The cable will be a 30-m, one-phase coaxial cable with a 1-kA transport current and 10-kV operating voltage. The mechanical restrictions limit the number of layers and also the number of tapes within the layers, because to avoid overlapping of the CC tape edges and to keep the cable structure flexible the covering factor cannot exceed 97%. On the other hand, the stranding machine limits the lay angles to at least 17.66°. Cryogenic design ensures stable operation in normal conditions, which means that the generated heat must be removed from the cryostat. Furthermore, heat generated during fault conditions must be removed as well.

The generated heat can be decreased by increasing the copper former cross-section. According to the conventional fault current model used in Super3C design work, the former should have a conducting section of more than 354 mm^2. Then the cable can withstand a 40-kA, 1-s fault current without the LN_2 reaching its the boiling point from the initial conditions of 77 K and 3 bar. Under normal conditions, viable operation requires that electromagnetic losses are as small as possible, which can be obtained by using small, same signed lay angles. Another important design factor is the electric insulation. Here the insulation follows the industry standard to keep the cable compatible with the existing electricity distribution networks. The cold dielectric type cable has lapped insulation impregnated with LN_2. In this way, the inner layers can be cooled without specific ducts, and LN_2 is used as a part of the dielectric layer. The final design was a compromise between the mechanical, thermal, and electromagnetic requirements.

This work points out that in one-layer cables, which are longer than 30 m, the variation in contact resistances between the tapes does not cause uneven current sharing. In two-layer cables, which have one core and one shield layer, the lay angles should have the same sign, and they should be as small as the mechanical restrictions allow. To maximize the cable's critical current and minimize the AC losses in one layer, the superconductor should form as perfect a cylinder as possible. In multilayer cables, in which several layers are connected in parallel, the lay angles should be chosen such that the total AC losses are minimized. The fault current model predicted unusual current sharing between the superconductor and the copper former in 1-kA cables. With a 2-kA fault current, the peak current of the superconductor was 1.5 times the critical current. However, when the current is significantly higher that the superconductor critical current, the existence of the superconductor makes no difference.

After the Super3C cable is completed, AC losses, critical current and fault current effect will be measured. The measurements will reveal how well the developed modeling tools describe real cable operation. So far, the computed losses have been near the test cable measurements. Yet is not clear why the rough circuit analysis model can predict the losses so accurately. This should be studied further by applying numerical methods to simulate current penetration in CC cables.

Bibliography

[1] F. S. Acton. *Numerical Methods That Work*. Math. Assoc. Amer., Washington, DC, 1990.

[2] V. Ambegaokar and B. I. Halperin. Voltage Due to Thermal Noise in the dc Josephson Effect. *Phys. Rev. Lett.*, 22:1364–1366, 1969.

[3] G. J. Anders. *Rating of Electric Power Cables*. IEEE and McGraw-Hill, US, 1997.

[4] G. Arfken and H. Weber. *Mathematical Methods for Physicists*. Harcourt Academic Press, US, fifth edition, 2001.

[5] J. Bardeen, L. N. Cooper, and J. R. Schrieffer. Theory of superconductivity. *Phys. Rev.*, 108:1175–1204, 1957.

[6] R. F. Barron. *Cryogenic Heat Transfer*. Taylor & Francis, 1999.

[7] C. P. Bean. Magnetization of High-Field Superconductors. *Reviews of Modern Physics*, 36:31–39, 1964.

[8] O. Beckman, L. Lundgren, P. Nordblad, L. Sandlund, P. Svedlindh, T. Lundström, and S. Rundqvist. Specific heat and magnetic susceptibility of single phase $YBa_2Cu_3O_7$. *Rev. Mod. Phys.*, 125:425–428, 1987.

[9] J. G. Bednorz and K. A. Müller. Possible high T_c superconductivity in the Ba-La-Cu-O system. *Zeitschrift für Physik B Condensed Matter*, 64:189–193, 1986.

[10] K. J. Binns, P. J. Lawrenson, and C. W. Trowbridge. *The analytical and numerical solution of electric and magnetic fields*. John Wiley, Chichester: UK, 1992.

[11] G. Blatter, M. V. Feigel'man, V. B. Geshkenbein, A. I. Larkin, and V. M. Vinokur. Vortices in high-temperature superconductors. *Rev. Mod. Phys.*, 66:1125–1388, 1994.

[12] A. Bossavit. *Computational electromagnetism.* Academic Press, San Diego: CA., Chestnut Hill: MA., 1998.

[13] A. A. B. Brojeny and J. R. Clem. Self-field effects upon the critical current density of flat superconducting strips. *Supercond. Sci. Technol.*, 18:888–895, 2005.

[14] A. Canning, G. Galli, F. Mauri, A. De Vita, R. Car, Q. Ding, et al. Critical current density for superconductors with giant flux creep. *Cryogenics*, 36:507–511, 1996.

[15] W. Carr. AC loss from the combined action of transport current and applied field. *IEEE Trans. Mag.*, 15:240–243, 1979.

[16] M. Chen, L. Donzel, M. Lakner, and W. Paul. High temperature superconductors for power applications. *Journal of the European Ceramic Society*, 24:1815–1822, 2004.

[17] M. Chen, W. Paul, M. Lakner, L. Donzel, M. Hoidis, P. Unternaehrer, R. Weder, and M. Mendik. 6.4 MVA resitive fault current limiter based on Bi-2212 superconductor. *Physica C*, 372:1657–1663, 2002.

[18] L. Civale, B. Maiorov, J. L. MacManus-Driscoll, H. Wang, T. G. Holesinger, S. R. Foltyn, A. Serquis, and P. N. Arendt. Identification of intrinsic ab-plane pinning in $YBa_2Cu_3O_7$ thin films and coated conductors. *IEEE Trans. Appl. Supercond.*, 15:2808–2811, 2005.

[19] S. T. Dai, L. Z. Lin, Y. B. Lin, Z. Y. Gao, Y. F. Fang, L. H. Gong, Y. P. Teng, F. Y. Zhang, X. Xu, G. Li, et al. The three-phase 75 m long HTS power cable. *Cryogenics*, 47:402–405, 2007.

[20] M. Däumling. A model for the current distribution and ac losses in superconducting multi-layer power cables. *Cryogenics*, 39:759–65, 1999.

[21] K. Develos-Bagarinao, H. Yamasaki, Y. Nakagawa, H. Obara, and H. Yamada. Microcrack-free thick $YBCO/CeO_2/Al_2O_3$ films prepared by a large-area pulsed laser deposition system. *Physica C*, 392:1229–1235, 2003.

[22] K. Develos-Bagarinao, H. Yamasaki, J. C. Nie, and Y. Nakagawa. Thickness dependence of J_c for YBCO thin films prepared by large-area pulsed laser deposition on CeO_2-buffered sapphire substrates. *Supercond. Sci. Technol.*, 18:667–674, 2005.

[23] D. Dew-Hughes. Model for flux creep in high T_c superconductors. *Cryogenics*, 28:674–677, 1988.

[24] J. R. Dormand and P. J. Prince. A family of embedded Runge-Kutta formulae. *J. Comput. Appl. Math.*, 6:19–26, 1980.

[25] R. C. Duckworth, M. J. Gouge, J. W. Lue, C. L. H. Thieme, and D. T. Verebelyi. Substrate and stabilization effects on the transport AC losses in YBCO coated conductors. *IEEE Trans. Appl. Supercond.*, 15:1583–1586, 2005.

[26] J. Evetts. *Concise encyclopedia of magnetic & superconducting materials*. Pergamon Press, Oxford: UK, 1992.

[27] R. Feenstra, A. A. Gapud, F. A. List, E. D. Specht, D. K. Christen, T. G. Holesinger, and D. M. Feldmann. Critical currents $I_c(77\text{ K}) > 350$ A/cm-width achieved in ex situ YBCO coated conductors using a faster conversion process. *IEEE Trans. Appl. Supercond.*, 15:2803–2807, 2005.

[28] S. R. Foltyn, P. Tiwari, R. C. Dye, M. Q. Le, and X. D. Wu. Pulsed laser deposition of thick YBaCuO films with $J = 1$ MA/cm. *Appl. Phys. Lett.*, 63:1848, 1993.

[29] K. Fujinami, H. Suematsu, M. Karppinen, and H. Yamauchi. Effect of overdoping on the irreversibility field and critical current density of the $HgBa_2Ca_2Cu_3O_{8+\delta}$ superconductor. *Physica C*, 307:202–208, 1998.

[30] A. A. Gapud, R. Feenstra, D. K. Christen, J. R. Thompson, and T. G. Holesinger. Temperature and magnetic field dependence of critical currents in YBCO coated conductors with processing-induced variations in pinning properties. *IEEE Trans. Appl. Supercond.*, 15:2578–2581, 2005.

[31] J. Gavaler, A. Santhanam, A. Braginski, M. Ashkin, and M. Janocko. Dimensional effects on current and field properties in NbN films. *IEEE Trans. Mag.*, 17:573–576, 1981.

[32] F. Gömöry. Improvement of the self-field critical current of a high-T_c superconducting tape by the edge cover from soft ferromagnetic material. *Appl. Phys. Lett.*, 89:72506, 2006.

[33] F. Gömöry, J. Souc, M. Vojenciak, E. Seiler, B. Klincok, J. M. Ceballos, E. Pardo, A. Sanchez, C. Navau, S. Farinon, et al. Predicting AC loss in practical superconductors. *Supercond. Sci. Technol.*, 19:60–66, 2006.

[34] F. Gömöry, J. Šouc, M. Vojenčiak, and B. Klinčok. Phenomenological description of flux pinning in non-uniform high-temperature superconductors in magnetic fields lower than the self-field. *Supercond. Sci. Technol.*, 20:271–277, 2007.

[35] M. J. Gouge et al. Tests of tri-axial HTS cables. *IEEE Trans. Appl. Supercond.*, 15:1827–1830, 2005.

[36] P. M. Grant. Currents without borders. *Nature*, 407:139, 2000.

[37] F. Grilli, S. Stavrev, B. Dutoit, S. Spreafico, R. Tebano, F. Gömöry, L. Frolek, and J. Šouc. Numerical modelling of a HTS cable in AC regime. *Physica C*, 401:176–181, 2004.

[38] T. Hartikainen, R. Mikkonen, and J. Lehtonen. Environmental advantages of superconducting devices in distributed electricity-generation. *Applied Energy*, 84:29–38, 2007.

[39] S. Honjo, M. Shimodate, Y. Takahashi, T. Masuda, H. Yumura, C. Suzawa, S. Isojima, and H. Suzuki. Electric properties of a 66 kV 3-core superconducting power cable system. *IEEE Trans. Appl. Supercond.*, 13:1952–1955, 2003.

[40] F. P. Incropera and D. P. DeWitt. *Fundamentals of Heat and Mass Transfer.* Wiley, New York, fourth edition, 1996.

[41] Y. Inoue, H. Kurahashi, Y. Fukumoto, and M. Shimada. Critical current density and n-value of NbTi wires at low field. *IEEE Trans. Appl. Supercond.*, 5:1201–1204, 1995.

[42] Y. Iwasa. *Case Studies in Superconducting Magnets Design and Operational Issues.* Plenum Press, New York, 1994.

[43] Y. Iwasa, E. J. McNiff, R. H. Bellis, and K. Sato. Magnetoresistivity of silver over temperature range 4.2 - 159 K. *Cryogenics*, 33:836–837, 1993.

[44] T. Izumi, Y. Tokunaga, H. Fuji, R. Teranishi, J. Matsuda, S. Asada, T. Honjo, Y. Shiohara, T. Muroga, S. Miyata, et al. Progress in development of coated conductors by TFA-MOD processing. *Physica C*, 412:885–889, 2004.

[45] G. Kastner, C. Schafer, S. Senz, D. Hesse, M. Lorenz, H. Hochmuth, M. Getta, M. A. Hein, T. Kaiser, and G. Müller. Microstructure and microwave surface resistance of YBaCuO thin films. *IEEE Trans. Appl. Supercond.*, 9:2171–2174, 1999.

[46] N. Kelley, P. Cinquemani, P. Belcher, Y. Wen, M. Nassi, P. Corsaro, P. L. Ladie, S. Norman, and M. Rahman. Applications of HTS cables to power transmission: state-of-the-art and opportunities. *Transmission and Distribution Conference, 1999 IEEE*, 1, 1999.

[47] S. W. Kim, J. H. Joo, J. Cho, J. H. Bae, H. J. Kim, and K. C. Seong. Effect of winding direction on four-layer HTS power transmission cable. *Cryogenics*, 43:629–635, 2003.

[48] Y. Kim, S. Kim, T. Harano, M. Tsuda, N. Harada, T. Hamajima, M. Ono, and H. Takano. Layer-current waveform of coaxial multi-layer HTS cable considering the flux flow state. *Cryogenics*, 44:37–43, 2004.

[49] Y. B. Kim, C. F. Hempstead, and A. R. Strnad. Resistive States of Hard Superconductors. *Rev. Mod. Phys.*, 36:43–45, 1964.

[50] D. Kincaid and W. Cheney. *Numerical Analysis.* TBrooks/Cole Publishing Company, Pacific Grove, second edition, 1996.

[51] B. Klinčok and F. Gömöry. Influence of gaps in monolayer superconducting cable on ac losses. *Journal of Physics: Conference Series*, 43:897–900, 2006.

[52] P. Kottman. *The Influence of Magnetic Field and Temperature on Critical Currents in High-T_c Superconductors.* PhD thesis, Tampere University of Technology, 1996.

[53] A. Kuhle, C. Traeholt, S. Kruger Olsen, C. Rasmussen, O. Tønnesen, and M. Däumling. Measuring AC-loss in high temperature superconducting cable-conductors using four probe methods. *IEEE Trans. Appl. Supercond.*, 9:1169–1172, 1999.

[54] J. C. Lagarias, J. A. Reeds, M. H. Wright, and P. E. Wright. Convergence properties of the Nelder-Mead simplex algorithm in low dimensions. *SIAM Journal on Optimization*, 9:112–147, 1998.

[55] E. Lakervi and E. J. Holmes. *Electricity Distribution Network Design.* Peter Peregrinus, UK, 1989.

[56] D. Larbalestier, A. Gurevich, D. M. Feldmann, and A. Polyanskii. High-T_c superconducting materials for electric power applications. *Nature*, 414:368–77, 2001.

[57] A. I. Larkin and Y. N. Ovchinnikov. Pinning in type II superconductors. *Journal of Low Temperature Physics*, 34:409–428, 1979.

[58] J. Lehtonen, H. C. Freyhardt, A. Usoskin, A. Even, E. Pierson, M. Collet, A. Wolf, and P. Herrmann. Design and demonstration of superconducting power link. *Generation, Transmission and Distribution, IEE Proceedings*, 151:755–760, 2004.

[59] J. Lehtonen, A. Korpela, W. Nah, J. Kang, P. Kovác, and T. Melisek. Influence of self-field on the critical current of Bi-2223/Ag tapes. *Physica C*, 403:257–262, 2004.

[60] J. Lehtonen, A. Korpela, J. Pitel, and P. Kovac. Local extreme values in critical current of anisotropic Bi-2223/Ag tapes. *Physica C*, 403:139–144, 2004.

[61] J. Lehtonen, M. Masti, R. Nast, C. Schmidt, W. Goldacker, M. Leghissa, M. Oomen, V. Hussennether, T. J. Arndt, and C. E. Bruzek. AC coil, reactor and cable demonstrations of low AC loss elementary and assembled BSCCO conductors. *Supercond. Sci. Technol.*, 18:400–406, 2005.

[62] J. Lehtonen, R. Mikkonen, and R. Perälä. Temperature dependent self-field effect in measured $V(I, B)$-characteristics of Bi-2223/Ag tapes. *Physica C*, 401:151–154, 2004.

[63] N. Magnusson. Semi-empirical model of the losses in HTS tapes carrying AC currents in AC magnetic fields applied parallel to the tape face. *Physica C*, 349:225–234, 2001.

[64] J. F. Maguire, F. Schmidt, F. Hamber, and T. E. Welsh. Development and demonstration of a long length HTS cable to operate in the Long Island power authority transmission grid. *IEEE Trans. Appl. Supercond.*, 15:1787–1792, 2005.

[65] M. Majoroš, L. Janšák, S. Sello, and S. Zannella. Transient analysis of HTS inductive fault current limiter. *IEEE Trans. Appl. Supercond.*, 7:989–992, 1997.

[66] M. Majoroš, L. Ye, A. V. Velichko, T. A. Coombs, M. D. Sumption, and E. W. Collings. Transport AC losses in YBCO coated conductors. *Supercond. Sci. Technol*, 20:299, 2007.

[67] A. P. Malozemoff. The new generation of superconductor equipment for the electric power grid. *IEEE Trans. Appl. Supercond.*, 16:54–58, 2006.

[68] M. Masti, J. Lehtonen, R. Perälä, W. Nah, and J. Kang. Comparison of voltage–current characteristics of high quality Bi-2223 tapes with

Hall-sensor measurements and computed current density distributions. *Physica C*, 401:155–159, 2004.

[69] T. Masuda, H. Yumura, M. Watanabe, H. Takigawa, Y. Ashibe, C. Suzawa, T. Kato, Y. Yamada, K. Sato, S. Isojima, et al. Design and experimental results for Albany HTS cable. *IEEE Trans. Appl. Supercond.*, 15:1806–1809, 2005.

[70] T. Matsushita, M. Kiuchi, K. Kimura, S. Miyata, A. Ibi, T. Muroga, Y. Yamada, and Y. Shiohara. Dependence of critical current properties on the thickness of the superconducting layer in YBCO coated tapes. *Supercond. Sci. Technol.*, 18:227, 2005.

[71] T. Matsushita, T. Watanabe, Y. Fukumoto, K. Yamauchi, M. Kiuchi, E. S. Otabe, T. Kiss, S. Miyata, A. Ibi, T. Muroga, et al. Flux pinning characteristics of YBCO coated conductor. *Physica C*, 426:1096–1102, 2005.

[72] D. Miyagi, S. Iwata, T. Wakatsuki, N. Takahashi, S. Torii, K. Ueda, and K. Yasuda. The shielding effect of HTS power cable based on E-J -power law. *IEEE Trans. Appl. Supercond.*, 14:654–657, 2004.

[73] A. Mogro-Campero, L. G. Turner, E. L. Hall, N. Lewis, L. A. Peluso, and W. E. Balz. Film thickness dependence of critical current density and microstructure for epitaxial YBaCuO films. *Supercond. Sci. Technol*, 3:62–66, 1990.

[74] S. Mukoyama, S. Maruyama, M. Yagi, Y. Yagi, N. Ishii, O. Sato, M. Amemiya, H. Kimura, and A. Kimura. Development of 500m HTS power cable in super-ACE project. *Cryogenics*, 45:11–15, 2005.

[75] S. Mukoyama, K. Miyoshi, H. Tsubouti, T. Yoshida, M. Mimura, N. Uno, M. Ikeda, H. Ishii, S. Honjo, Y. Iwata, et al. Uniform current distribution conductor of HTS power cable with variable tape-winding pitches. *IEEE Trans. Appl. Supercond.*, 9:1269–1272, 1999.

[76] S. Mukoyama, M. Yagi, H. Hirano, Y. Yamada, T. Izumi, and Y. Shiohara. Development of HTS power cable using YBCO coated conductor. *Physica C: Superconductivity and its applications*, 445:1050–1053, 2006.

[77] H. W. Neumüller, W. Schmidt, H. Kinder, H. C. Freyhardt, B. Stritzker, R. Wördenweber, and V. Kirchhoff. Large area deposition of YBCO thick films for applications in resistive fault current limiting devices. *Journal of Alloys and Compounds*, 251:366–372, 1997.

[78] H. Noji, S. Ooyama, and K. Nakajima. Effective helical-pitch adjustment in a high-T_c superconducting cable for reducing AC losses. *Physica C*, 412:1206–1211, 2004.

[79] H. Noji, S. Ooyama, and K. Nakajima. Reduction of alternating current loss in a high-T_c superconducting transmission cable by means of helical pitch adjustment. *Cryogenics*, 44:151–157, 2004.

[80] W. T. Norris. Calculation of hysteresis losses in hard superconductors carrying ac: isolated conductors and edges of thin sheets. *J. Phys. D: Appl. Phys.*, 3:489–507, 1970.

[81] D. P. Norton, A. Goyal, J. D. Budai, D. K. Christen, D. M. Kroeger, E. D. Specht, Q. He, B. Saffian, M. Paranthaman, C. E. Klabunde, et al. Epitaxial $YBa_2Cu_3O_7$ on Biaxially Textured Nickel (001): An Approach to Superconducting Tapes with High Critical Current Density. *Science*, 274:755–757, 1996.

[82] H. K. Onnes. The discovery of Superconductivity. *Commun. Phys. Lab*, 12:120, 1911.

[83] M. P. Oomen, J. Rieger, M. Leghissa, B. ten Haken, and H. H. J. ten Kate. Dynamic resistance in a slab-like superconductor with $J_c(B)$ dependence. *Supercond. Sci. Technol.*, 12:382–387, 1999.

[84] K. Osamura. *Composite Superconductors.* Marcel Dekker, Inc., 1994.

[85] J. Paasi, P. F. Herrmann, T. Verhaege, J. Lehtonen, J. Bock, L. Cowey, H. C. Freyhardt, A. Usoskin, G. Moulaert, and M. Collet. Superconducting power link for power transmission and fault current limitation. *Physica C*, 354:1–4, 2001.

[86] J. Paasi and A. Korpela. Influence of microcracks and anisotropic conductivity on critical current and exponent n in silver-sheathed HTS tapes. *IEEE Trans. Appl. Supercond.*, 9:2215–2218, 1999.

[87] M. Qiu, Z. C. Zhang, Y. Q. Cao, X. H. Li, Y. Zhang, J. Fang, L. Z. Lin, and L. Y. Xiao. Strain effect of YBCO coated conductor on transport characteristics. *Supercond. Sci. Technol.*, 20:162–167, 2007.

[88] J. J. Rabbers. *AC Loss in Superconducting Tapes and Coils.* PhD thesis, University of Twente, 2001.

[89] J. J. Rabbers, B. ten Haken, and H. H. J. ten Kate. Hysteresis loss and the voltage-current relation in BSCCO tape superconductors. *Physica C: Superconductivity and its applications*, 401:165–170, 2004.

[90] R. P. Reade, P. Berdahl, R. E. Russo, and S. M. Garrison. Laser deposition of biaxially textured yttria-stabilized zirconia buffer layers on polycrystalline metallic alloys for high critical current Y-Ba-Cu-O thin films. *Appl. Phys. Lett.*, 61:2231, 1992.

[91] R. P. Reed and A. F. Clark. *Materials at low temperatures.* American Society for Metals, Metals Park, OH, US, 1984.

[92] J. R. Reitz, F. J. Milford, and R. W. Christy. *Foundations of Electromagnetic Theory.* Addison Wesley, Bristol and Philadelphia, 1992.

[93] G. J. H. M. Rijnders et al. In situ monitoring during pulsed laser deposition of complex oxides using reflection high energy electron diffraction under high oxygen pressure. *Appl. Phys. Lett.*, 70:1888, 1997.

[94] M. W. Rupich, U. Schoop, D. T. Verebelyi, C. Thieme, W. Zhang, X. Li, T. Kodenkandath, N. Nguyen, E. Siegal, D. Buczek, et al. YBCO coated conductors by an MOD/RABiTS/spl trade/process. *IEEE Trans. Appl. Supercond.*, 13:2458–2461, 2003.

[95] U. Schoop, M. W. Rupich, C. Thieme, D. T. Verebelyi, W. Zhang, X. Li, T. Kodenkandath, N. Nguyen, E. Siegal, L. Civale, et al. Second generation HTS wire based on RABiTS substrates and MOD YBCO. *IEEE Trans. Appl. Supercond.*, 15:2611–2616, 2005.

[96] B. Seeber. *Handbook of Applied Superconductivity.* Institute of Physics Publishing, Bristol and Philadelphia, 1998.

[97] V. Selvamanickam, Y. Chen, X. Xiong, Y. Xie, X. Zhang, Y. Qiao, J. Reeves, A. Rar, R. Schmidt, and K. Lenseth. Progress in scale-up of second-generation HTS conductor. *Physica C*, 463:482–487, 2007.

[98] N. Shaked, A. Friedman, M. Sinvani, I. A. Al-Omari, Y. Wolfus, A. Shaulov, and Y. Yeshurun. Effect of external magnetic field on the critical current in single and bifilar Bi-2223 tapes. *Physica C*, 354:237–241, 2001.

[99] P. P. Silvester and R. L. Ferrari. *Finite elements for electrical engineers.* Cambridge University Press, Cambridge, 1983.

[100] U. K. Sinha, J. K. Stovall, P. Haldar, D. T. Lindsay, M. J. Gouge, V. Selvamanickam, R. L. Hughey, J. W. Lue, and N. Vo. Development and test of worlds first industrial high temperature superconducting (hts) power cable. *IEEE Power Engineering Society Winter Meeting*, 2:442–447, 2001.

[101] J. Šouc and F. Gömöry. New approach to the ac loss measurement in the superconducting secondary circuit of an iron-core transformer. *Supercond. Sci. Technol.*, 927:932, 2002.

[102] R. J. Soulen Jr, T. L. Francavilla, W. W. Fuller-Mora, M. M. Miller, C. H. Joshi, W. L. Carter, A. J. Rodenbush, M. D. Manlief, and D. Aized. Explanation of the dissipation observed in several high-temperature superconductors using a modified Ambegaokar-Halperin model. *Phys. Rev. B*, 50:478–487, 1994.

[103] S. Spreafico, L. Gherardi, S. Fleshier, D. Tatelbaum, J. Leone, D. Yu, and G. Snitchler. The effect of self-field on current capacity in Bi-2223 composite strands. *IEEE Trans. Appl. Supercond.*, 9:2159–2162, 1999.

[104] S. Stavrev, F. Grilli, B. Dutoit, and S. P. Ashworth. Comparison of the AC losses of BSCCO and YBCO conductors by means of numerical analysis. *Supercond. Sci. Technol.*, 18:1300–1312, 2005.

[105] A. Stenvall, A. Korpela, J. Lehtonen, and R. Mikkonen. Two ways to model voltage-current curves of adiabatic MgB_2 wires. *Supercond. Sci. Technol.*, 20:859–864, 2007.

[106] M. D. Sumption and E. W. Collings. Stability and flux jumping of internal-Sn, Nb_3Sn conductors (and a model system MgB_2). *IEEE Trans. Appl. Supercond.*, 13:3394–3397, 2003.

[107] H. Takigawa, H. Yumura, T. Masuda, M. Watanabe, Y. Ashibe, H. Itoh, C. Suzawa, M. Hirose, K. Yatsuka, K. Sato, et al. The installation and test results for Albany HTS cable project. *Physica C*, 463:1127–1131, 2007.

[108] R. Teranishi, T. Izumi, and Y. Shiohara. Highlights of coated conductor development in Japan. *Supercond. Sci. Technol.*, 19:4–12, 2006.

[109] Y. Tokunaga, T. Honjo, T. Izumi, Y. Shiohara, Y. Iijima, T. Saitoh, T. Goto, A. Yoshinaka, and A. Yajima. Advanced TFA-MOD process of high critical current YBCO films for coated conductors. *Cryogenics*, 44:817–822, 2004.

[110] O. Tønnesen, M. Däumling, K. H. Jensen, S. Kvorning, S. K. Olsen, C. Træholt, E. Veje, D. Willen, and J. Østergaard. Operation experiences with a 30 kV/100 MVA high temperature superconducting cable system. *Supercond. Sci. Technol.*, 17:101–105, 2004.

[111] M. Tsuda, J. Fujimoto, N. Harada, and T. Hamajima. AC loss reduction of coaxial multi-layer HTS cable. *IEEE Trans. Appl. Supercond.*, 14:642–645, 2004.

[112] O. Tsukamoto. Ways for power applications of high temperature superconductors to go into the real world. *Supercond. Sci. Technol.*, 17:185–190, 2004.

[113] O. Tsukamoto. Roads for HTS power applications to go into the real world Cost issues and technical issues. *Cryogenics*, 45:3–10, 2005.

[114] K. Ueda, O. Tsukamoto, S. Nagaya, H. Kimura, and S. Akita. R&D of a 500 m superconducting cable in Japan. *Applied Superconductivity, IEEE Transactions on*, 13:1946–1951, 2003.

[115] A. Usoskin, H. C. Freyhardt, A. Issaev, J. Dzick, J. Knoke, M. P. Oomen, M. Leghissa, and H. W. Neumueller. Large area YBCO-coated stainless steel tapes with high critical currents. *IEEE Trans. Appl. Supercond.*, 13:2452–2457, 2003.

[116] A. Usoskin, A. Rutt, J. Knoke, H. Krauth, and Arndt. Long-length YBCO coated stainless steel tapes with high critical currents. *IEEE Trans. Appl. Supercond.*, 15:2604–2607, 2005.

[117] A. Vostner, H. W. Weber, H. C. Freyhardt, A. Usoskin, J. Dzick, and J. Knoke. Transport and anisotropic properties of coated conductors deposited by PLD on steel substrates. *IEEE Trans. Appl. Supercond.*, 11:2715–2718, 2001.

[118] J. Šouc, M. Vojenčiak, F. Gömöry, X. Granados, A. Usoskin, and A. Rutt. AC loss of YBCO coated tape prepared by laser ablation. *Journal of Physics: Conference Series*, 43:127–129, 2006.

[119] C. P. Wang, K. B. Do, M. R. Beasley, T. H. Geballe, and R. H. Hammond. Deposition of in-plane textured MgO on amorphous SiN substrates by ion-beam-assisted deposition and comparisons with ion-beam-assisted deposited yttria-stabilized-zirconia. *Appl. Phys. Lett.*, 71:2955, 1997.

[120] W. Warnes and D. Larbalestier. Determination of the average critical current from measurements of the extended resistive transition. *IEEE Trans. Appl. Supercond.*, 23:1183–1187, 1987.

[121] T. Watanabe, R. Kuriki, H. Iwai, T. Muroga, S. Miyata, A. Ibi, Y. Yamada, and Y. Shiohara. High rate deposition by PLD of YBCO films for coated conductors. *IEEE Trans. Appl. Supercond.*, 15:2566–2569, 2005.

[122] J. O. Willis. Superconducting transmission cables. *Power Engineering Review, IEEE*, 20:10–14, 2000.

[123] M. N. Wilson. *Superconducting Magnets*. Oxford University Press, 1983.

[124] A. M. Wolsky. Hts cable – status, challenge and opportunity. Technical report, International Energy Agency, Argonne National Laboratory, US, 2004.

[125] M. K. Wu, J. R. Ashburn, C. J. Torng, P. H. Hor, R. L. Meng, L. Gao, Z. J. Huang, Y. Q. Wang, and C. W. Chu. Superconductivity at 93 k in a new mixed-phase yb-ba-cu-o compound system at ambient pressure. *Phys. Rev. Lett.*, 58:908–910, 1987.

[126] Y. Xin, B. Hou, Y. Bi, H. Xi, Y. Zhang, A. Ren, X. Yang, Z. Han, S. Wu, and H. Ding. Introduction of China's first live grid installed HTS power cable system. *IEEE Trans. Appl. Supercond.*, 15:1814–1817, 2005.

[127] N. Yamada, T. Akune, N. Sakamoto, and Y. Matsumoto. Temperature dependence of irreversibility fields in Re doped Hg-1223 superconductors. *Physica C*, 412:425–429, 2004.

[128] Y. Yamada, T. Muroga, H. Iwai, T. Watanabe, S. Miyata, and Y. Shiohara. Progress of PLD and IBAD processes for YBCO wire in the SRL-Nagoya Coated Conductor Centrenew method for a coated conductor using a self-epitaxial PLD-CeO_2 buffer. *Supercond. Sci. Technol.*, 17:70–73, 2004.

[129] K. Yamafuji and T. Kiss. A new interpretation of the glass-liquid transition of pinned fluxoids in high-T_c superconductors. *Physica C*, 258:197–212, 1996.

[130] G. M. Zhang, J. Schwartz, P. Sastry, L. Z. Lin, L. Y. Xiao, and Y. J. Yu. The effects of bending strain on the critical current and AC loss of BSCCO/Ag tapes. *Supercond. Sci. Technol.*, 17:1018–1021, 2004.